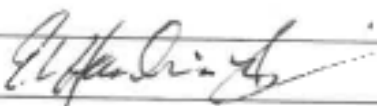


## APPENDIX E FCT DOCUMENT COVER SHEET <sup>1</sup>

Name/Title of Deliverable/Milestone/  
Revision No. DPC Criticality Simulation Preliminary Phase: Fuel/Basket  
Degradation Models (Milestone M3SF-19SN010305071)

Work Package Title and Number Multi-Physics Simulation of DPC Criticality – SNL  
(SF-19SN01030507)

Work Package WBS Number WBS 1.08.01.03.05

Responsible Work Package Manager Ernest Hardin   
(Name/Signature)

Date Submitted

Quality Rigor Level for Deliverable/Milestone <sup>2</sup>	<input type="checkbox"/> QRL-1 <input type="checkbox"/> Nuclear Data	<input type="checkbox"/> QRL-2	<input type="checkbox"/> QRL-3	<input checked="" type="checkbox"/> QRL-4 Lab- Specific
--	---	--------------------------------	--------------------------------	--

This deliverable was prepared in accordance with Sandia National Laboratories  
(Participant/National Laboratory Name)

QA program which meets the requirements of  
 DOE Order 414.1     NQA-1-2000     Other

**This Deliverable was subjected to:**

Technical Review

Peer Review

**Technical Review (TR)**

**Peer Review (PR)**

**Review Documentation Provided**

**Review Documentation Provided**

- Signed TR Report or,
- Signed TR Concurrence Sheet or,
- Signature of TR Reviewer(s) below

- Signed PR Report or,
- Signed PR Concurrence Sheet or,
- Signature of PR Reviewer(s) below

**Name and Signature of Reviewers**

Michael Nole /SNL  for 9/17/19

**NOTE 1:** Appendix E should be filled out and submitted with the deliverable. Or, if the PICS:NE system permits, completely enter all applicable information in the PICS:NE Deliverable Form. The requirement is to ensure that all applicable information is entered either in the PICS:NE system or by using the FCT Document Cover Sheet.

- In some cases there may be a milestone where an item is being fabricated, maintenance is being performed on a facility, or a document is being issued through a formal document control process where it specifically calls out a formal review of the document. In these cases, documentation (e.g., inspection report, maintenance request, work planning package documentation or the documented review of the issued document through the document control process) of the completion of the activity, along with the Document Cover Sheet, is sufficient to demonstrate achieving the milestone.

**NOTE 2:** If QRL 1, 2, or 3 is not assigned, then the QRL 4 box must be checked, and the work is understood to be performed using laboratory specific QA requirements. This includes any deliverable developed in conformance with the respective National Laboratory / Participant, DOE or NNSA-approved QA Program.

**DPC Criticality  
Simulation Preliminary  
Phase: Fuel/Basket  
Degradation Models**

**Spent Fuel and Waste Disposition**

Prepared for the  
U.S. Department of Energy,  
Office of Spent Fuel and Waste Science and Technology  
by  
Sandia National Laboratories and  
Itasca Consulting Group, Inc.

**M3SF-19SN010305071  
September 17, 2019**

### Revision History

<i>DPC Criticality Simulation Preliminary Phase: Fuel/Basket Degradation Models</i> Deliverable: M3SF-19SN010305071 Work Package: 1.08.01.03.05 – Multiphysics Simulation of DPC Criticality – SNL WBS: 1.08.01.03.05	Technical review performed by Sandia (compliant with NTRD QAPD Rev. 5, Appendix B). Sandia approval (Tracking # 11020970) is for internal use only. The resulting copy (Rev. 0) was submitted to PICS/NE in satisfaction of the deliverable, and to DOE for management review prior to publication.
---	---

**Disclaimer:** This is a technical report that does not take into account contractual limitations or obligations under the Standard Contract for Disposal of Spent Nuclear Fuel and/or High-Level Radioactive Waste (Standard Contract) (10 CFR Part 961). For example, under the provisions of the Standard Contract, spent nuclear fuel in multi-assembly canisters is not an acceptable waste form, absent a mutually agreed to contract amendment. To the extent discussions or recommendations in this report conflict with the provisions of the Standard Contract, the Standard absent a mutually agreed to contract amendment. To the extent discussions or recommendations in this report conflict with the provisions of the Standard Contract, the Standard Contract governs the obligations of the parties, and this report in no manner supersedes, overrides, or amends the Standard Contract.

This report reflects technical work which could support future decision making by DOE. No inferences should be drawn from this report regarding future actions by DOE, which are limited both by the terms of the Standard Contract and a lack of Congressional appropriations for the Department to fulfill its obligations under the Nuclear Waste Policy Act including licensing and construction of a spent nuclear fuel repository.

**Additional Notice:** This report was prepared as an account of work sponsored by an agency of the United States Government. Neither the United States Government, nor any agency thereof, nor any of their employees, nor any of their contractors, subcontractors, or their employees, make any warranty, express or implied, or assume any legal liability or responsibility for the accuracy, completeness, or usefulness of any information, apparatus, product, or process disclosed, or represent that its use would not infringe privately owned rights. Reference herein to any specific commercial product, process, or service by trade name, trademark, manufacturer, or otherwise, does not necessarily constitute or imply its endorsement, recommendation, or favoring by the United States Government, any agency thereof, or any of their contractors or subcontractors. The views and opinions expressed herein do not necessarily state or reflect those of the United States Government, any agency thereof, or any of their contractors.

Sandia National Laboratories is a multimission laboratory managed and operated by National Technology and Engineering Solutions of Sandia LLC, a wholly owned subsidiary of Honeywell International Inc. for the U.S. Department of Energy's National Nuclear Security Administration under contract DE-NA0003525.



**Approved for Unclassified, Limited Release**

## ACKNOWLEDGEMENTS

This report was a group effort with major contributions from:

<b>Contributor</b>	<b>Section</b>
Ernest Hardin/SNL	Sections 1, 2 and 8; editor overall
Branko Damjanac/Itasca	Lead for Sections 3 through 7
Jason Furtney/Itasca	Sections 6 and 7
Azadeh Riahi/Itasca	Sections 5 and 6
Varun/Itasca	Sections 4, 5 and 6
Mike Nole/SNL	Technical reviewer

All contributors are credited with input to conclusions and recommendations in each modeling section, and Section 8. In addition, important insights were provided by Brady Hanson/PNNL and Halim Alsaed/EnviroNuclear LLC. The authors would also like to thank others who contributed their ideas, particularly Bob Clark of DOE/SFWS&T, Rob Howard, Kaushik Banerjee and John Scaglione of ORNL, and Laura Price and Geoff Freeze of SNL. The DPC disposition R&D team extends beyond the group mentioned here to include many others at SNL and ORNL.

## TABLE OF CONTENTS

<b>1. Introduction .....</b>	<b>12</b>
<b>2. Review of Fuel/Basket Material Degradation Processes and Models .....</b>	<b>14</b>
2.1 Cladding Creep Rupture .....	14
2.2 Initially Failed Cladding .....	15
2.3 Cladding Corrosion Mechanisms .....	16
2.4 Axial Splitting Model for Unsaturated, Oxidizing Conditions .....	19
2.5 Axial Splitting Model for Saturated, Reducing Conditions .....	20
2.6 Fuel Assembly Spacer Grids and End Nozzles .....	20
2.7 General Corrosion Models for Basket Materials .....	21
2.8 Cladding Bending and Shear (Seismic Loads) .....	23
2.9 Summary of Degradation Processes for Modeling .....	24
<b>3. Model Scoping .....</b>	<b>26</b>
3.1 Fuel Assembly Cell Model .....	26
Basket Material Degradation .....	26
3.2 Basket Degradation Model .....	27
Initial <i>FLAC3D</i> Continuum Modeling Study .....	28
<i>3DEC</i> Model of Canister and Internals .....	28
3.3 Waste Package Breach Model .....	28
3.4 Model Parameters .....	29
Corrosion Submodel .....	29
3.4 Future Model Development .....	30
<b>4. Fuel Assembly Cell Model .....</b>	<b>32</b>
4.1 Introduction .....	32
4.2 Model Setup .....	32
4.3 Fuel Assembly Cell Model Results .....	33
4.4 Seismic Analysis .....	39
4.5 Discussion .....	40
<b>5. Basket Degradation Model .....</b>	<b>42</b>
5.1 <i>FLAC3D</i> Study of Basket Plate Deformations .....	42
Introduction .....	42
Model Geometry .....	42
Fuel Assembly Loading .....	44
Material Properties .....	44
Results for Shear and Bending Failure of Horizontal Plates .....	44
Numerical Modeling .....	45
Calculations Based on Beam Theory .....	48
Analysis of Entire Basket Collapse Due to Buckling .....	48
Analysis of Buckling of Individual Cells .....	53
Discussion and Conclusions .....	54

5.2	Distinct Element Model of Basket Collapse .....	55
	Detailed Basket Model .....	55
	Fuel Assemblies .....	58
	Single-Rod Model .....	60
	Simplified Basket Model.....	64
	Static Analyses .....	65
	Seismic Analyses.....	67
5.3	Discussion .....	69
<b>6.</b>	<b>Waste Package Breach Model .....</b>	<b>71</b>
6.1	Introduction .....	71
6.2	Methodology .....	71
6.3	Canister and Disposal Overpack Properties .....	73
6.4	Results .....	74
	Critical Pressure for Steel Yielding.....	74
	Numerical Model Results.....	74
6.5	Discussion .....	77
<b>7.</b>	<b>Coupling of Mechanical and Porous-Medium Flow Models .....</b>	<b>78</b>
	<i>FLAC3D</i> Background.....	78
	<i>TOUGH3</i> Background.....	79
7.1	Coupling Methodology.....	80
7.2	Coupling Implementation.....	81
7.3	Example Coupling Problem .....	82
<b>8.</b>	<b>Summary and Recommendations .....</b>	<b>85</b>
8.1	Fuel Assembly Cell Model.....	85
8.2	Basket Degradation Model.....	85
8.3	Waste Package Breach Model.....	86
8.4	Coupling of Mechanical, Thermal, and Flow Processes .....	86
<b>9.</b>	<b>References.....</b>	<b>87</b>
	<b>Appendix A. Fuel Assembly Characteristics.....</b>	<b>90</b>
	<b>Appendix B. Analytical Buckling Load.....</b>	<b>91</b>
	<b>Appendix C. Selection of Stainless steel Yield Strength .....</b>	<b>92</b>
	<b>Appendix D. Generated <i>Python</i> Class That Performs Coupling Tasks</b> ( <i>flac3dtough3.FLAC3D_TOUGH3</i> ).....	<b>94</b>

## LIST OF FIGURES

Figure 1.	Typical internal structure of canister and detail of fuel assembly cell. ....	27
Figure 2.	The geometry of the WP breach model .....	29
Figure 3.	Model layout showing plates (green), fuel rods (red), and corrosion products (blue). ....	34
Figure 4.	Model output showing number of particles representing corrosion product in each zone of the grid. ....	34
Figure 5.	Corrosion products at (top left) X years, (top right) 2X years, (bottom left) 4X years, and (bottom right) 8X years for balls and 0° inclination case. ....	35
Figure 6.	Corrosion products at (top left) X years, (top right) 2X years, (bottom left) 4X years, and (bottom right) 8X years for balls and 30° inclination case. ....	36
Figure 7.	Corrosion products at (top left) X years, (top right) 2X years, (bottom left) 4X years, and (bottom right) 8X years for clumps and 0° inclination case. ....	37
Figure 8.	Corrosion products at (top left) X years, (top right) 2X years, (bottom left) 4X years, and (bottom right) 8X years for clumps and 30° inclination case. ....	38
Figure 9.	Velocity time histories for horizontal (upper) and vertical (lower) components of ground motion used for shaking the plates. ....	39
Figure 10.	Model configuration at 1 second (top left), 2 seconds (top right), 5 seconds (bottom left), and after the end of shaking (bottom right) for clumps and 0° inclination case. ....	40
Figure 11.	Cross-section view of fuel basket (from Figure 1.2.4 in Holtec 2018). ....	43
Figure 12.	Geometry of the fuel assembly. ....	43
Figure 13.	<i>FLAC3D</i> model representation along the canister axis. The black dotted box shows the load of fuel assembly and spacer grid transferred to the horizontal plate at the interface between each spacer grid and horizontal plate. Only half the spacing between spacer grids is represented in the <i>FLAC3D</i> model, as shown. ....	44
Figure 14.	Single-cell model (of the basket shown in Figure 11) with spacer grid represented as an equivalent rigid material. ....	45
Figure 15.	Displacement contours (m) within the basket cell for a plate thickness of 2 mm (displacements magnified 100×). ....	46
Figure 16.	Displacement contours (m) within the basket cell for a plate thickness of 1 mm (displacements magnified 100×). ....	47
Figure 17.	Contours of $\sigma_{xx}$ (Pa) within the basket cell for a plate thickness of 1 mm (displacements magnified 100×). ....	47
Figure 18.	Geometry and boundary conditions of the full basket model. ....	49
Figure 19.	Buckling mode and critical thickness for onset of buckling for basket models. Colors represent the relative value of horizontal displacement, with blue being close to zero and red representing the maximum. ....	51
Figure 20.	Deformation of Model B prior to the state shown in Figure 19 (Model B). ....	52
Figure 21.	Basket model with spacer grid implementation (black color shows regions constrained by spacer grid). ....	53
Figure 22.	Deformation contours of basket Model B with implementation of a lateral constraint due to presence of spacer grids. ....	53
Figure 23.	Geometry and boundary condition for a single-cell model. ....	54

Figure 24.	Displacement contours (m) from <i>FLAC3D</i> buckling analysis of a single-cell model, for plate thickness of 1.0 mm (left); and plate thickness of 0.8 mm (right). The displacements for the model with thickness of 0.8 mm are not final displacements because the model is unstable. ....	54
Figure 25.	Model setup showing different components in longitudinal view.....	56
Figure 26.	Model setup showing different components in transverse view.....	57
Figure 27.	Model setup showing different components in perspective view.....	58
Figure 28.	Components of a typical 17×17 PWR fuel assembly (Lindgren and Durbin 2013).....	58
Figure 29.	Details of a single cell of spacer grid (Lee et al. 2007). ....	59
Figure 30.	Single rod model of guide tubes showing comparison of displacement profiles (m) for cantilever bending obtained using analytical solution and <i>3DEC</i> model. ....	61
Figure 31.	Moment-curvature responses for a single fuel rod obtained from laboratory tests (left) and from <i>3DEC</i> model (right).....	62
Figure 32.	Model setup showing different components in the simplified model.....	64
Figure 33.	Final configuration at the end of Stage 3 for the detailed model.....	66
Figure 34.	Final configuration at the end of Stage 3 for the simplified model. ....	66
Figure 35.	Bending of rods under gravity in the model that neglected contribution from fuel pellets.....	67
Figure 36.	Rods breaking and sliding out of end nozzles at the end of Stage 3 for the model with greater height of fall due to narrower canister supports. ....	67
Figure 37.	Velocity time histories of three components of ground motion used for shaking of the canister.....	68
Figure 38.	Model configuration at different times during the shaking. ....	69
Figure 39.	Analyzed locations and orientations of the initial fractures.....	72
Figure 40.	Typical results (displacement magnitude contours shown in meters) for a longitudinal fracture.....	75
Figure 41.	Critical pressure for longitudinal fractures of different lengths in both the canister and the overpack. ....	76
Figure 42.	Critical pressure for hoop fractures of different lengths in both the canister and the overpack. ....	76
Figure 43.	Schematic of <i>FLAC3D–TOUGH3</i> coupling. ....	81
Figure 44.	<i>TOUGH3</i> predictions of pore pressure (Pa) for cold water injection. ....	83
Figure 45.	<i>TOUGH3</i> predictions of temperature (°C) for cold water injection. ....	83
Figure 46.	<i>FLAC3D</i> predictions of total stress (Pa) (including thermal strains).....	84
Figure 47.	<i>FLAC3D</i> predictions of effective stress (Pa). ....	84
Figure B-1.	Column effective length factors for Euler's critical load (image from Wikipedia, public domain.) ....	91
Figure C-1.	Stress-strain curve for stainless steel at room temperature (Rowlands). ....	92
Figure C-2.	Stress-strain curve for stainless steel at room temperature ( <a href="https://icme.hpc.msstate.edu/mediawiki/index.php/316_Stainless_Steel">https://icme.hpc.msstate.edu/mediawiki/index.php/316_Stainless_Steel</a> ). ....	93

**LIST OF TABLES**

Table 1.	Properties of shell, basket, and fuel materials. ....	30
Table 2.	Fuel properties for basket component deformation scoping calculations.....	44
Table 3.	Analytical calculation for maximum axial and shear forces in a basket plate.....	48
Table 4.	Parameters related to model geometry.....	63
Table 5.	Parameters related to material properties.....	63
Table 6.	Geometric details of canister. ....	73
Table A-1.	PWR fuel assembly characteristics (adapted from Table 1.2.10, Holtec 2018). ....	90

## ABSTRACT

This report documents progress in modeling the degradation of commercial spent nuclear fuel (SNF) and dual-purpose canister (DPC) baskets, in response to corrosion once waste packages (WPs) in a repository are breached and admit ground water, and to ground motion once the fuel assemblies and baskets are degraded. It is intended that degraded fuel/basket configurations will be evaluated for nuclear reactivity, as the configurations evolve with time over many thousands of years. The capabilities demonstrated may also be used in the future to simulate the behavior of disposal criticality control features added to DPC baskets or fuel assemblies, in the form of disposal control rods, inserts, channels, etc.

The meshless, distinct element approach used in *PFC3D* software has been shown to be useful for studying redistribution of corrosion products, particularly for controlling particle shape, and the conditions for particle formation and release. Preliminary results show that seismic ground motion might cause rapid thinning of partially degraded absorber plates, in baskets made entirely from aluminum-based materials, which could lead to transient criticality events. Advancements to the modeling approach are proposed which could improve realism and represent a wider range of DPC basket designs.

A basket degradation model has been built to study the nature of basket collapse (from the weight of fuel) in response to corrosion and ground motion. Degradation of metal plates comprising an “egg-crate” basket structure will lead to redistribution of loads onto fuel assembly components, deformation of fuel rods, and degradation of neutron absorbing components. Preliminary results from the basket degradation model show how it could be used to generate degraded fuel/basket configurations, and also how it could be used to represent the evolution of DPCs with added disposal criticality control features. The model can also be used to represent external loading of a DPC by ground water pressure after breach of the disposal overpack but prior to breach of the canister. Model enhancements are proposed including extension to BWR fuel, stainless steel basket plates, Boral® sandwich neutron absorber plates, and representing degraded components as disaggregated pieces rather than removing them from the model.

A quasi-static WP breach model was developed to investigate deformation and growth of initial breaches (cracks) in the DPC shell and the disposal overpack, in response to internal pressurization. Preliminary results show that longitudinal initial fractures around 1 cm and longer can grow due to internal pressurization, while initial circumferential fractures less than approximately 6 cm long will not grow before plastic yielding occurs. The results also show that deformation of initial cracks will increase the transmissivity of the breach at relatively low differential pressures, and that crack growth can occur at pressures of just a few MPa. This could be significant from the standpoint of limiting the energy of transient events. One important uncertainty is the series arrangement of breaches in the canister and overpack, which have different thicknesses. Further development of the WP breach model is recommended to simulate a pulse of thermal energy from a criticality event within a saturated WP. Such a scoping model would couple heat generation to internal pressure and transmissivity of breaches. The venting rate for water mass from the package would be a function of breach morphology, energy input, and other important factors.

Coupling of *FLAC3D* with porous-medium heat-mass transport code *TOUGH3* is reported in the literature, limited to quasi-static mechanical conditions. Relaxing this restriction is one objective for coupling studies reported here. A preliminary *FLAC3D-TOUGH3* coupled model is presented with an example calculation. The finite-displacement capability of *FLAC3D* should be incorporated in the coupling scheme and tested for conservation and flux balances, in multi-dimensional problems of increasing complexity. The problems should include adjustments to permeability and fluid storage based on changes in finite volume strain, and should include approximations for open spaces in the model (e.g., pseudo-permeability). A similar transport code, *PFLOTRAN* (open-source freeware) is being used extensively for PA and should be considered for coupling with *FLAC3D*. Note that *FLAC3D* has been selected by investigators in lieu of fully implicit finite element codes, because of the mechanical modeling features (e.g., interfacing with distinct element codes, and seismic boundary conditions) and constitutive models (e.g., creep) that are available.

## ACRONYMS

ANL	Argonne National Laboratory
BWR	Boiling water reactor
DPC	Dual-purpose canister (storage and transportation)
EoS	Equation of state
FMDM	Fuel matrix degradation model
LEFM	Linear elastic fracture mechanics
MMC	Metal-matrix composite
ORNL	Oak Ridge National Laboratory
PA	Performance assessment
PGV	Peak ground velocity
PNNL	Pacific Northwest National Laboratory
PWR	Pressurized water reactor
SCC	Stress corrosion cracking
SNF	Spent nuclear fuel
SNL	Sandia National Laboratories
WP	Waste package (consists of DPC or other canister, plus a disposal overpack)

## **DPC Criticality Simulation Preliminary Phase: Fuel/Basket Degradation Models**

### **1. Introduction**

This report documents progress in model development to represent degradation of spent nuclear fuel (SNF) and dual-purpose canister (DPC) baskets, in response to corrosion once waste packages in a repository are breached and admit ground water, and to ground motion once the SNF and baskets are degraded. It is intended that degraded fuel/basket configurations will be evaluated for nuclear reactivity, as the configurations evolve with time. The capabilities demonstrated may also be used in the future to simulate the behavior of disposal criticality control features added to DPC baskets or fuel assemblies, in the form of disposal control rods, inserts, channels, etc.

Multi-physics modeling often involves externally coupled simulation codes, and this report describes preliminary work to use different codes to represent aspects of the complex phenomenology of waste package internal degradation and heat-mass transport.

Model development described here is complementary with parallel development underway at Oak Ridge National Laboratory (ORNL; work package SF-19OR01030501 Rev. 2). The ORNL work has the objective to closely couple neutron propagation and fluid dynamics, by externally coupling existing codes (a different set than is described here). The work described here is intended to be coupled with the ORNL models in the future, by specifying degraded fuel/basket configurations for analysis. Multi-physics models developed at each lab can also be compared, for model validation.

Section 2 is a review of literature describing the degradation of fuel rods,  $\text{UO}_2$ , and basket materials. It was developed to support the model development thrust, and includes these processes:

- Fuel cladding: initial condition, creep rupture due to internal gas pressure and bending, and external (water-side) localized corrosion.
- $\text{UO}_2$  fuel: alteration on exposure to moisture (with radiolysis), axial splitting of cladding, and fuel-cladding bonding.
- Basket: general corrosion (stainless steel, aluminum-based materials).

Other processes such as cladding stress corrosion and delayed hydride cracking, and localized corrosion of basket materials, are possible but believed to have minor importance, and can be addressed later in model development. The scope of literature included in this review is expected to evolve with time as the models evolve and the work receives wider exposure.

Section 3 summarizes scoping input used to frame model development in FY19. This includes degradation mechanisms to be considered, material properties, modeling approaches, etc.

Section 4 describes the fuel assembly cell model which tracks degradation products from a corroding basket, as they fall and accumulate within a fuel assembly residing in a single cell of a fuel basket. A simple basket design is selected consisting of an “egg-crate” structure made from plates of an aluminum-based material. This type of basket is common among existing DPCs, and may be the fastest to degrade among all DPC designs. The fuel assembly cell model will be useful for predicting thinning of neutron absorbing plates, especially rapid thinning in response to seismic ground motion.

Section 5 describes the basket degradation model, which represents weakening and collapse of the basket structure, again consisting of an “egg-crate” structure of aluminum-based material. Various

supporting calculations are described which were used to develop a detailed model of an entire DPC with basket and fuel, and also to justify certain numerical simplifications to speed up simulations. The basket degradation model will be useful for producing degraded configurations of fuel and neutron absorbers that can be analyzed for reactivity (including disposal criticality control features added to DPC baskets or fuel assemblies).

Section 6 develops the waste package breach model, a solid mechanics simulation of the deformation and growth of cracks in the DPC shell and disposal overpack, in response to internal pressure such as could be produced by a criticality event. The initial breaches that allow ground water to enter DPCs are conceptualized as cracks in both the shell and overpack. The behavior of these initial cracks in response to canister pressurization varies depending on crack size and location, material properties, and loading conditions.

Section 7 describes preliminary results from coupling of *FLAC3D* (a multi-purpose, widely used solid mechanics modeling code with thermal and poroelastic coupling capabilities) with a porous-medium heat-mass transport code (*TOUGH3*). An eventual use for such coupling is described in the future modeling part of the model scoping section (Section 3.4).

Finally, in Section 8 the conclusions and recommendations from the model description sections are collected, with additional commentary on how these models can be used to evaluate alternative approaches to direct disposal of commercial SNF in DPCs.

## **2. Review of Fuel/Basket Material Degradation Processes and Models**

Ernest Hardin (Sandia National Laboratories)

The following information is based on literature review and is intended to guide the selection of model features and degradation mechanisms for fuel and basket degradation model development.

### **2.1 Cladding Creep Rupture**

Zircaloy is a highly corrosion resistant, inert material that can maintain long-term stability over a range of temperature and chemical environments, e.g., in the pH range 2 to 12. No additional degradation of Zircaloy will occur in sealed waste packages because of the lack of moisture and oxygen (intact fuel rods). Waste package breach is a multi-step process whereby the outer layer corrodes due to external conditions (corrosion, rockfall, seismicity, faulting, etc.) then water/moisture ingress causes corrosion of the inner layers including the DPC shell. After breach, the waste package is invaded by ground water (in saturated settings) or moisture and air (unsaturated settings), and degradation of the fuel and basket begins.

This review concludes that two modes of degradation are the most important causes of cladding perforation: elastoplastic creep leading to rupture, and penetration of the cladding wall by corrosion that occurs with concentrated water chemistry.

Cladding creep occurs only when the cladding is intact, in response to persistent tensile stress caused by internal gas pressure. It depends on the amount of gas (initial gas charge plus fission gases, which depend on burnup), and on the internal void volume (fuel-cladding gaps, pellet-pellet gaps, and plenum volume). Fuel pellets tend to swell with burnup, but this may be assumed negligible for most fuel types and typical burnup. Cladding creep is sensitive to temperature because the gas expands ideally, and the solid-state creep process is thermally activated. Creep begins in the reactor with several years of exposure at operating temperature (~325°C) with fission gas production. Cladding creep is accelerated by cladding damage, caused by thinning due to formation of an oxide layer, and embrittlement that reduces the total creep strain tolerated before rupture. These processes are directly related to the extent of burnup, especially the rate of oxide formation which accelerates in higher burnup fuel. As creep accumulates the void volume within the fuel rods increases, which mitigates the tensile stress condition somewhat and has been taken into account in predictive models.

During pool storage the fuel temperature is much cooler and radiation flux is less than during reactor operation, so that cladding damage processes slow to insignificance. Creep continues at a much lower rate in response to the internal gas pressure. During DPC dewatering the fuel temperature may approach 400°C, accelerating cladding creep but only briefly. Dry storage temperature is initially higher than fuel pool temperature, up to approximately 200°C depending on burnup and age, for a few decades until relatively short-lived fission products decay (half-lives ~30 yr). Additional creep may occur during dry storage because of the integrated time-temperature exposure.

Cladding creep may result in rupture if the total creep strain exceeds a threshold of about 6%. Unirradiated Zircaloy may sustain >10% strain without rupture, while high burnup fuel may fail at 4% strain. Because of irradiation embrittlement, rupture is more likely in the central fuel interval of each rod where burnup is greatest, than at the ends of the fuel region or in the plenum section. Thickness of the oxide layer may also be a factor in thinning of the cladding. Higher average burnup increases oxide thickness, but experiments have shown only weak correspondence of oxide

thickness with position in the reactor and measures of average burnup (Balfour et al. 1992; Motta et al. 2015). Note that cladding creep can occur at any time before and during disposal and does not require waste package breach.

Tensile stress magnitude in the Zircaloy (hoop stress) of less than 90 MPa has been shown to substantially reduce the rate of creep strain accumulation. Hoop stress is less than 90 MPa for the great majority of spent fuel cladding even at elevated temperature up to 350°C, and virtually all cladding at lower temperatures. Models are available to predict creep strain accumulation as a function of burnup and cumulative time-temperature exposure. The phenomenology is relevant to disposal criticality primarily because of the elevated temperature, and the potential for long exposure time.

### **Correlation Model and Creep Law Based on Experimental Creep Test Data**

The following discussion is taken from *Clad Degradation – Summary and Abstraction* (Siegmann 2000a). The cladding degradation model was based on experimental work on nonirradiated cladding material from Murty (source as cited) modified for the effects from irradiation in reactor service. The abstraction approach analyzed typical repository cooling histories and integrated a laboratory-based creep rate law with Arrhenius dependence on temperature, to estimate accumulated strain. For implementation in performance assessment (PA) for the Yucca Mountain Site Recommendation (SR), the total creep strain was correlated to peak waste package surface temperature (a quantity that was also calculated for the PA). This abstraction approach would be impractical for criticality effects modeling because peak temperature is not generally correlated with time-temperature exposure associated with a succession of criticality events. Note that a simpler bounding statement of cladding failure was used for the Yucca Mountain License Application PA.

For implementing cladding creep and rupture in a fuel degradation model, the best approach would be to select a creep constitutive model that represents the strain rate laws from the Modified Murty correlation (Siegmann 2000a, Section 6.2). This would be combined with an abstraction of yield strain at rupture (e.g., Siegmann 2000a, Figure 7).

## **2.2 Initially Failed Cladding**

If cladding creep rupture slows to insignificance under disposal conditions, and possibly even at temperatures associated with a succession of criticality events, then the fraction of initially failed fuel rods could be an important determinant of fuel performance. Rod failures from dry storage (0.045% of rods failed or approximately 2.4 rods per 21-PWR size waste package [WP]) and transportation (vibration and impact, at 0.01% of rods failed, or 0.6 rods per WP) are included in the distribution of failures in existing fuel (Siegmann 2000a). The great majority of flaws in failed cladding (except for early fuel discussed below) probably consist of fine cracks or pinholes, some of which are undetected. These best-available data are suitable as modal values in distributions of uncertainty on initial cladding failures. In contrast to these values, the BSC (2005a) fuel-in-air report reviewed cladding failure data and estimated 1 to 2 failed rods per PWR fuel assembly. These data need to be reconciled for use in modeling source term changes due to potential criticality events.

Fuel with high failure rates included boiling water reactor (BWR) fuel from 1970 and also 1973-1976, and pressurized water reactor (PWR) fuel from 1972, 1983, and 1989 (e.g., BWR fuel discharged in 1970 with 4.5% of the rods failed) (Siegmann 2000a). The nature of damage varies

from pinhole flaws to larger gaps with growth of UO<sub>2</sub> alteration products. Such fuel has likely been placed in the same storage canisters (and not dispersed throughout a larger population of canisters with undamaged fuel). Hence, the number of canisters containing early fuel with high failure rates is relatively small, and these canisters can be dealt with separately in any model of fuel degradation. Ultimately, they could be classified as damaged fuel and packaged differently for disposal.

### **2.3 Cladding Corrosion Mechanisms**

This section discusses other mechanisms that could potentially result in cladding perforation, including external Zircaloy oxidation, localized corrosion, delayed hydride cracking, and stress corrosion cracking (SCC). Internal attack (fuel-side corrosion) may also occur from reaction with fission products, particularly cesium and iodine. Of these, oxidation and localized corrosion are most appropriate for consideration in response to disposal criticality, because of elevated temperature and the potential for evaporative concentration of solutes during repeated, episodic heating events.

#### **Water-Side Zircaloy Oxidation**

Hillner et al. (1994) summarized the external corrosion behavior of Zircalloys in water. This mechanism conserves the Zr, while adding O to produce weight gain. The ZrO<sub>2</sub> oxide film is black, and adherent up to reactor burnup of about 55 GW-d/MT, when scaling begins to occur. Scaling was observed to affect only the outer portion and not the full oxide layer.

Corrosion of fresh, clean Zircaloy is more rapid for the first few microns, then exhibits a transition to a slower, constant rate of weight gain when the oxide film thickness is about 25 μm. (A weight gain of 378 mg/100 cm<sup>2</sup> = 16.8 μm of metal consumed.) Pre-transition stages (and early post-transition stages, if any) produce minor changes in oxide layer thickness and can be ignored for this discussion.

Based on review of previous testing, and long-term testing of non-irradiated Zircalloys in water (Hillner et al. 1994) the post-transition kinetics exhibit two stages. For the later stage, the incremental change in weight is linear with time, with an Arrhenius temperature dependence ( $E_A = 95.2$  kJ/mole). The supporting test data are limited in duration and must be extrapolated two orders of magnitude for application to repository problems. Assuming a cladding temperature of 180°C for 10,000 years in a repository, oxide thickness growth on the order of 0.3 to 3 microns is predicted. This is a minute increase in oxide layer thickness, such that Zircaloy oxidation in water or steam can be neglected for modeling of postclosure criticality, unless temperatures greater than approximately 300°C are sustained.

#### **Localized Corrosion**

The following discussion was excerpted from BSC (2005b) which is a cladding degradation abstraction report authored by David Stahl.

Zirconium alloys are susceptible to pitting in aggressive solutions of chloride ions, ferric ions, or hydrogen peroxide. Based on review of testing literature, failure criteria were constructed based on an electrochemical definition of pitting as the condition at which the corrosion potential exceeds repassivation potential (i.e.,  $E_{\text{corr}} > E_{\text{rp}}$ ). Electrochemical values were obtained for Zr alloys in various solutions containing these species. The model to predict repassivation potential depended only on chloride concentration whereas the corrosion potential model depended on all three. Using

the regression model with solution conditions developed for the repository (not evaporatively concentrated) no cladding failures were predicted.

However, evaporative concentration of ground water in a breached WP in an unsaturated repository could lead to accelerated corrosion of Zr alloys. Bale (2000) reviewed laboratory testing data for general corrosion (weight loss) and localized corrosion (pitting) at extreme solution conditions (chloride, fluoride, ferric ion, acidic pH). Test results are reported for various Zr alloys, surface finishes, and temperatures. The author states that: "...the corrosion and pitting rates may be in the acceptable range provided the HCl concentration is 20% or less, the ferric ion concentration is 50 ppm or less, and the temperature is less than 60°C." The "acceptable range" in this usage refers to the Hillner et al. (1994) model discussed above, for general corrosion of Zircalloys in water or steam.

SNF cladding is invariably pickled (soaked in acid) prior to use, and pickling was found to confer significant resistance to ferric ion at acidic conditions, at least for short term tests.

With regard to fluoride and pH effects Bale (2000) wrote: "If the pH is maintained below 3.18 [from Pourbaix analysis] and the HF/fluoride ion concentration remains above 5 ppm, then the [general] corrosion rate will be greater than 100  $\mu\text{m}/\text{year}$ ...If the pH is greater than 3.18, the fluoride concentration is greater than 5 ppm and the temperature is less than 55°C, then the corrosion rate is estimated between that calculated from the Hillner [1994] equation [for general corrosion in water or steam] and 7  $\mu\text{m}/\text{year}$ ...The same assessment is made if the temperature is between 55 and 100°C and the fluoride concentration is 100 ppm or less..." The data summary thus showed that rapid corrosion of Zr alloys (on the order of 10  $\mu\text{m}/\text{yr}$  or greater) is possible with solution conditions that can be produced by evaporative concentration of ground waters.

In a report for the Yucca Mountain SR, Siegmann (2000b) stated that: "...notwithstanding that no localized corrosion failures were predicted, localized corrosion has not yet been ruled out for localized and/or non-equilibrium effects including extreme concentration by evaporation. A number of mechanisms may locally depress the pH or increase the concentration of corrosive species such as fluoride or chloride, causing localized corrosion (pitting or cracking) to begin...until they can be ruled out, or shown to be too transitory to have negative consequences on cladding, a conservative model has been adopted..." The report goes on to describe a conservative mass balance between the fluoride flux incoming with ground water, and the dissolution of Zr.

Recognizing that concentrated solutions will cause the rate of localized corrosion to increase steeply, an approximation can be taken whereby evaporative concentration, with evaporation driven by a fraction of the heat produced by criticality events, is used as a surrogate for aggressive corrosion conditions that cause accelerated corrosion of Zircalloys. Based on the foregoing analyses, when enough evaporation has occurred in the WP to produce any of the following conditions, all fuel rods in a WP could be assumed to be perforated:

- > 5 ppm HF or fluoride, and pH < 3.18
- > 5 ppm HF or fluoride, pH > 3.18, and T < 55°C (somewhat accelerated up to 7  $\mu\text{m}/\text{yr}$ )
- > 5 ppm HF or fluoride, pH > 3.18, and T > 55°C (accelerated)
- > 300 ppm chloride (contributes to acidic pH and provides the counterion for ferric ion complexation from steel corrosion)

- $\text{pH} < 3$  (associated with concentration of chloride)
- $\text{pH} > 12$  (hydroxide complexes form such as  $\text{LiOH}$ )

Note that in the presence of chloride at  $\text{pH} < 3$ , ferric ion is likely to be produced from corrosion of steels, and that  $\text{Fe}^{3+} > 100$  ppm can initiate localized corrosion of Zircalloys. This condition is represented here by the evaporative concentration of chloride. The concentration of 300 ppm allows sufficient chloride to make  $\text{pH} < 3$  (absent cations) plus provide chloride for ferric chloro-iron complexes. Each of these evaporative concentration factors, and associated species concentrations and pH values, should be verified using a geochemical modeling code and representative starting ground water compositions.

Evaporative concentration pertains to an unsaturated repository whereby ground water enters a WP, but only steam and air egress (e.g., during criticality events). For saturated conditions there is no boiling to separate solvent from solute, and some solution exchange is likely with the surrounding near field because of thermal expansion. For example, heating by  $200^\circ\text{C}$  under moderate pressure (prevents boiling) causes water expansion of more than 4%. Heating beyond the boiling point ( $264^\circ\text{C}$  at 50 bar hydrostatic ground water pressure) could result in evaporative concentration, but the mass expelled from the package would likely contain liquid as well as steam. For saturated conditions evaporative concentration can therefore be ignored, except that aggressive chemistry may occur when the ground water already contains elevated concentrations of fluoride or chloride and is heated by criticality.

### **Hydride Reorientation and Delayed Hydride Cracking**

Delayed hydride cracking has been analyzed in terms of stress intensity and found to be unlikely even at elevated temperature, so that only a small fraction of fuel (0.01%) could be affected. For modeling of fuel/basket degradation the mechanism of delayed hydride cracking can be ignored, and the potential impact on cladding integrity incorporated into the uncertain initial failed cladding distribution.

Ahn et al. (2018) concluded that temperatures are too low during storage and disposal for reorientation leading to cracking or delayed hydride cracking, and that even if reorientation did occur the effect on cladding strength would likely be negligible.

### **Stress Corrosion Cracking of Cladding**

Stress corrosion cracking has been investigated as a potential mode of fuel-side cladding failure, from fission product iodine and cesium (see analysis by Siegmann 2000a). Tensile stress of 180 MPa in the cladding is reportedly required (i.e., twice the threshold for cladding creep), and sufficient concentration of iodine, or by analogy, chloride. Stress corrosion cracking (water-side) would require an aqueous phase with elevated chloride concentration, elevated temperature, and sufficient tensile stress. As discussed for cladding creep, such stresses are higher than those expected to predominate in actual cladding, even at elevated temperature. Hence SCC is unlikely if temperature is limited (as would be the case for criticality events in an unsaturated repository with maximum temperature limited by boiling) or there is a constant supply of diluent ground water (saturated repository). Note also that the conditions that cause external SCC are also conducive to other modes of localized corrosion.

## 2.4 Axial Splitting Model for Unsaturated, Oxidizing Conditions

When rupture or perforation of cladding occurs in air (or humid air), oxidative reaction of the UO<sub>2</sub> fuel causes swelling and axial splitting (“unzipping”). The following discussion describes splitting that can occur in the unsaturated case, which has been studied experimentally. Alteration in the saturated case is controlled by UO<sub>2</sub> at reducing conditions, discussed in the next section.

The bare fuel (unclad) alteration products reported by Einziger and Strain (1986) crumbled when sampled, so by analogy, alteration products within splitting rods may also be non-cohesive and readily separate from the split cladding when it has opened sufficiently.

The mechanics of splitting were investigated by Einziger and Strain, who found that when splitting ensued from a small crack (ranging from 8 to 37 μm) that circumferential average strain was only on the order of 1%, requiring alteration of only ~20% of the UO<sub>2</sub> in cross section. When a larger (0.76 mm diameter) circular defect was introduced, average strain at breach was ~6.5% requiring alteration of ~80% of the UO<sub>2</sub> within (see Einziger and Strain 1986, Figure 10, for photos of damage). This indicates that the alteration products develop tractions on the internal surface of the cladding, when sufficiently confined, localizing the strain and leading to earlier splitting from smaller defects.

Splitting rod failure occurs in two steps, an incubation phase in which the fuel matrix degrades and swells at the location of a small cladding perforation, and a splitting phase when the oxidative reaction proceeds in both directions down the rod, facilitated by propagation of tensile cracks. The split cladding is further pushed apart by expansive alteration of the fuel.

The incubation phase was approximated by Einziger and Strain (1986) using observations of spallation of bare (unclad) UO<sub>2</sub> fuel, and the resulting Arrhenius rate law has strong temperature dependence. The time-to-splitting after perforation was projected to be a few weeks at high temperature (283°C) but more than a million years at 100°C.

Once splitting begins the rate is also temperature dependent in oxidizing conditions (e.g., humid air). A simple approximation assumes alteration of disk cross-sections as splitting proceeds in both directions down the rod (Siegmann 2000a; Stout and Leider 1998). An abstraction for PA combined rates calculated using three different methods, in a triangular distribution. Each fuel rod could be classified as either intact, unzipping, or exhausted.

The temperature dependence of splitting based on observation of artificially split samples of irradiated fuel, was plotted by Einziger and Strain (1986, Figure 11). For splitting to occur at a rate that is significant to repository performance, elevated temperature >100°C is required. In their analysis, Stout and Leider (1998) ignored the splitting time, focusing only on the time-to-splitting as discussed above.

Argonne National Laboratory performed fuel degradation tests with two intentionally failed fuel segments in humid air at 175°C (Cunnane et al. 2003). These conditions are more severe than the repository conditions. The cladding on both of these test samples split axially in less than two years. Assuming propagation velocity of 2 cm/yr, the rate converts to  $3.8 \times 10^{-6}$  cm/min and the inverse temperature is  $22.3 \times 10^{-4}$  K<sup>-1</sup>, which plots on an extrapolation of the trend identified by Einziger and Strain (1986, Figure 11). Transmission microscopy of these samples suggests that the active alteration phase in the fuel segments was the fuel-side cladding (ZrO<sub>2</sub>) rather than the UO<sub>2</sub> (Brady Hanson, personal communication, 22May2019).

## **2.5 Axial Splitting Model for Saturated, Reducing Conditions**

The rate of UO<sub>2</sub> fuel matrix reaction is controlled by chemistry, particularly the availability of oxidizing species from radiolysis, and the fugacity of H<sub>2</sub> in the WP from radiolysis and from corrosion of aluminum- and iron-based materials. The presence of sufficient H<sub>2</sub> lowers the electrochemical potential and reacts with oxidants in a manner that is catalyzed by noble-metal (fission product) particles in the fuel matrix, thus limiting oxidation of UO<sub>2</sub>. This process and the resulting fuel reaction rate is described by the fuel matrix degradation model (FMDM). In its original form (Jerden et al. 2015) the FMDM used temperature and alpha flux (Gy sec<sup>-1</sup>) at the reacting surface of the fuel, to describe the UO<sub>2</sub> corrosion rate (g m<sup>-2</sup> yr<sup>-1</sup>). Both temperature and alpha flux decay with time, so that the fuel dissolution rate decays by several orders of magnitude from as great as 10 g m<sup>-2</sup> yr<sup>-1</sup> at very early time to as low as 10<sup>-2</sup> to 10<sup>-6</sup> g m<sup>-2</sup> yr<sup>-1</sup> after 10<sup>4</sup> to 10<sup>5</sup> years. Note that early time predictions may not be relevant to repository conditions because WPs will be intact. The evolution of the dissolution rate depends on the concentrations of H<sub>2</sub> and carbonate (CO<sub>3</sub><sup>-2</sup>) in solution, and the abundance of catalytic noble metal particles in the irradiated fuel.

The availability of H<sub>2</sub> in the WP during degradation is a key factor in the FMDM fuel dissolution rate, which was represented by assumed concentration values in the initial reported results. Subsequently, Jerden et al. (2017, Figure 19) coupled the FMDM to a corrosion calculation for cladding, basket, and canister materials (Zircaloy 4, carbon steel, and stainless steels) that produce H<sub>2</sub> from aqueous corrosion in reducing environments. The hydrogen input is used in an FMDM simulation of the fuel dissolution rate, using both a closed boundary condition (no H<sub>2</sub> escape) and an open condition (Jerden et al. 2017, Figure 20).

The FMDM was developed to understand UO<sub>2</sub> alteration in a water-filled WP, with small package breaches limiting leakage and supporting a reducing environment. The predicted fuel dissolution rates are comparable to other reported data and models for spent fuel, but quite small. Experimental validation of the FMDM is in progress. A fuel dissolution rate of about 1 g m<sup>-2</sup> yr<sup>-1</sup> is near the upper end of the calculated range, and corresponds to ~10 μm/yr of UO<sub>2</sub> surface retreat with conditions of maximum temperature and alpha flux. If this process controls axial splitting of perforated fuel rods, then on the order of 10<sup>5</sup> yr would be needed for a fuel rod to split completely. Using estimates for corrosion rates of materials in the WP, H<sub>2</sub> production ends after a few thousand years, so the fuel dissolution rate increases, but temperature and radiolysis have also decreased so the fuel degradation rate is still small.

For fuel/basket degradation modeling (Sections 4 and 5) a simple way to include insights from the FMDM and the package corrosion mass balance, would be to set the rate of retreat for UO<sub>2</sub> dissolution in a splitting fuel rod to a reasonable upper bound (e.g., 10 μm/yr). This would be for later time when the fuel has substantially cooled, but the production of H<sub>2</sub> has decreased (the reactions are thermally activated, but the Jerden et al. 2017 examples are for 25°C).

## **2.6 Fuel Assembly Spacer Grids and End Nozzles**

The following discussion is based on a general description of a typical Westinghouse 17×17 PWR fuel assembly (Westinghouse 2009). Fuel assembly geometry, number of rods, water channels, control rod thimbles, nozzle details, etc., differ between fuel vendors and between PWRs and BWRs.

Fuel assemblies have water-permeable spacer grids made from formed metal sheet (typically Zircaloy or stainless steel) approximately every 0.5 m along the length, except at the ends. Spacer grids are made from tough materials with low corrosion rates, and generally do not fail in service. In addition to alignment, they have many small vanes that mix coolant flow. They can be represented by deformable connections or grid blocks between fuel rods. They hold fuel rods loosely and only in x- and y-directions, so that rods can slip out (this is done deliberately when fuel assemblies are disassembled). Rods are held loosely but stiffness increases steeply as the distance decreases between adjacent rods. There is coupling between rods whereby loads can be transmitted to the spacer grids and transferred to other rods. Grids are held in place axially by attachment to the guide tubes. Corrosion of spacer grids is possible, and gross damage will ensue when the surface retreat reaches approximately half the thickness (corrosion occurs on both sides). Typical thickness is 500  $\mu\text{m}$ .

The end nozzles are typically Type 304 stainless steel castings with cavities to hold rod ends, springs and dashpots to control fuel rod movement, and nozzle openings to direct coolant water. Springs and bolts are typically made from Inconel. The bottom and top nozzles also anchor guide tubes (or tie rods in BWR fuel) that are distributed in the pin array and hold the assembly together. For PWR assemblies the guide tubes also guide control rod insertion from above, in the reactor. Fuel assemblies are lifted by the top nozzle, and the weight of fuel rods is borne by the bottom nozzle, which is attached to the top nozzle by the guide tubes/tie rods.

Whereas the grid spacers are deformable, the nozzles are massive and stiff, and will have extended mechanical lifetime in the disposal environment. Note that nozzles have been known to fail by stress corrosion cracking in the reactor/fuel pool environment, when boric acid is used. Nozzles can be represented as relatively heavy, solid blocks that attach to the guide thimbles and restrain fuel rod ends, except that rod ends can slip in the z-direction (and can potentially slip out of the nozzles). The mechanical lifetime of nozzles in a repository would be subject to considerations of volume, surface area, and general corrosion rate.

The foregoing description of a PWR 17 $\times$ 17 fuel assembly is representative of other PWR assemblies (mainly 14 $\times$ 14) and to some extent BWR fuel (ranging from 7 $\times$ 7 to 10 $\times$ 10 fuel rod arrays). However, BWR assemblies are smaller and generally do not include guide tubes for reactor control rods, but use cruciform control blades that move up and down between groups of four assemblies. BWR assemblies may also have “water rods” or cavities designed to improve moderation along the length of the assembly, and they also have a “fuel channel” which is a metal sheath wrapping the entire assembly, that guides coolant flow.

## **2.7 General Corrosion Models for Basket Materials**

Baskets are of two types: egg-crate and tube-and-plate, with variations. The egg-crate design is simplest, consisting of parallel, longitudinal plates that extend the full length of the basket, which are indexed together to form a rectilinear array. Each square cell in the array accommodates one fuel assembly. Additional smaller plates may be used around the edges to stabilize the geometry and to attach the basket to the DPC shell. The egg crate is fabricated either by using a combination of full-width and folded plates welded together, or by using full-width plates with indexing notches. The longitudinal plates are typically about 1 cm thick and made from 304L stainless steel (e.g., in the NAC International TSC series of DPCs) or from an aluminum-B<sub>4</sub>C composite (e.g., the Holtec Metamic-HT® basket available in the MPC series).

The tube-and-plate type of basket consists of stainless steel guide sleeves for each fuel assembly, held in place by spacer plates. Most of these baskets are used in the NUHOMS® series of DPCs manufactured by Transnuclear. The guide sleeve wall thickness is small, on the order of 2.5 to 5 mm (e.g., NUHOMS 24P canister, Transnuclear 2004). The spacer plates are arranged approximately every 50 cm along the length of the basket (corresponding to the distance between fuel assembly spacer grids) and each spacer plate has square cutouts for each fuel assembly guide sleeve. Some spacer plates are made from Type 304 stainless steel, some are plated carbon steel (save material cost and improve thermal conduction while preventing corrosion in fuel pools), and some may be aluminum thermal shunts depending on the design. Spacer plates are typically the thickest components (e.g., 2 cm) used in any DPC basket, for structural support of the fuel guide sleeves with small ligaments between cutouts. Because of the thickness, baskets with stainless steel spacer plates may maintain the fuel geometry longer than any other type of basket. Support rods are used to attach the plates together in a stiff assembly, to maintain the basket structure during operations, storage, and transport. A variant of the tube-and-plate basket is a tube-and-rail configuration in which the guide sleeves are held in place by an egg-crate structure supported by metal rails.

A key element of modern basket designs is neutron absorber plates. This discussion focuses on absorber plate designs and neglects earlier flux-trap designs because they represent a small fraction of the total DPC fleet. (Flux traps have been abandoned in newer DPC designs because they take up extra room.) Each fuel assembly must be separated from each neighboring assembly by an absorber plate. Egg-crate baskets with stainless steel plates use thin sheets of Boral® (aluminum-B<sub>4</sub>C composite) that are held in place by thin cover sheets (“wrappers”) of stainless steel, tack-welded at the edges to basket plates. The tube-and-spacer baskets in more recent designs use absorber plates (typically Boral®) attached to guide sleeves in a similar manner.

These arrangements produce galvanic cells in which the aluminum-based material corrodes preferentially, protecting the stainless steel around it. Hydrogen gas is produced, which has caused blistering under the cover sheets where the method has been used in fuel pool storage racks. Future modeling of this mode of corrosion degradation will be challenging because of the spatial resolution needed to represent the cover sheets.

An important deviation from the use of Boral® absorber plates is the Metamic® or Metamic-HT® basket (Holtec) in which the basket plates serve both structural and absorber functions. We note that early DPC and bolted-cask designs used borated stainless steel absorber plates, but these did not prove commercially viable and were never put into service, or their numbers were quite limited.

For modeling, Metamic® or Metamic-HT® basket plates are simplest to represent numerically, with fewer elements than Boral® sandwiches.

Degradation of all of these basket materials can be treated using a 1-D general corrosion model with appropriate constant corrosion rates (applicable after initial phases of corrosion, oxide layer buildup, etc., have occurred). Localized corrosion and (e.g., pitting and crevice corrosion) will also occur with passivated materials, but are not expected to reduce the active thickness of absorber plates.

The classic 1-D model for the extent of diffusion-limited surface retreat has a  $t^{1/2}$  time dependence and is proportional to the reactant species diffusivity in the altered layer (Crank 1956, Equation 7.77):

$$X = \sqrt{\frac{2DC_1t}{W\rho}} \quad (1)$$

where

- $D$  is the effective diffusion coefficient for a reactive mobile species diffusing through a corrosion product layer,
- $C_1$  is the concentration of the reactive species at the outer surface of the altered layer,
- $W$  is the mass fraction of the reactive species in the corrosion product layer, and
- $\rho$  is the density of that layer.

This equation is a simplification that applies if  $C_1 \ll W\rho$ , and it means that the concentration gradient in the altered layer is uniform. This function was developed originally to represent metal tarnishing by oxygen moving in the air-filled porosity of the altered layer. It can also represent an oxidizing species diffusing through water-saturated porosity, where a diffusion-limited decrease of the corrosion rate is observed over time.

Data fits have also been proposed using metal loss vs. log time (Bezins et al. 1977; long-term kinetics) of the form

$$A = B \log t + C \quad (2)$$

where for long-term kinetics (after initial oxide layer formation) the value of  $B$  is constant, while  $C$  is small compared to the long-term accumulation of corrosion product. The tests also demonstrated significant dependence of corrosion rates on pH and the presence of chloride. Elevated temperature and additions of nitrate and sulfate are probably also factors but were not addressed in the experiments (testing performed at 50°C).

In summary, metal general corrosion is generally pH and temperature dependent, and sensitive to anionic species such as chloride. Many DPC basket and shell materials are passive so that they can undergo localized corrosion cracking and pitting, but these modes can be assumed not to result in absorber depletion or basket collapse. Various functional forms are available for the evolution of long-term corrosion rates, and model formulation should include terms that can be parameterized from experimental studies reported in the literature.

## 2.8 Cladding Bending and Shear (Seismic Loads)

The following discussion is excerpted from Ahn et al. (2018).

For laterally-supported fuel subjected to side-loading (i.e., horizontal fuel subject to vertical or transverse accelerations) the fuel rods are subjected to both bending and shear forces imparted by the nozzle blocks and spacer grids. The structural response depends on whether the cladding is bonded internally to the fuel pellets.

Because the fuel behaves in a brittle manner while the cladding behaves in a ductile manner, virtually all of the bending tensile stresses will occur in the cladding. The cladding and fuel will resist shear forces from side loading, but for simplicity it can be assumed that all of the shear is resisted by the cladding. Scoping calculations show that during a side-drop event a uniformly loaded fuel rod spanning multiple grid spacers would have maximum tensile stress due to bending that is an order of magnitude greater than the maximum tensile stress due to shear.

In bending of fuel rods, there is no composite action for cladding and pellets. This is because the cladding and pellet column lie on the same bending axis. This means they act independently in bending whether bonded or not, and the flexural rigidity overall is the sum of the contributions from cladding and pellets. Hence, flexure of an intact fuel rod can be represented by an equivalent cylinder with the appropriate rigidity. Tensile strain from bending in the cladding can be calculated from curvature and compared to rupture limits. Similarly, shear loads can be applied across the cladding cross-section and compared to shear strength limits. Simulating an intact fuel rod with solid elements also represents the action of fuel pellets to stabilize gross flattening deformation of the cladding.

During bending, failure of the fuel pellets, which are more brittle than cladding, produces localized and immediate tensile loading of the cladding. When a crack forms in the fuel, shears develop between the adjacent pellets and the cladding, in response to the tension in the cladding. Exceeding the cladding tensile strength, and/or any local damage at this site such as a pinhole, will tend to produce a crack. This behavior is known to occur (cladding cracks tend to form at pellet joints or fractures) but difficult to detect during bending tests that primarily measure average curvature. It is different from pellet-cladding-interaction, which is fuel-side tensile failure (stress corrosion cracking) that occurs in power reactors subject to rapid power increases.

## **2.9 Summary of Degradation Processes for Modeling**

Degradation of fuel rods occurs initially in-reactor and is temperature and radiation dependent, so that cladding degradation essentially stops after removal from the reactor as long as the fuel is stored either dry or in fresh water, at limited temperatures. The initial, irradiated condition of Zircaloy cladding includes:

- Irradiated texture, with Zr-hydride buildup near the external surface.
- Sparse localized corrosion internally (fuel-side) from attack by fission-product iodine and cesium, which does not penetrate the cladding thickness.
- Some circumferential plastic creep of cladding in response to internal gas pressure.
- A few rods damage initially by pitting or cracking, manufacturing defects, or abrasion during fuel handling.

Of these, the most important mechanisms for modeling fuel degradation are believed to be cladding creep (mainly circumferential but also axial), and localized corrosion in response to aggressive chemical conditions. Once a fuel rod is breached by either mechanism, then the UO<sub>2</sub> begins to alter oxidatively, which leads to swelling of the rod around the breach. This can lead to axial splitting (“unzipping”) in unsaturated, oxidizing conditions, but not in saturated, reducing conditions. All degradation processes are temperature dependent, while corrosion also depends on moisture and the chemical environment.

The key processes for modeling fuel degradation are then: 1) cladding creep leading to a critical rupture strain (time-temperature exposure dependent); 2) localized corrosion (pitting or cracking) that is insignificant in fresh water at any temperature but occurs rapidly if the chemical environment concentrates to certain levels; and 3) axial splitting that starts at any cladding penetration, with delayed onset, that proceeds relatively rapidly in unsaturated conditions at elevated temperature.

When failure of a fuel rod occurs either by creep or localized corrosion, then axial splitting follows particularly in unsaturated conditions. A small fraction of fuel rods are already perforated when initially sealed into the canister (approximately 0.1% to 2% depending on fuel type, origin, and age) but do not degrade further while the canister is intact. After WP breach, these rods would likely be the first to degrade, possibly exhibiting axial splitting. This conceptual model of initially failed fuel rods and degradation processes is assembled from a rich literature of various experimental and modeling studies focused on Zircaloy cladding performance in reactors, extended to performance in a repository.

Basket structural components (tubes, plates, and bolts) made from stainless steel, carbon steel, aluminum-based material, or Inconel will undergo general corrosion according to rate laws that are limited by diffusion of reactants (oxygen, water) through corrosion products. The classic 1-D model for diffusion-limited surface retreat has a  $t^{1/2}$  time dependence and is proportional to the reactant species diffusivity in the altered layer. Data fits have also been proposed using metal loss vs. log time. Metal corrosion is generally pH and temperature dependent, and sensitive to anionic species such as chloride. Many DPC basket and shell materials are passive so they undergo localized corrosion, but the associated modes of degradation are assumed to be relatively minor.

### 3. Model Scoping

Jason Furtney, Branko Damjanac, Varun, and Azadeh Riahi (Itasca Consulting Group) and Ernest Hardin (Sandia National Laboratories)

Three models have been developed to represent degradation of fuel assemblies, fuel baskets, and the canister/waste package shell:

**Fuel Assembly Cell Model:** Represents the behavior of neutron absorbers, fuel rods, and the basket around a single cell in a DPC basket, after moisture invades the WP.

**Basket Degradation Model:** Simulates structural failure and disaggregation of basket structural elements and fuel assemblies, and their configuration as they fall under gravity within the canister.

**Waste Package Breach Model:** Evaluates how pressure within the canister (in response to rapid heating) affects deformation of the shell and its transmissivity.

This section discusses the methodology, parameters, and geometry for each model, and provides results and other information related to the progress made. The work has relied on Itasca software products *FLAC3D*, *3DEC*, and *PFC3D* (Itasca 2016, 2017, 2018).

#### 3.1 Fuel Assembly Cell Model

The fuel assembly cell model has two components that investigate: 1) degradation processes within the fuel assembly cell, and 2) transport of corrosion products on the length scale of a single fuel assembly cell. Figure 1 shows the internal structure of a generic canister and a close up of a single fuel assembly cell. The preliminary model described here investigates mechanisms that could give rise to early occurrence of criticality in a breached WP, for DPCs in which aluminum-based basket plates (which also serve as neutron absorbers) are the fastest degrading components.

#### Basket Material Degradation

The basket material degradation submodel is an aggregation of corrosion submodel types (e.g., adding Equations 1 and 2) with a user interface for parametric studies. The basket material is assumed to be macroscopically uniform as is the case with Metamic-HT® metal-matrix composite (MMC) used in Holtec baskets. The model output will be basket material thickness and corrosion product generation rates.

Since the model focuses on degradation of the basket, the following processes were not considered:

- Fuel rod corrosion
- Zircaloy creep
- Initially damaged cladding
- Changes in fuel properties from irradiation
- Axial splitting of fuel rods (not likely for the saturated case, and much slower than degradation of aluminum-based basket material)
- UO<sub>2</sub> alteration

Fuel degradation was not considered but may be included in the future, particularly to represent the effects of heating from criticality events.

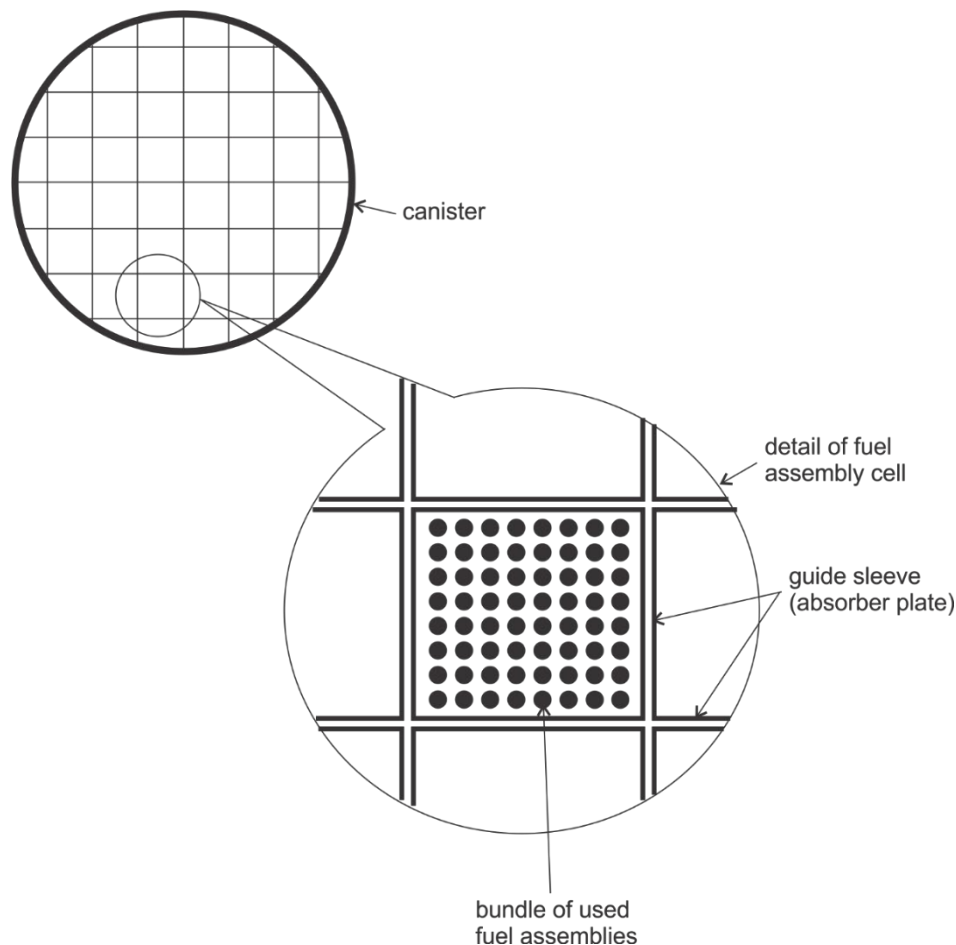


Figure 1. Typical internal structure of canister and detail of fuel assembly cell.

As the aluminum-based basket plate material degrades, it releases cohesionless corrosion product (e.g., gibbsite, or bayerite) and particles of neutron-absorbing boron carbide. The model represents how these materials are formed and transported, and where they are deposited in response to gravity and seismic motion. Itasca's *PFC3D* software was used to represent the transport and deposition of the corrosion product material. The fuel rods and basket components are fixed in this model (or they can move with a specified velocity to represent seismic motion). In the analysis the fuel cell is assumed to be filled with water because this is the condition most likely to lead to criticality. The model output is a Cartesian grid showing the relative concentrations of corrosion products/neutron absorber particles.

The model is delivered in the form of a *PFC FISH* (built-in scripting language) program.

### 3.2 Basket Degradation Model

The primary goal of this model at this initial stage of development is to represent behavior of the fuel assemblies during basket degradation and collapse processes. A two-stage modeling approach was adopted whereby a simplified initial *FLAC3D* continuum model was first developed to calibrate the effective material properties and illustrate the mechanical failure mechanisms. Based on that,

a *3DEC* model was created with explicit representation of fuel rods, spacer grids, end nozzles, and an egg-crate basket of uniform material. The main purpose of the *3DEC* model was to investigate the mechanism for collapse of the basket.

### **Initial *FLAC3D* Continuum Modeling Study**

The basket-scale *FLAC3D* continuum model consists of a section of an egg-crate type canister oriented horizontally. The model domain is a vertical slice perpendicular to the axis of the canister, representing the region between adjacent spacer grids (or spacer plates in a tube-and-plate style basket). Appropriate reflective boundary conditions are applied at the vertical boundaries of the domain. The behavior of basket plates was analyzed using a simple *FLAC3D* study of a single plate under bending and buckling conditions.

In the 3-D basket-scale continuum model, zone material properties delineate regions that represent the spacer grids, basket components, and the canister shell. Corrosion is represented by manipulating the material properties of the model components according to corrosion rate models as described previously (no elements are deleted). The model demonstrates the displacements, stress state, and coarse modes of failure of the canister and internals during progressive material degradation. This model is isothermal, and the effects of internal fluid pressure are not considered (buoyancy is included). This modeling approach stops working at large strains when the mesh becomes severely distorted; for deformation to progress beyond this point a “meshless” distinct element modeling approach is used as discussed below.

### ***3DEC* Model of Canister and Internals**

Using what was learned from the *FLAC3D* model a more detailed *3DEC* model of the canister and internals was developed. The canister shell and internal components including fuel rods, nozzles, spacer grids, and basket components were explicitly represented as discrete objects. An entire DPC shell, basket, and all fuel assemblies were represented in the model (no symmetry planes).

Although the geometric representation is more complete compared to other models, the mechanical representation is simplified. Where possible, rigid *3DEC* blocks (which are computationally efficient) with block-block hinge failure mechanisms were used to represent fuel rods and basket components. *3DEC* has the advantage of being able to handle larger deformations. As with the *FLAC3D* model, the *3DEC* model is isothermal and does not include the effects of internal fluid pressure (although buoyancy is included). The *3DEC* model can also be run in dynamic mode to simulate seismic events. Model output includes the configuration of the canister internals at time snapshots and as a function of event time during dynamic loading.

### **3.3 Waste Package Breach Model**

This is a *FLAC3D* model of a cylindrical shell, with initial breaches to represent cracks that deform with internal pressure. Initial breaches were defined as fractures running along the canister longitudinal axis (Figure 2), and in the circumferential direction. The model is elastoplastic or elastic with simulation of fracture propagation based on linear elastic fracture mechanics (LEFM). It is capable of simulating dynamic response with application of a transient pressure-time history on the inner surface of the shell.

From the inputs, the model calculates a stress history in the overpack. A fracture growth criterion is applied to the pre-existing breach to calculate the potential fracture extension. Thermal hydraulics of the water in the canister are not considered at this stage of development.

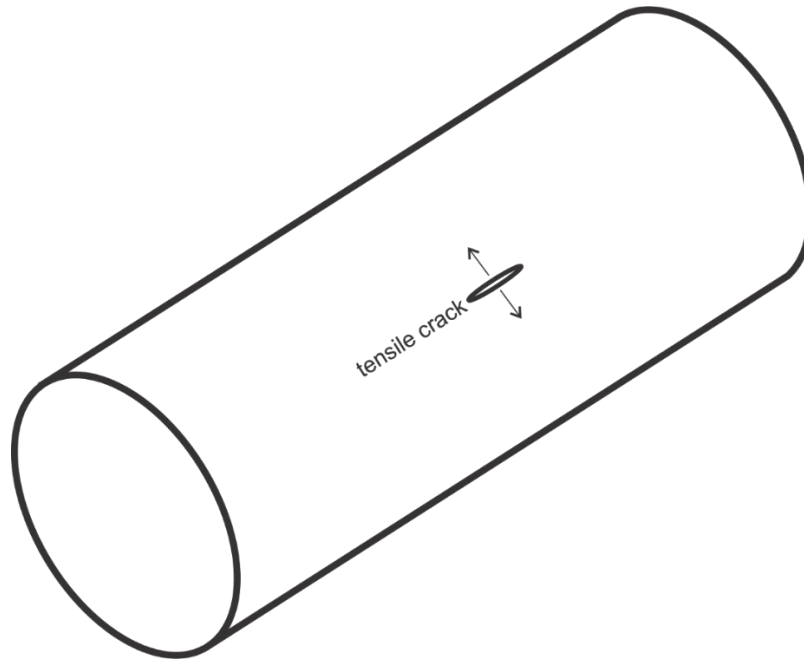


Figure 2. The geometry of the WP breach model

### 3.4 Model Parameters

The thermal and mechanical material properties for the models are listed in Table 1. Property values are for a 300 K reference temperature. Temperature-dependent values from Wolfe and Kaufman (1968) and Popov et al. (2000) are also available for use.

#### Corrosion Submodel

The corrosion rate of metals in water is generally temperature and pH dependent (and may depend on other species also as discussed in Section 2). Corrosion is expressed here as surface retreat distance (Equation 1). For longer time-scales, a log time dependence of surface retreat may be appropriate (Equation 2). Each material in the DPC can be assigned different corrosion parameter values, although simulations may be dominated by degradation of a single material such as the aluminum-based basket plates. The specific values used for corrosion parameters are not important to the simulation until: 1) time-specific projections of damage are required; and/or 2) multiple materials are involved in degradation simultaneously.

Table 1. Properties of shell, basket, and fuel materials.

Property	Value
Aluminum Young's Modulus	70 GPa
Aluminum Poisson's Ratio	0.33
Aluminum Density	2,700 kg/m <sup>3</sup>
Aluminum Specific Heat Capacity	960 J/kg-K
Aluminum Thermal Conductivity	205 W/m-K
Zirconium Young's Modulus	95 GPa
Zirconium Poisson's Ratio	0.33
Zirconium Density	6,500 kg/m <sup>3</sup>
Zirconium Specific Heat Capacity	270 J/kg-K
Zirconium Thermal Conductivity	11.2 W/m-K
UO <sub>2</sub> Young's Modulus	230 GPa (Wolfe & Kaufman, 1967)
UO <sub>2</sub> Poisson's Ratio	0.316
UO <sub>2</sub> Density	10,970 kg/m <sup>3</sup>
UO <sub>2</sub> Specific Heat Capacity	240.7 J/kg-K (Popov et al., 2000)
UO <sub>2</sub> Thermal Conductivity	3 W/m-K

### 3.4 Future Model Development

The overall approach is to improve realism of fuel/basket features and degradation processes, and to couple all the important processes that impact degradation, and ultimately, the radionuclide source term for repository performance.

The models described in this report are intended to be integrated to represent effects from corrosion, seismic ground motion, and heating by criticality events. A general approach is to apply a high-rate heating history to a sub-region of a fuel basket to represent a criticality event. The starting configuration can be intact or degraded (see Sections 4 and 5). For fluid and heat transfer, the mechanical model of the fuel and basket (e.g., *FLAC3D* continuum version, elastic and dynamic, Section 5) can be coupled with a fluid dynamics code. The choice of a fluid dynamics code is important and difficult because it must represent:

- Movement of fluid (air, water, and steam; multiphase),
- Transport of heat (conduction, convection, and possibly radiation), and
- Mass/energy transfers with the surrounding medium.

Much of the computational effort in a coupled scheme will likely be used for heat-mass transport modeling. For this study a porous-medium code was selected for coupling (Section 7). Originally developed for geothermal applications and petroleum reservoir simulation, the fully implicit, integrated finite difference, porous-medium approach incorporates rigorous equations of state for fluids (including around the critical boundary for water), but has the limitation that all parts of the problem including open spaces must be represented by porous media (i.e., with Darcy flow). Although computationally intensive, it is significantly faster than a Navier-Stokes implementation of heat-mass transport, often used for computational fluid dynamics problems. The coupled model

development work that is currently underway at ORNL faces the same choice of approaches to represent heat-mass transport in response to criticality events.

For a porous-medium approach, effective transport properties will be developed for the fuel and basket, corrosion products, and void regions of the canister. Properties will also be developed for an annular, porous region around the outside of the WP with frictional mechanical coupling, that acts as a heat sink and a source-sink for steam and water. Pressure inside the breached canister can be calculated in response to local heating, resulting in a stress history for the canister/package wall (calculated by the coupled mechanical model). A fracture-growth criterion can then be applied to the pre-existing breach to calculate dilation and extension (see Section 6), which can be used to simulate transport of fluid through the breach and the back-coupling effect on the pressure inside the canister.

## 4. Fuel Assembly Cell Model

Varun and Branko Damjanac (Itasca Consulting Group)

### 4.1 Introduction

This section presents current progress related to the numerical modeling of corrosion of neutron absorber plates and movement of corrosion products. As aluminum-based Boral® or Metamic-HT® basket materials degrade, they release cohesionless corrosion product and particles of neutron-absorbing boron carbide. Understanding how these materials are transported and where they are deposited is required for subsequent investigation of criticality risks.

There are two major types of baskets: egg-crate and tube-and-plate. The egg-crate design is simplest, consisting of parallel, longitudinal plates that extend the full length of the basket, which are indexed together to form a rectilinear array. Each square cell in the array accommodates one fuel assembly. The egg-crate design is the focus of this study. The egg crate is fabricated either by using a combination of full-width and narrower plates that are welded together, or by using full-width plates indexed with half-height notches. Typically, the longitudinal plates are approximately 1 cm thick and made from 304L stainless steel (e.g., in the NAC International TSC series of DPCs) or from an aluminum-B<sub>4</sub>C composite (the Holtec Metamic-HT® basket now available in the MPC series).

Each fuel assembly must be separated from each neighboring assembly by a neutron absorber plate. As discussed in Section 2, egg-crate style baskets can be complex to model, but MMC plates (e.g., Metamic-HT®) are simpler and more readily represented numerically with fewer elements than Boral® sandwiches. The current version of the fuel assembly cell model describes the simpler MMC basket; corrosion of the sandwich geometry can be addressed later.

### 4.2 Model Setup

Itasca's *PFC3D* software was used to represent the transport and deposition of the corrosion material. The model is templated such that the user can specify the geometry and material parameters, and then *FISH* scripting functions are used to setup and run the model.

The following are salient features and assumptions for the model.

- The model is setup as a pseudo-3D model (Figure 3). A thick slice of the cross-section perpendicular to the axis of the canister (y-axis) is modeled with periodic boundaries along the axis of the canister (y-axis), i.e., material leaving from one face will enter back from the other face. This is done to account for proper packing in 3-D. To study the effect of different orientations of the canister, the user can specify the direction of gravity (in the x-z plane). However, it is assumed that the axis of the canister stays horizontal.
- The fuel rods and basket components are fixed as rigid features in this model (although it can be run so that the fuel and basket move with seismic ground motion). The outer diameter of fuel rods, the number of fuel rods in each direction, and the spacing between the rods and between the basket plates are model parameters.
- Loose corrosion products that originate on the basket plate surfaces are simulated by generating clumps (represented by spherical particles or balls of various sizes) adjacent to the walls that represent the plates. The balls (clumps) are then allowed to move and settle, interacting with fuel rods, basket plates, and other particles representing settled material.

The radii of spherical particles and the friction coefficient between particles must be specified. The main difference between balls and clumps made of aggregated balls, is that clumps have rolling resistance because of their shape, whereas balls have no rolling resistance. In the current model clumps are made from two balls glued together, but any general clump geometry may be used.

- The fuel assembly cell is assumed to be filled with water. Buoyancy forces act on the clumps as they settle. A drag force proportional to velocity is also applied to each particle, based on Stoke's law  $FD = 6\pi\mu r v$ , where  $\mu$  is the dynamic viscosity,  $r$  is spherical particle radius, and  $v$  is settling velocity. Based on an average particle size of about 50  $\mu\text{m}$ , the terminal velocity of the particles is estimated to be in the range 0.1 m/sec to 0.01 m/sec (depending on the temperature and viscosity of water). This implies the corrosion products will settle to the bottom (with collisions) in a few seconds to about a minute. Given this slow rate of corrosion, there will not be many particles settling at the same time. A settling particle will likely interact with fuel rods, basket plates, and other already-settled particles, but not with other particles in the process of settling.
- Using this assumption, the computation time is reduced by having multiple particles settling at the same time provided they do not interact with each other. Based on the model size, the number of particles that can be generated at the same time without interacting with each other is determined. These particles are generated randomly along the length of the plates, settled, and brought to equilibrium. The "real" time is then incremented by a value equal to the time during which the mass of corrosion products equal to the mass of these particles would have been generated. This process is then repeated over and over until the desired duration of "simulated" time is reached. The logarithmic corrosion rate law is used at this point, i.e., metal loss is  $A = B \log t + C$  (Equation 2) where  $B$  is time-invariant and  $C$  is small compared to long-term accumulation of corrosion products.
- The model output is a Cartesian grid with the concentrations of the individual corrosion products and neutron absorber materials. The user can specify the grid size. A sample output for a 20 $\times$ 20 grid is shown in Figure 4.

### 4.3 Fuel Assembly Cell Model Results

Examples for both spheres and clumps are shown next. For all cases, the results are shown at the end of X, 2X, 4X and 8X years (relative corrosion rates). Figure 5 shows the results for spheres and no inclination of the fuel assembly cell. The larger concentration on the sides is because all particles generated on the side walls end up in that region. Figure 6 shows the results for spheres and 30° inclination. As expected, higher concentration is observed in the lowest corner. The results for clumps and no inclination are shown in Figure 7, and clumps with 30° inclination are shown in Figure 8. The main difference with clumps is that some clumps can be observed sticking on the fuel rods due to rotational resistance.

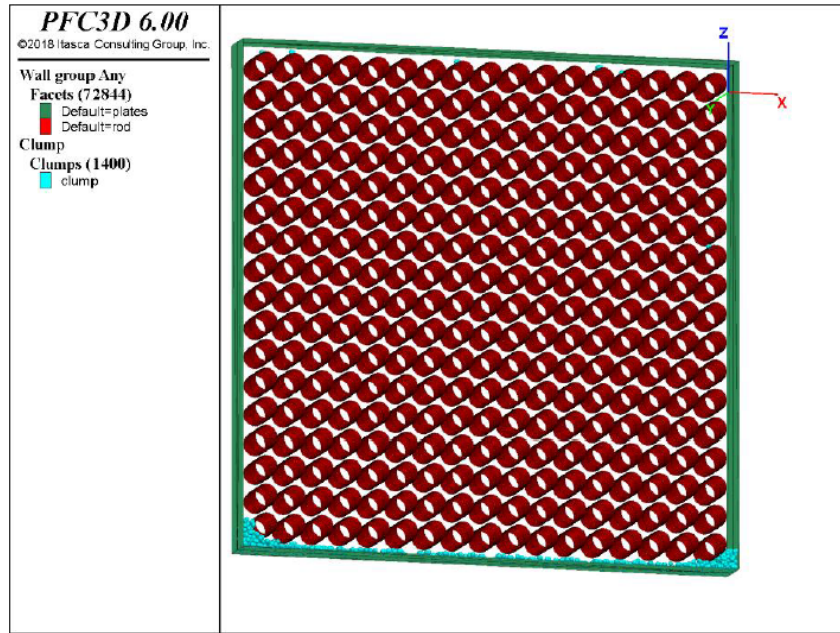


Figure 3. Model layout showing plates (green), fuel rods (red), and corrosion products (blue).

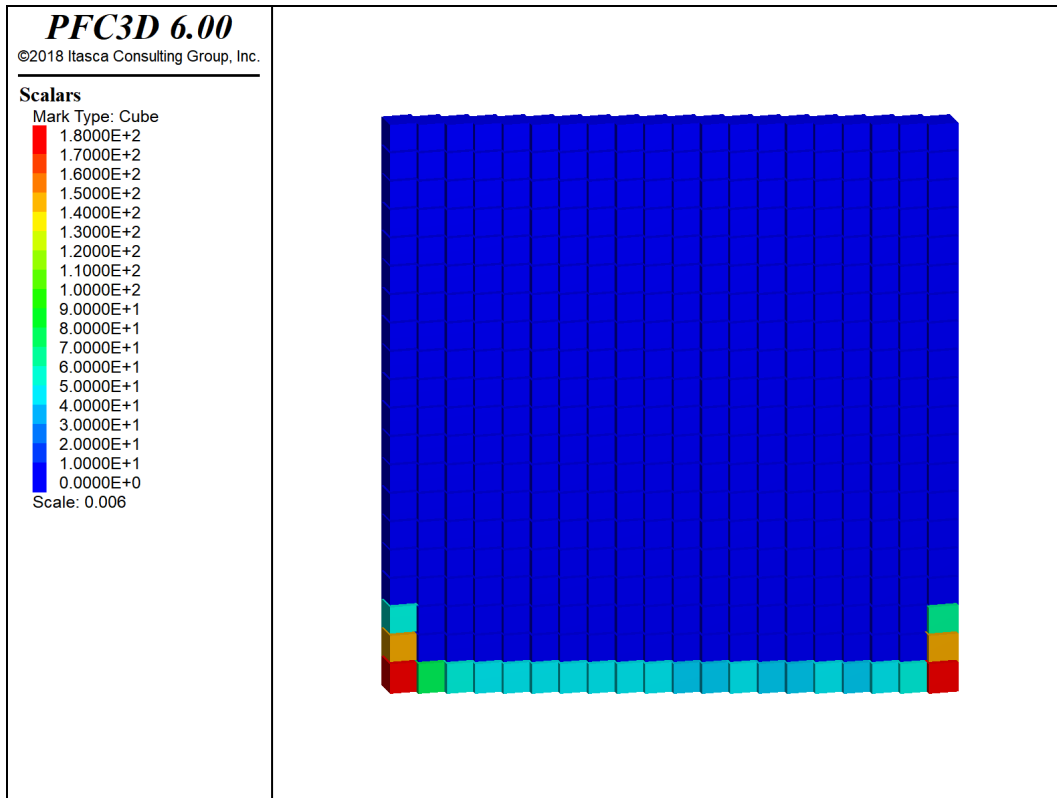


Figure 4. Model output showing number of particles representing corrosion product in each zone of the grid.

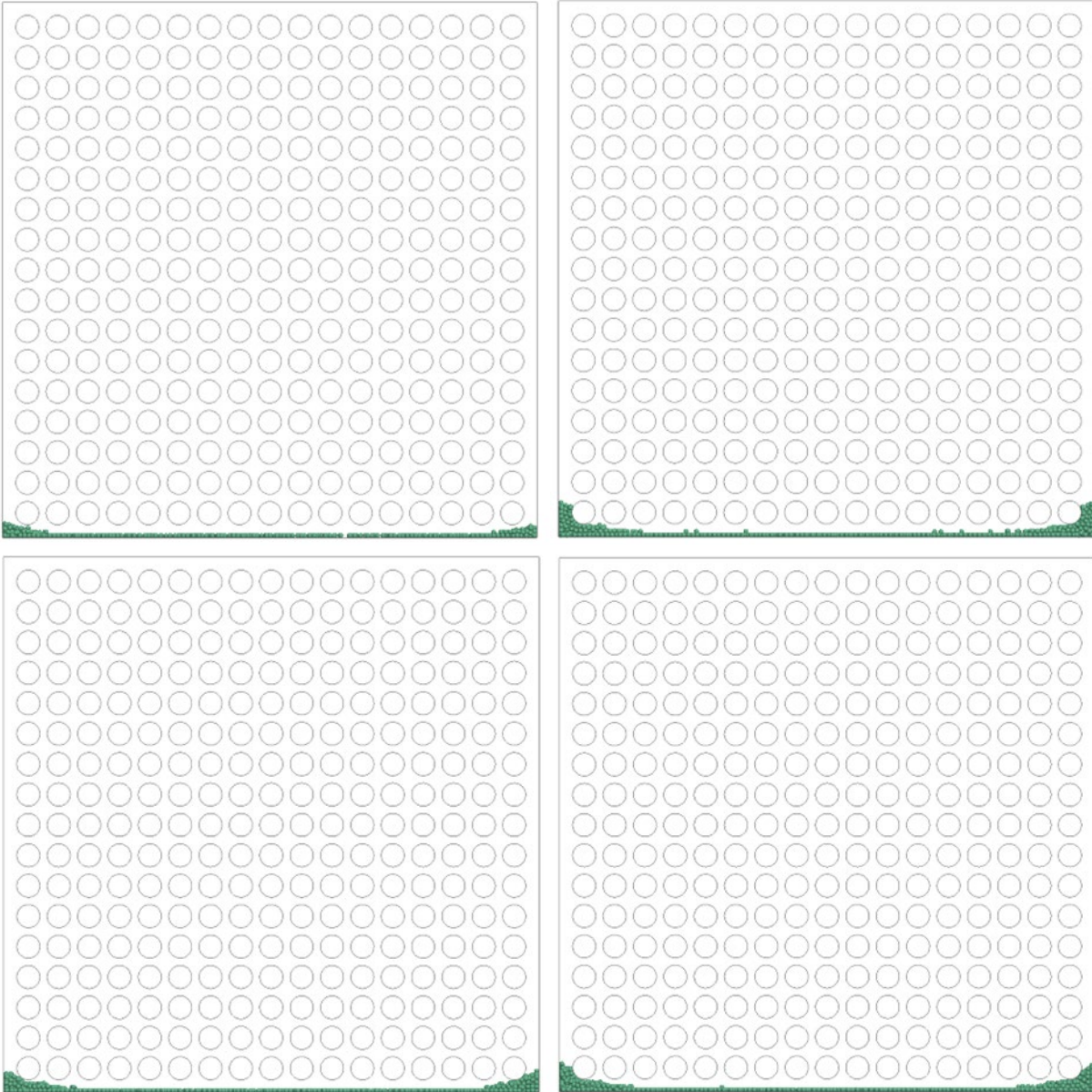


Figure 5. Corrosion products at (top left) X years, (top right) 2X years, (bottom left) 4X years, and (bottom right) 8X years for balls and 0° inclination case.

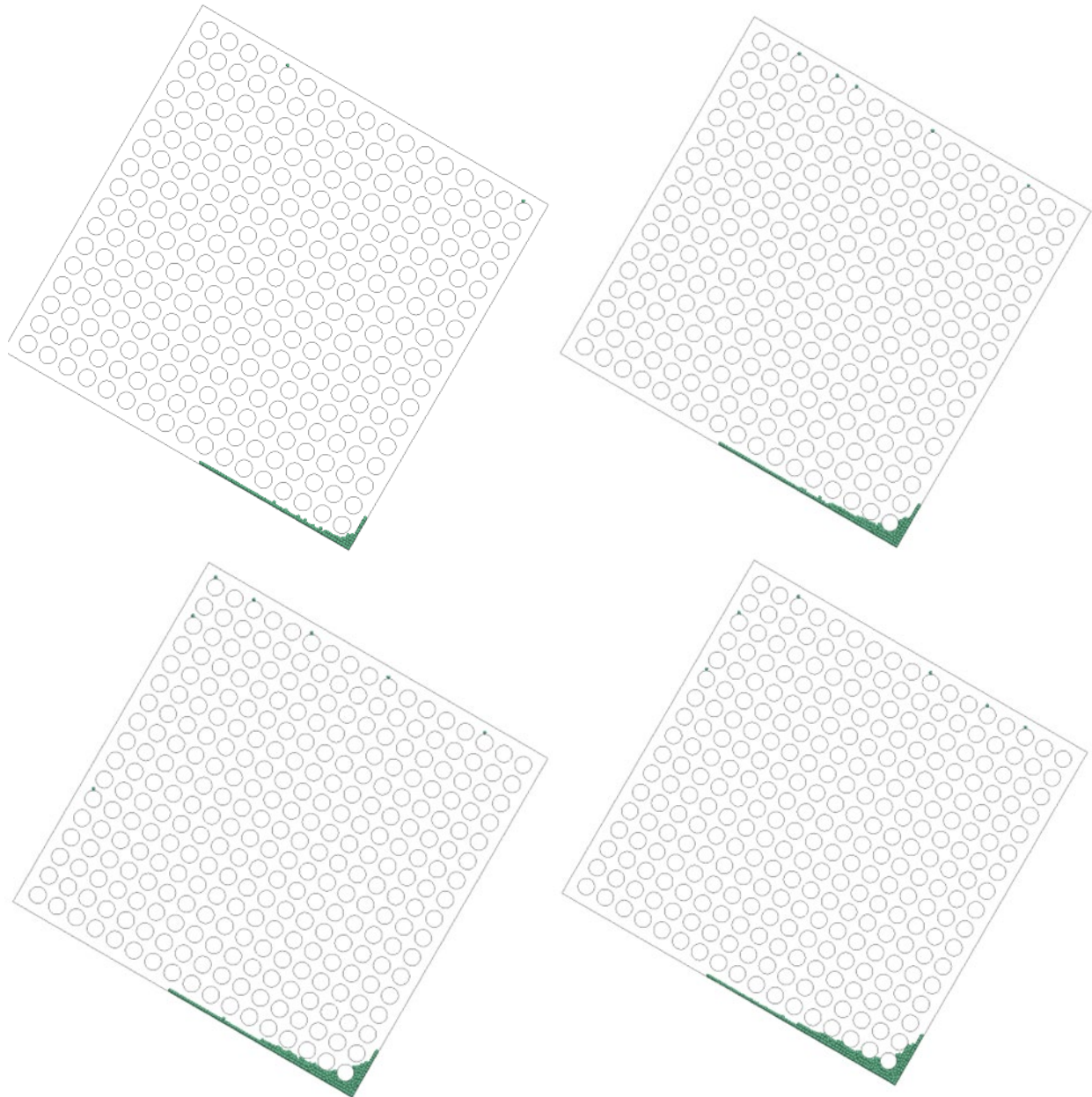


Figure 6. Corrosion products at (top left) X years, (top right) 2X years, (bottom left) 4X years, and (bottom right) 8X years for balls and 30° inclination case.

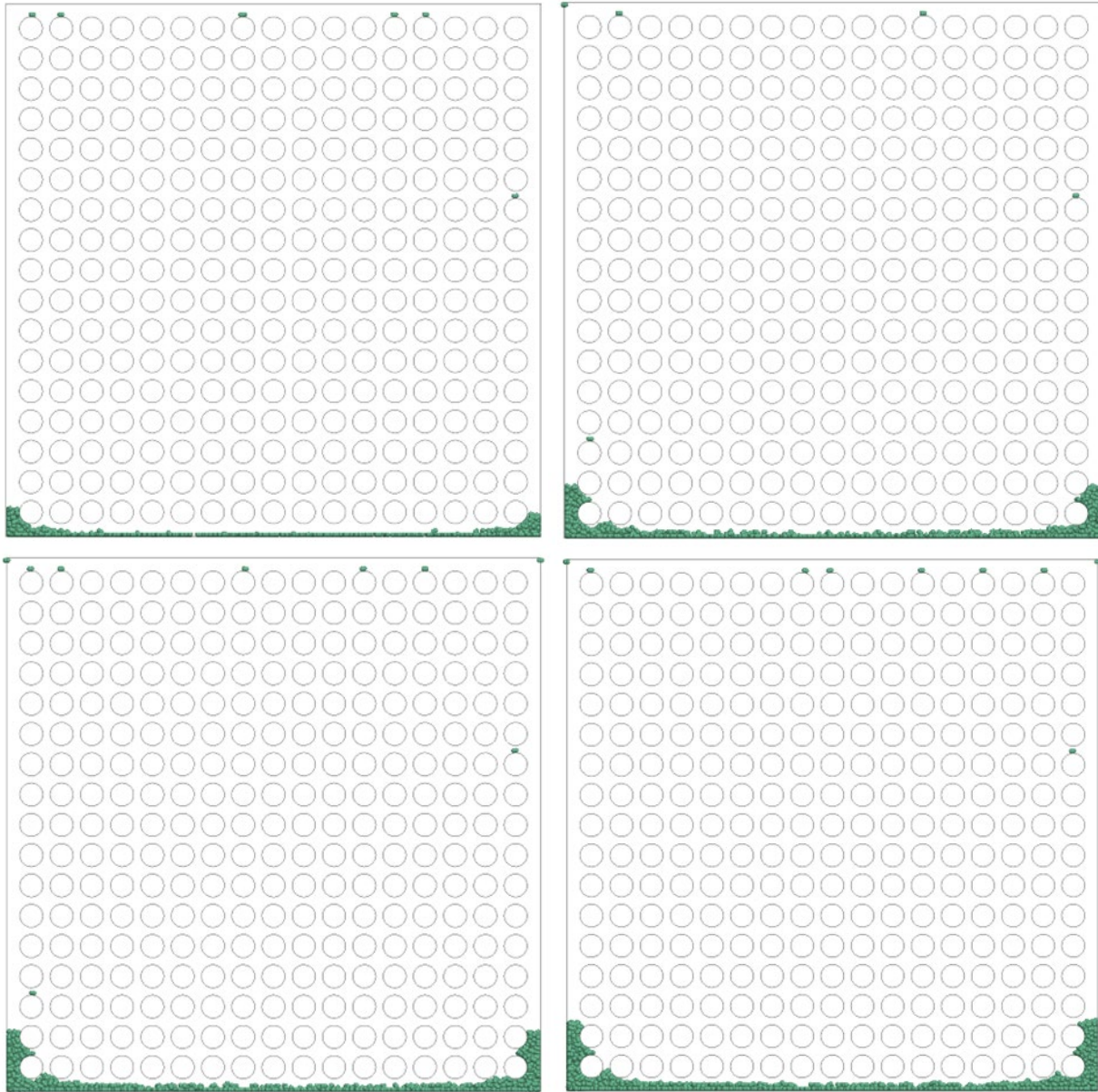


Figure 7. Corrosion products at (top left) X years, (top right) 2X years, (bottom left) 4X years, and (bottom right) 8X years for clumps and 0° inclination case.

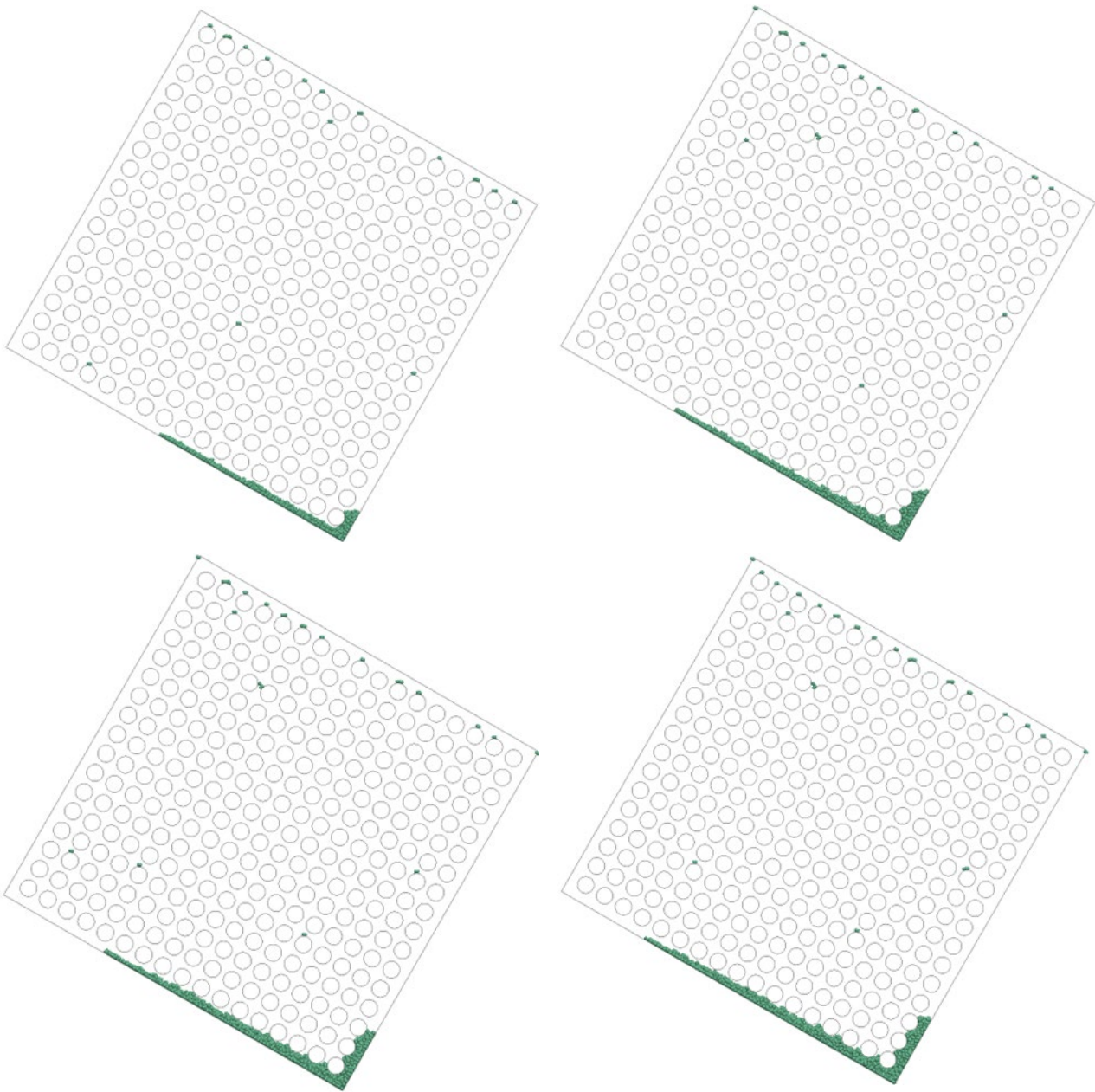


Figure 8. Corrosion products at (top left) X years, (top right) 2X years, (bottom left) 4X years, and (bottom right) 8X years for clumps and 30° inclination case.

#### 4.4 Seismic Analysis

After the specified duration of corrosion was simulated (8X in this case), a seismic analysis was carried out. It was assumed that the canister is embedded in ground (i.e., backfilled) at least partially so that the ground motion is transferred directly to the canister, and that the basket structure is intact so that there is no relative motion between the basket and canister. Relative motion between the basket and fuel rods was also neglected. To model the seismic shaking the vertical component and one horizontal component of ground motion (both normal to the axis of the canister) were applied as velocity components to the basket and fuel rods (Figure 9). The third component (horizontal) cannot be used for this case due to the periodic boundary condition in out-of-plane direction. For this demonstration, a ground motion history from the set for the 1.05 m/sec peak ground velocity (PGV) level used for the Yucca Mountain project was selected. Snapshots of configuration at four different instants of time are shown in Figure 10. As most of the energy in ground shaking is in the first twelve seconds, relatively smaller changes are observed after that. The results indicate that there is redistribution of corrosion products due to shaking, which could be important for initiating a transient criticality, especially if particle release is also accelerated by shaking as discussed below.

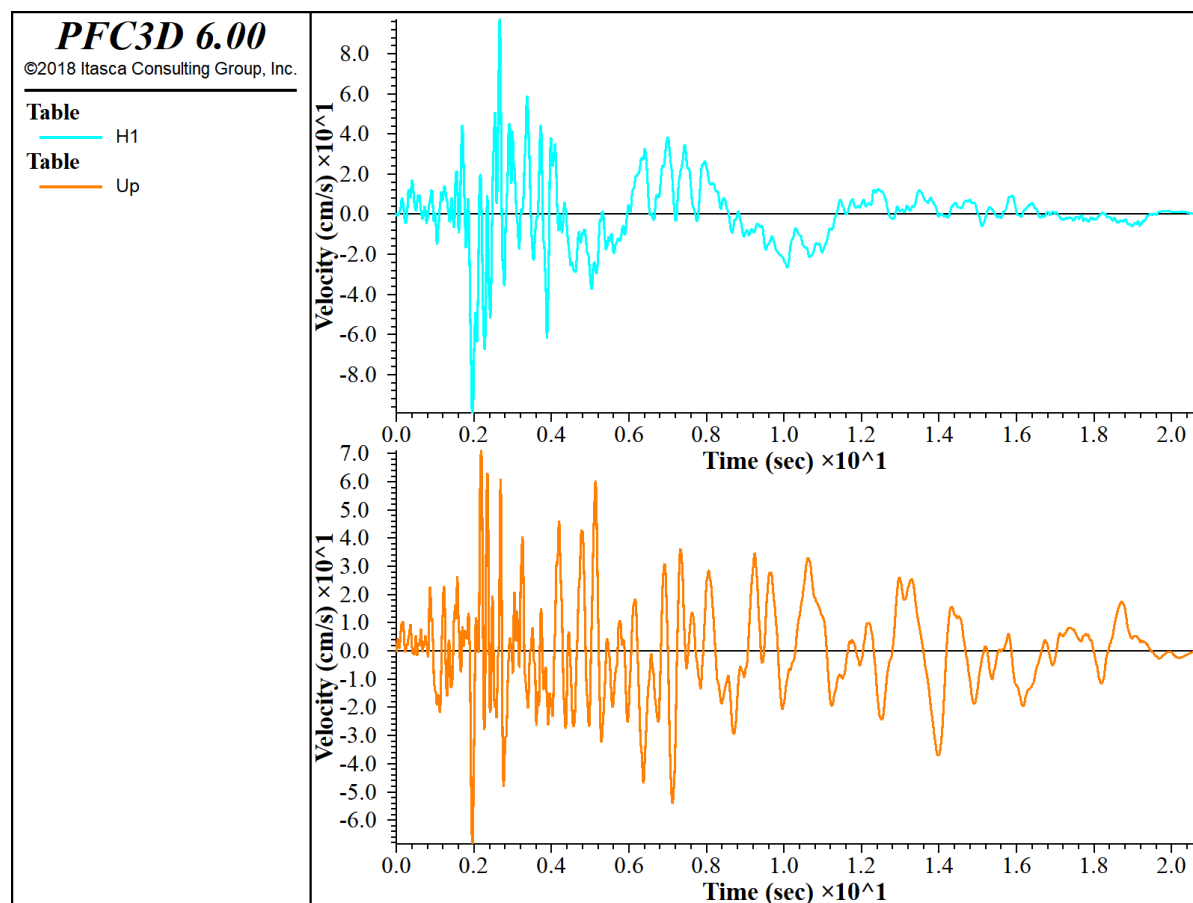


Figure 9. Velocity time histories for horizontal (upper) and vertical (lower) components of ground motion used for shaking the plates.

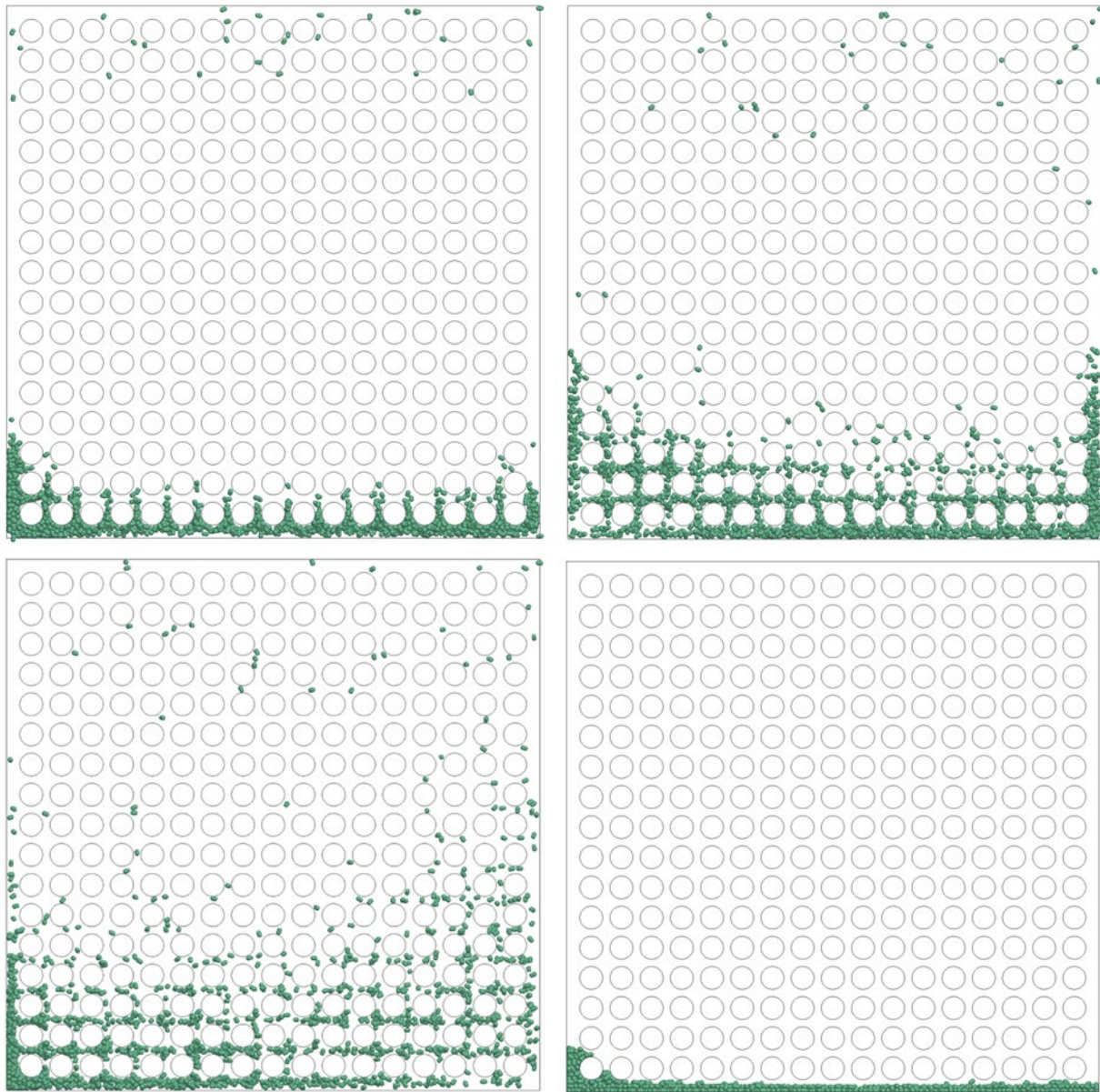


Figure 10. Model configuration at 1 second (top left), 2 seconds (top right), 5 seconds (bottom left), and after the end of shaking (bottom right) for clumps and  $0^\circ$  inclination case.

#### 4.5 Discussion

An important uncertainty in modeling of plate degradation is the criterion for release of corrosion-product particles from the plates. In particular, the extent of release in the event of a seismic event could determine whether a transient criticality event occurs, and the nature of the event. The size

of released particles could be a factor in settling behavior. Anodizing the basket plates creates a thin, compact oxide layer that likely affects particle size and the initial rate of sloughing.

To address these uncertainties, future work should represent the mechanics of detachment and unravelling of corrosion products. Weakening of corrosion product elements prior to detachment, and weakening of the basket plates as they corrode, could improve realism especially when the model is subject to seismic shaking. Spatially heterogeneous degradation properties could also improve realism, e.g., representing weld-affected zones, spatially varying temperature, and partially saturated conditions in the canister.

One possible way to represent detachment and unravelling of the corrosion products is to model the plates as bonded assemblies of balls that represent the aluminum matrix with B<sub>4</sub>C particles inside. As part of the corrosion process, the bonds in this assembly can then be allowed to break randomly near the face, releasing particles (representing the corrosion product). That could more realistically model the corrosion process in terms of size of particle released and timing as a function of location, i.e., particles in the roof may fall at a faster rate than those on the sides and may have a different size distribution as well. It would also explicitly represent thinning of the neutron absorbing plates.

Eventually, based on demonstrated utility of model results, the fuel assembly cell model can be further developed to include: 1) BWR fuel assemblies; and 2) degradation of stainless steel basket plates (or plated carbon steel), with Boral® sandwich-style absorber plates.

## 5. Basket Degradation Model

Azadeh Riahi and Branko Damjanac (Itasca Consulting Group; Section 5.1)  
Varun and Branko Damjanac (Itasca Consulting Group; Section 5.2)

### 5.1 *FLAC3D* Study of Basket Plate Deformations

#### Introduction

This section summarizes an analysis of failure modes of aluminum-based fuel basket plates in a DPC, performed using the *FLAC3D* code (Itasca 2019). The results are used in a separate model (Section 5.2) that simulates complete basket collapse and requires explicit representations of all relevant structural components.

There are several potential mechanisms that can lead to DPC basket structure failure due to corrosion and thinning of structural components:

- Plastic failure of the horizontal basket plates as a result of bending, shearing, or a combination of both,
- Buckling of the vertical basket plates, and
- Failure of welded joints.

Analysis of these mechanisms in a canister-scale model could be computationally prohibitive because of the meshing requirements to capture each mechanism accurately. Therefore, an incremental approach is adopted whereby smaller models at different scales are built to analyze each mechanism with the required mesh discretization. These models include:

- *FLAC3D* model of an individual basket cell to evaluate plastic failure of horizontal plates,
- *FLAC3D* model of a full basket for evaluating kinematic instability (buckling) of the vertical basket plates, and
- *FLAC3D* model of an individual basket cell for analysis of local buckling within a cell.

#### Model Geometry

The geometry for the basket approximates the Holtec MPC-32® basket design (Figure 11). The width and height of each cell are assumed to be 0.21 m. Dimensions are adjusted to approximate the inner diameter of the canister, the number of cells, and the geometry of the basket.

The geometries of the fuel assembly and rods are shown in Figure 12. Assuming PWR fuel, a 17×17 array configuration with 25 guide/instrument tubes is represented. The inner and outer diameters of the cladding are taken from the description of Buongiorno (2010, p. 12). The fuel type is assumed to be UO<sub>2</sub>, and the cladding is assumed to be Zircaloy (see Section 5.2 for properties of the fuel).

The *FLAC3D* models assume symmetry along the canister axis. The *FLAC3D* basket and single-cell models each represent a section from the middle of the spacer grid to the half-distance of two spacer grids (Figure 13).

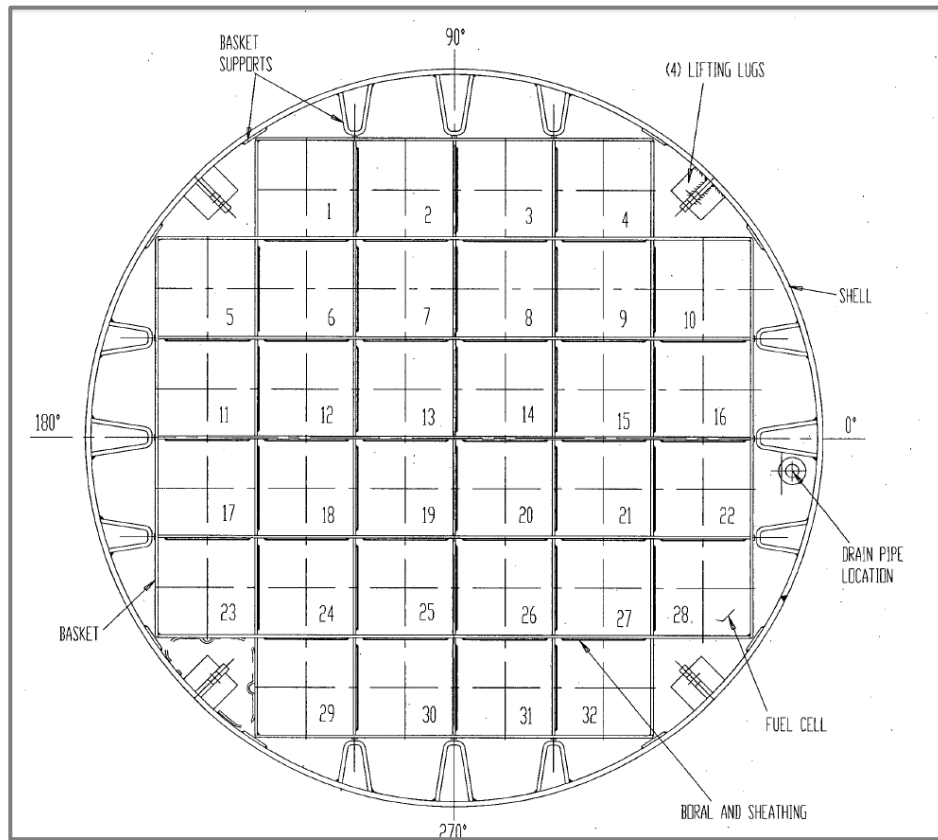


Figure 11. Cross-section view of fuel basket (from Figure 1.2.4 in Holtec 2018).

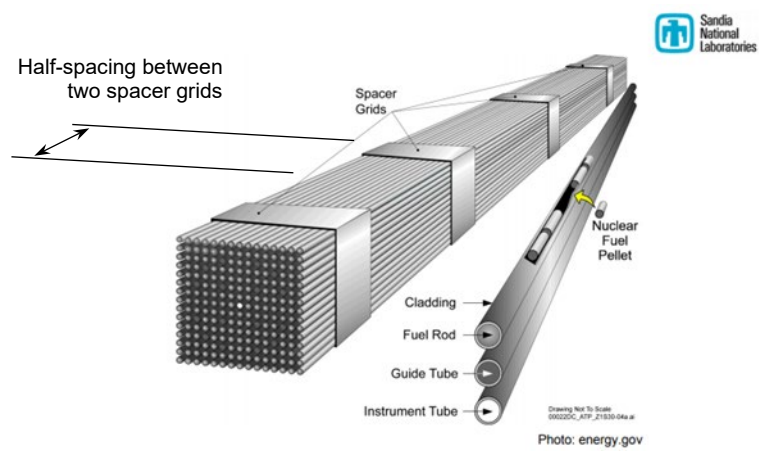


Figure 12. Geometry of the fuel assembly.

### Fuel Assembly Loading

The total load of the fuel assembly is transferred to the horizontal plates at the interface between the plates and the spacer grids. The load carried by each spacer grid is calculated using the geometry shown in Figure 13. It is assumed that the spacer grid width is 5 cm and the center-to-center spacing between the grids is 0.6 m. The fuel assembly characteristics are selected considering tables provided by Holtec (2018). The reference table for a 17×17 array configuration is presented in Appendix A.

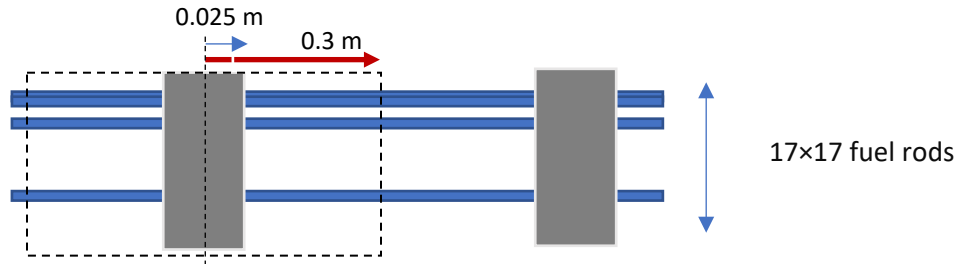


Figure 13. *FLAC3D* model representation along the canister axis. The black dotted box shows the load of fuel assembly and spacer grid transferred to the horizontal plate at the interface between each spacer grid and horizontal plate. Only half the spacing between spacer grids is represented in the *FLAC3D* model, as shown.

### Material Properties

It is assumed that the fuel basket plates are made from MMC material (e.g., Metamic-HT®) with properties similar to aluminum. Values for the Young’s modulus, Poisson ratio and density of Metamic-HT (Blue 2009) are shown in Table 2. Blue (2009) specified a minimum tensile strength of 31.3 ksi (216 MPa) for Metamic-HT plates. In this study, to be conservative, a tensile yield strength of 200 MPa was selected for basket plates. In these calculations, for Zircaloy and UO<sub>2</sub>, only the density values are relevant (used to calculate the total weight of the fuel assembly discussed in the previous section).

Table 2. Fuel properties for basket component deformation scoping calculations.

Material	Young’s Modulus (GPa)	Poisson Ratio	Density (kg/m <sup>3</sup> )
Zircaloy			6,500
Aluminum/Metamic-HT	80	0.3	2,690
UO <sub>2</sub>			10,970

### Results for Shear and Bending Failure of Horizontal Plates

The objective of the analysis documented in this section is to estimate the plate thickness that would result in plastic failure due to shearing or bending of horizontal plates. For such an analysis, building the model of the entire fuel basket is not necessary. A *FLAC3D* model was developed to

represent a single cell with a third dimension equal to half the spacing between spacer grids (Figures 12 and 13). This allows the creation of a model with very fine discretization (scale of millimeters) which is needed to capture bending and shearing mechanisms through the thickness of the plate. Instead of modeling the thinning process of the plates progressively, models with different plate thicknesses representing different states of corrosion are modeled independently. For each model, the plate is discretized into four zones along the thickness.

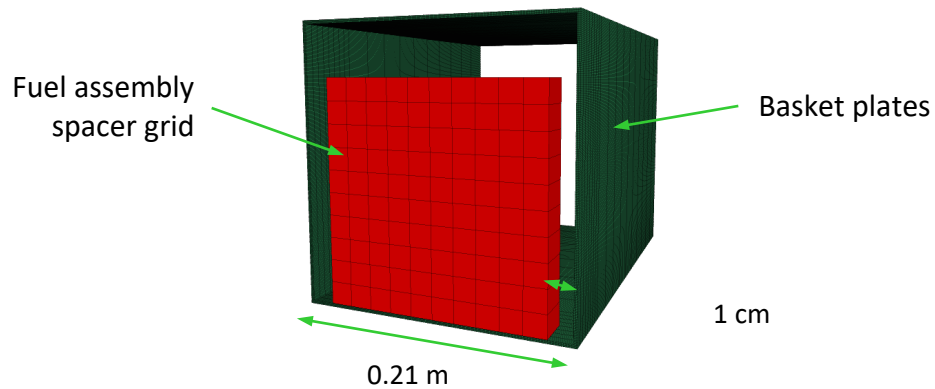


Figure 14. Single-cell model (of the basket shown in Figure 11) with spacer grid represented as an equivalent rigid material.

Note that in order to verify the results of the numerical model, a simple analysis using beam theory is also carried out below to calculate approximate sectional forces and stresses.

### Numerical Modeling

The basket plates are represented with the elastic-perfectly plastic von Mises constitutive model, and a lower bound strength value of 200 MPa. It is assumed that corrosion of the spacer grids is slow and negligible compared to corrosion of the plates, so it is represented as an equivalent elastic material with much greater stiffness (100×) than the plates. To represent the flexural rigidity of the system correctly, the interface between the spacer grids and the horizontal plates is represented using interface elements in *FLAC3D*. The density (specific weight) of the spacer grid is selected such that it results in loading on the plate equivalent to the load by the weight of the spacer grid and the partial weight of the fuel carried by each spacer grid. The model is quasi-static, and the lower corners of the cell are fixed (Figures 16 and 17). Finally, it is assumed that the basket is in submerged condition (i.e., the canister is filled with water). The density of water at 200°C is subtracted from all densities.

A series of single-cell models with different plate thickness values ranging from 1 cm to 1 mm is presented. The *FLAC3D* analyses shows that for the assumed plate thickness values and plate properties (close to aluminum) no plastic failure within the horizontal plates occurs for the models with plate thickness of 1.0 mm or more. Contours of displacement for a cell model with plate thickness of 2 mm are shown in Figure 15. For visualization purposes the deformation is magnified 100 times. This plot shows clearly that the cell model overestimates displacement of vertical plates by disregarding the effects of adjacent cells. Also, it shows that the vertical and horizontal

displacements remain very small. Therefore, the potential for closure of the gap between spacer grids and basket plates is negligible for the assumed plate thickness values of 1.5 mm or more.

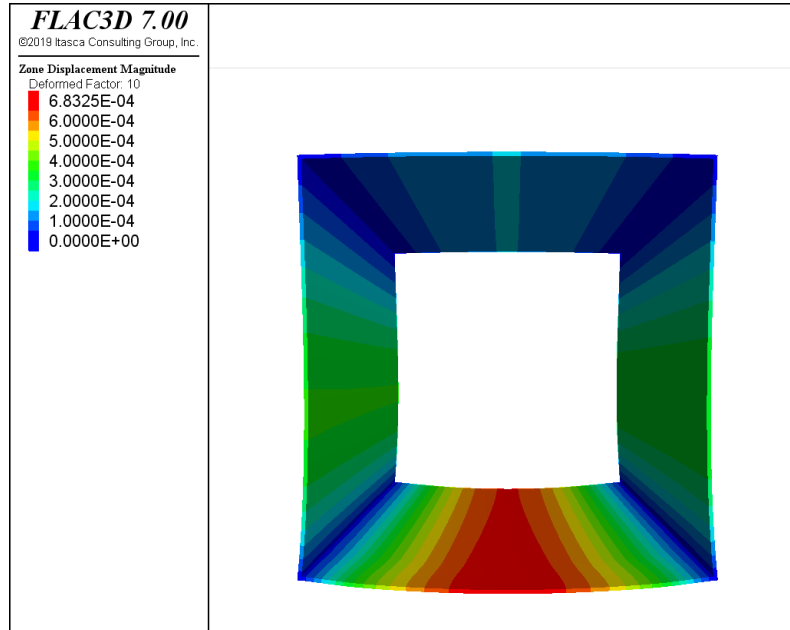


Figure 15. Displacement contours (m) within the basket cell for a plate thickness of 2 mm (displacements magnified 100×).

Contours of total displacement for the single-cell models with plate thickness of 1 mm are shown in Figure 16. For plate thickness of about 1mm, the maximum displacements are approximately 0.5 mm. No plastic failure is observed within the horizontal aluminum plates. Figure 17 shows contours of  $\sigma_{xx}$  in the cell model, which roughly represents the normal stresses caused by bending within the plate.

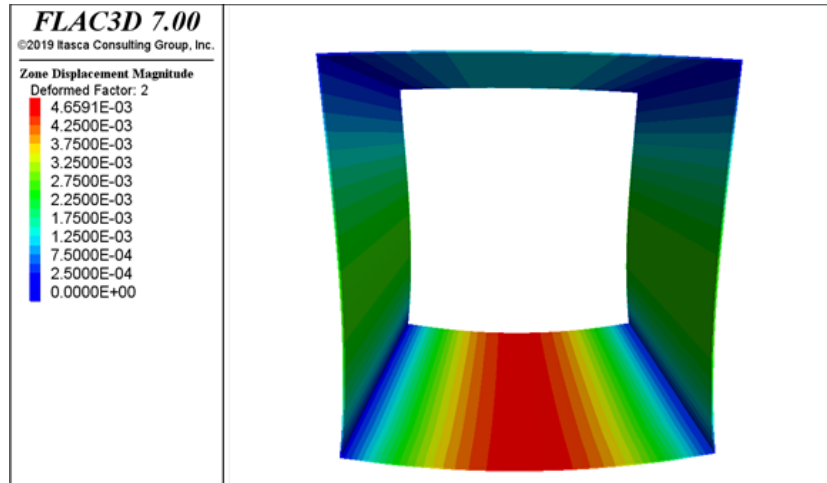


Figure 16. Displacement contours (m) within the basket cell for a plate thickness of 1 mm (displacements magnified 100×).

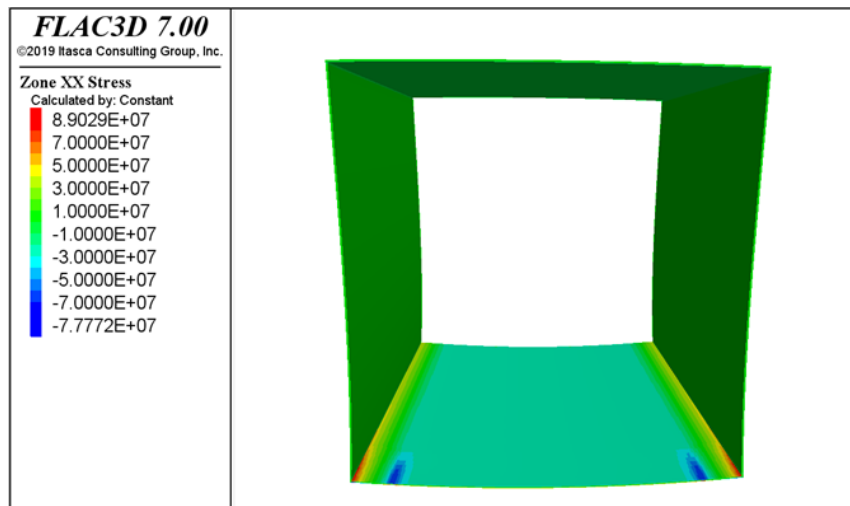


Figure 17. Contours of  $\sigma_{xx}$  (Pa) within the basket cell for a plate thickness of 1 mm (displacements magnified 100×).

### Calculations Based on Beam Theory

To evaluate these results two limiting cases are considered. First, it is assumed that each plate behaves as a simply supported beam, and second, it is assumed that the plate behaves as a beam fixed at both ends. From the contours of deformation and stress shown in Figures 16 and 17, respectively, the width of the beam engaged in bending response is assumed to be equal to half the spacing between the two spacer grids (because the load by the spacer grids is not continuous along the horizontal plates). However, for calculation of shear stresses, it is assumed that most of the load is carried by the area below the spacer grid. Therefore, for calculation of shear stresses, the width of the beam is assumed to be equal to the width of the spacer grid. Assuming a free-rotational boundary condition (simply supported beam) should be conservative, and the true condition representing welded vertical and horizontal plates in the basket is between a completely free and a rigidly fixed rotational boundary condition.

The maximum moment in a simply supported beam is  $WL^2/8$ , and in a beam fixed at two ends it is  $WL^2/12$ . In both cases, the maximum shear force is  $WL/2$ , where  $W$  is the distributed load per unit length of the beam and  $L$  is the beam span. The maximum bending stress in the beam is  $\sigma = Mc/I$ , where  $I$  is the moment of inertia of the beam cross-section and  $c$  is the distance from the neutral axis to the outermost point of the cross-section. For a rectangular cross-section with a width of  $b$  and a thickness (height) of  $h$ ,  $I$  is equal to  $bh^3/12$ .

Using a distributed stress of  $1.35 \times 10^5$  Pa (weight of the fuel), a spacer grid width of 0.05 m, and a beam span of 0.21 m, Table 3 presents the axial and shear stresses for the assumed conditions. Comparing values of axial stress to the assumed tensile strength for plates, suggests that for plate thickness of 1.5 mm or more the potential for plastic failure due to bending is negligible. Also, the potential for failure due to shearing of aluminum plates is significantly less than failure due to bending.

Compared to the *FLAC3D* models, the cases presented in Table 3 underestimate the stiffness of the structure by disregarding the contribution from other components of the cell.

Table 3. Analytical calculation for maximum axial and shear forces in a basket plate.

Plate Thickness (m)	$I$ (m <sup>4</sup> )	$EI$ (Pa·m <sup>4</sup> )	Maximum Moment, SS (N·m)	Maximum Moment, fixed (N·m)	Maximum Bending Stress, SS (Pa)	Maximum Bending Stress, fixed (Pa)	Shear Stress (Pa)
0.01	$5 \times 10^{-8}$	$4.00 \times 10^3$	$3.72 \times 10^1$	$2.48 \times 10^1$	$3.72 \times 10^6$	$2.48 \times 10^6$	$1.42 \times 10^6$
0.005	$6.25 \times 10^{-9}$	$5.00 \times 10^2$	$3.72 \times 10^1$	$2.48 \times 10^1$	$1.49 \times 10^7$	$9.92 \times 10^6$	$2.84 \times 10^6$
0.0025	$7.81 \times 10^{-10}$	$6.25 \times 10^1$	$3.72 \times 10^1$	$2.48 \times 10^1$	$5.95 \times 10^7$	$3.97 \times 10^7$	$5.67 \times 10^6$
0.002	$4 \times 10^{-10}$	$3.20 \times 10^1$	$3.72 \times 10^1$	$2.48 \times 10^1$	$9.30 \times 10^7$	$6.20 \times 10^7$	$7.09 \times 10^6$
0.0015	$1.69 \times 10^{-10}$	$1.35 \times 10^1$	$3.72 \times 10^1$	$2.48 \times 10^1$	$1.65 \times 10^8$	$1.10 \times 10^8$	$9.45 \times 10^6$
0.001	$5 \times 10^{-11}$	$4.00 \times 10^0$	$3.72 \times 10^1$	$2.48 \times 10^1$	$3.72 \times 10^8$	$2.48 \times 10^8$	$1.42 \times 10^7$

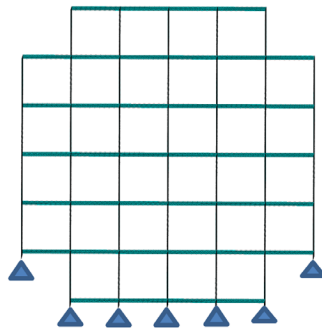
\* SS refers to simply supported

### Analysis of Entire Basket Collapse Due to Buckling

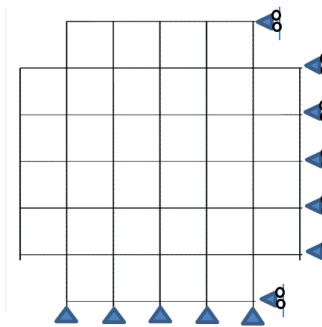
The objective of these analyses was to evaluate the failure conditions of the vertical plates of the basket. Failure of thin plates subjected to axial load often involves buckling. In these studies, the

critical plate thickness that would lead to buckling of the basket was evaluated. Similar to the approach taken in the previous subsection, instead of modeling the thinning process progressively, *FLAC3D* models of the fuel basket were constructed assuming different plate thickness values. Two different boundary condition scenarios were considered. In the first set of analyses, it was assumed that there is a gap between the fuel basket and the horizontal support elements (see Figure 11). This gap represents an initial small spacing between the basket and support elements that is required for placing the basket within the canister. The gap also reflects increased spacing due to corrosion of the plates. In the second set of analyses, the basket is constrained horizontally at the lateral support locations shown in Figure 11.

It is assumed that the basket is not in contact with any of the vertical supports at the top, and thus can freely move in the vertical direction. The support elements are modeled using short plates that are rigidly attached to the basket. The translational displacements of the bottom supports are constrained. The assumed boundary conditions for both sets of analyses are shown in Figure 18. The effect of boundary conditions on the critical buckling load and deformation mode has been studied using analytical solutions. The Euler's critical buckling load and mode for beams subjected to different boundary conditions are presented in Appendix B.



Model A: DPC basket with free lateral movement.



Model B: DPC basket with fixed lateral movement.

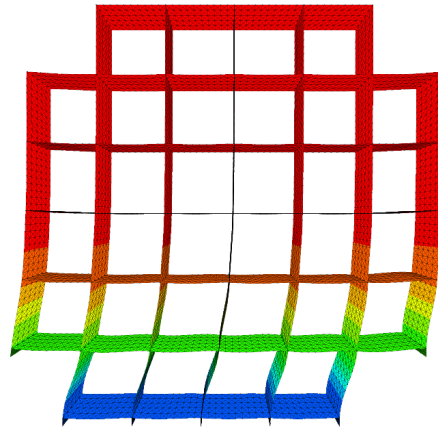
Figure 18. Geometry and boundary conditions of the full basket model.

The buckling mode and approximate critical plate thicknesses associated with the onset of kinematic instability are presented in Figure 19. The thickness of plates is varied in intervals of

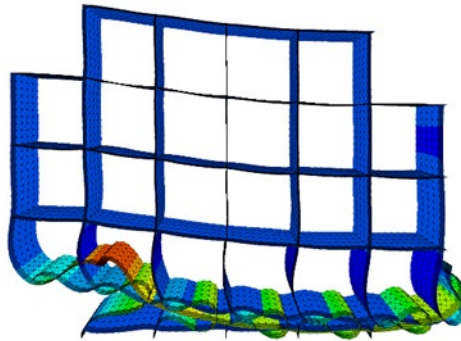
0.5 mm. These results show some analogy to the buckling mode for beams subjected to different boundary conditions and can be summarized as follows.

- If there is a gap between the basket and the horizontal supports, the basket will undergo global buckling when the plate thickness reaches a value of approximately 2 to 2.5 mm. The buckling mode is similar to the buckling of a cantilever column that is fixed at one end and free at the other.
- Upon buckling of the bottom rows of the vertical plates, the basket will move laterally as shown in Figure 19(a) and will contact the lateral supports, which will prevent continuous instability of the basket. The boundary conditions now become similar to those shown in Figure 18(b).
- Independent analyses of basket models with constrained horizontal displacement, as shown in Figure 18(b), suggest that buckling occurs in the bottom two rows of the cells. The buckling mode for the assumed boundary conditions is shown in Figure 19(b). The displacements shown in Figure 19(b) are not realistic because the presence of a spacer grid is not accounted for.
- The critical plate thickness for buckling instability for models with constrained horizontal displacement is between 1 and 1.5 mm. Analysis of the *FLAC3D* models with assumed properties suggests that the critical thickness is very close to 1.5 mm.

The displacement modes for models with constrained lateral boundaries prior to total collapse (Model B) are shown in Figure 20(b), which shows a series of instabilities within multiple cells. The effect of the spacer grid was modeled through an additional study in which the horizontal movement of plates was constrained once the displacement in the horizontal direction reached 1 cm. This value represents the assumed gap between the spacer grid and the plates. Figure 21 shows regions where the vertical plates contact the spacer grid. Additional studies show that constraining the lateral movement of these regions prevents additional buckling. Figure 22 shows deformation of a basket model with similar plate thickness to the model that had experienced buckling. The difference between the two models is the constraint of lateral movement by spacer grids.

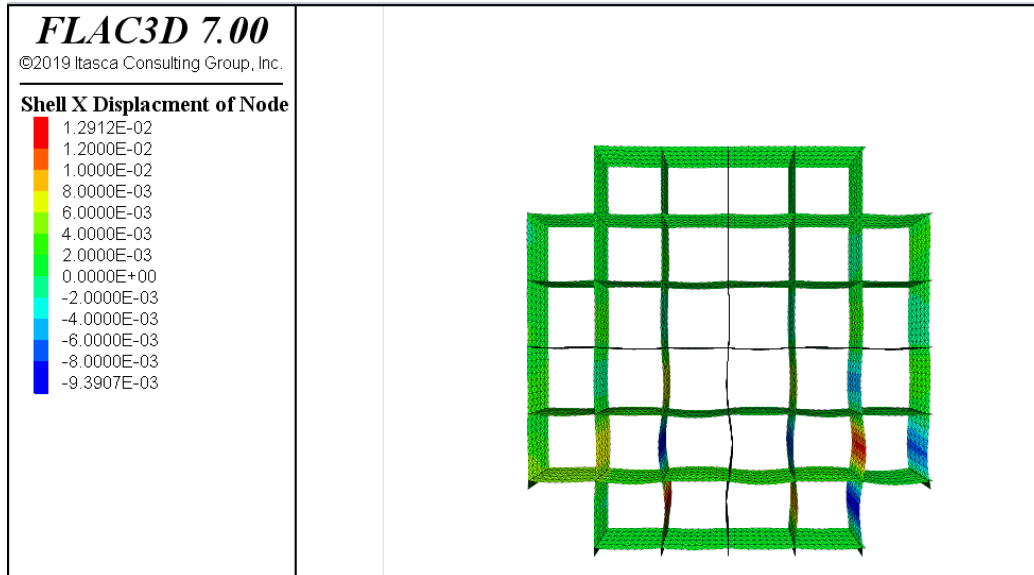


Model A with  $2 < t < 2.5$  mm

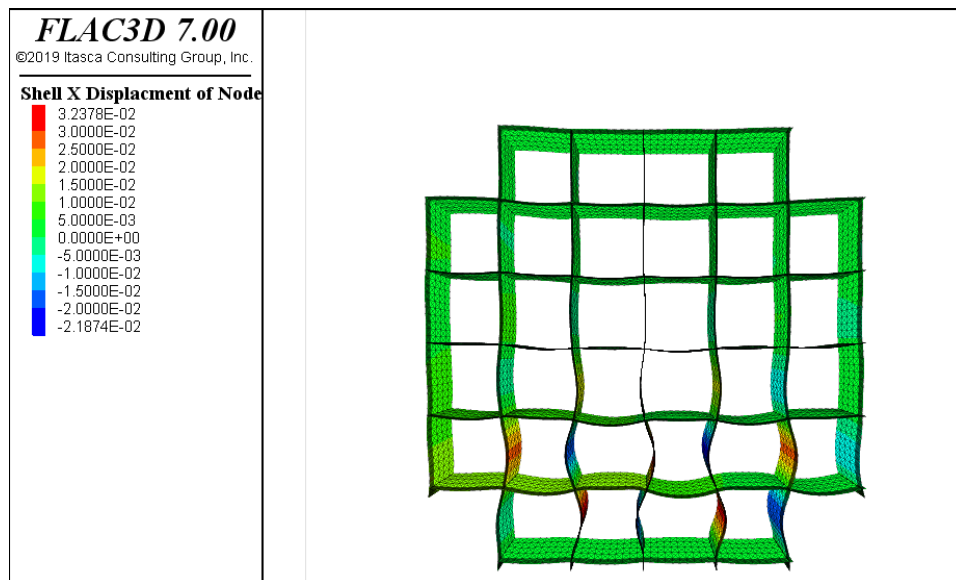


Model B with  $1.5 < t < 2$  mm

Figure 19. Buckling mode and critical thickness for onset of buckling for basket models. Colors represent the relative value of horizontal displacement, with blue being close to zero and red representing the maximum.



(a) At the onset of buckling.



(b) A state during buckling.

Figure 20. Deformation of Model B prior to the state shown in Figure 19 (Model B).

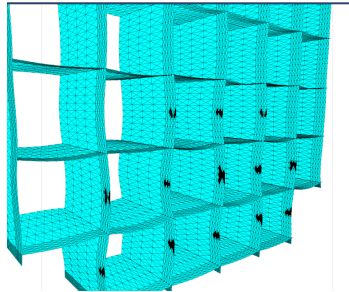


Figure 21. Basket model with spacer grid implementation (black color shows regions constrained by spacer grid).

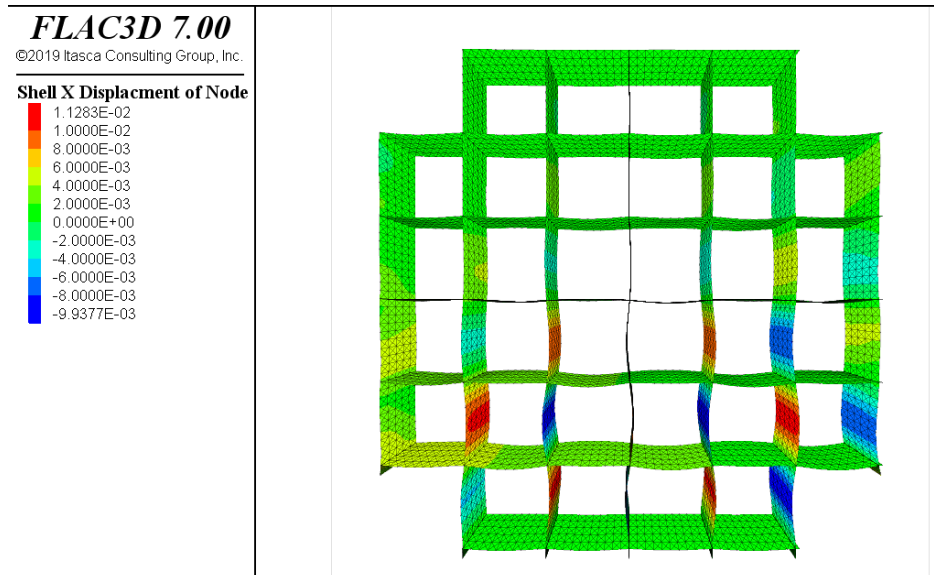


Figure 22. Deformation contours of basket Model B with implementation of a lateral constraint due to presence of spacer grids.

### Analysis of Buckling of Individual Cells

Previous analyses suggest that when the horizontal movement of the basket is constrained by basket support (Figure 11) the free length (equivalent column buckling length) reduces significantly, and kinematic instability of the basket is preceded by a series of buckling instabilities within cells. In order to get a more accurate estimate of buckling load and to evaluate if there are potential local instabilities within a cell that might have been missed due to the discretization of the full basket model, a single-cell model with much finer discretization was analyzed. The geometry and boundary conditions for a single-cell model are shown in Figure 23.

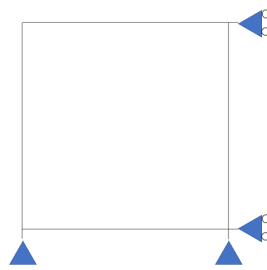


Figure 23. Geometry and boundary condition for a single-cell model.

Analyses of a single-cell model were carried out up to a plate thickness of 0.8 mm. These results suggest that while the cell model with a thickness of 1 mm shows clear geometric nonlinearity, it remains stable. The cell model with a thickness of 0.8 mm shows complete buckling instability. As a result, it can be concluded that: 1) no buckling mechanism should precede the mode observed above for the entire basket; and 2) the lateral constraint in the cell model reduces the buckling free length and thus, the critical load decreases. The *FLAC3D* single-cell geometry and buckling model are shown in Figure 24.

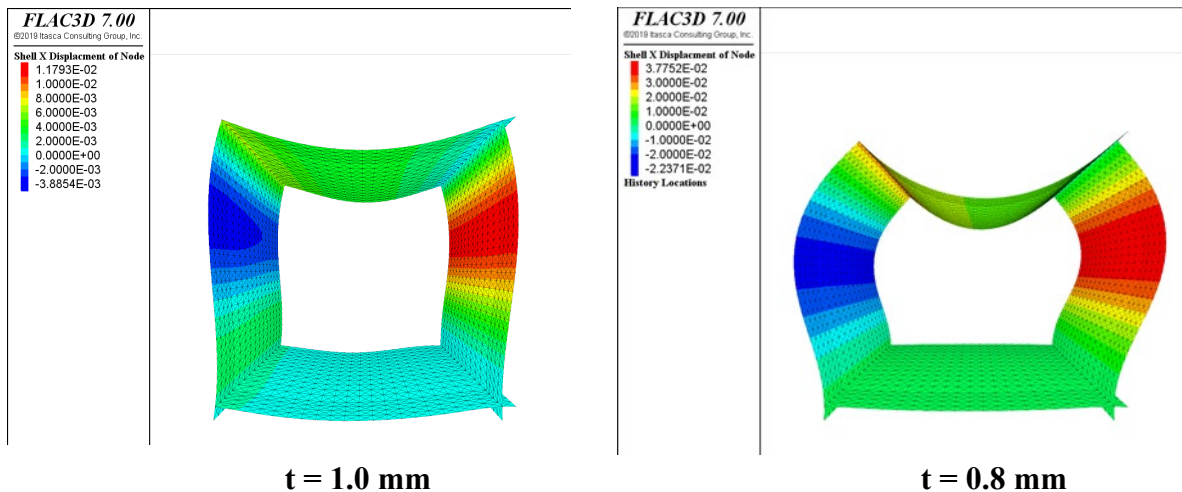


Figure 24. Displacement contours (m) from *FLAC3D* buckling analysis of a single-cell model, for plate thickness of 1.0 mm (left); and plate thickness of 0.8 mm (right). The displacements for the model with thickness of 0.8 mm are not final displacements because the model is unstable.

## Discussion and Conclusions

Structural collapse of the fuel basket can involve different mechanisms of failure. In this study, models accurate at different scales were created to investigate the onset of instability and collapse

within the basket. These studies suggest that shearing and bending of horizontal plates become a relevant failure mechanism when the plate thickness is less than 1 mm. However, buckling failure of the canister can occur for plate thickness values of approximately 2 mm to 2.5 mm if a gap exists between horizontal supports and the canister. If the canister is constrained laterally by the horizontal supports, then the basket will maintain its integrity with plate thickness from 1 to 1.5 mm. At these thickness values the vertical walls of the two lower levels of cells will buckle. As a result of large displacements, the cell walls will come in contact with the spacer grids. Spacer grids can provide horizontal support and constrain buckling within a specific cell; however, the columns can no longer hold axial loads. As a result, it is expected that the effective span of horizontal plates increases. Overall, these studies suggest that fuel basket collapse due to corrosion of the plates will occur as a result of vertical plate buckling when their effective thickness reduces to 1 to 2 mm from corrosion. Interaction of buckling with plate bending and shearing was not investigated in these studies.

## **5.2 Distinct Element Model of Basket Collapse**

This section summarizes the analysis of evolution of fuel basket collapse in a DPC using the *3DEC* code (Itasca 2016). For study of the incidence and consequences of criticality, it is important to understand the evolution of DPC internal degradation including plates, grid spacers, and fuel rods. The purpose of the basket collapse model is to simulate rearrangement of basket structural elements and fuel, falling under gravity (or seismic motion) within the canister as a result of degradation caused by corrosion. The model is developed for a configuration that approximates a representative MPC-32® fuel basket, using insights regarding structural failure and disaggregation of basket plates gained from the *FLAC3D* models described in Section 5.1.

### **Detailed Basket Model**

*3DEC* software implementing the distinct element method (Itasca 2016) is used to simulate the collapse of basket elements. The models are templated such that the user can specify the geometry and material parameters, and then *FISH* routines (a scripting language native to Itasca codes) are used to set up and run the model. The model is set up using different modules for each component so that the level of detail for any component can be changed without affecting the rest of the model. The three modules are for fuel assemblies, basket plates, and the canister shell. As described below, two types of models have been set up, with the difference being the level of detail to which the components have been modeled.

The detailed model simulates all components of the DPC including fuel assemblies, with reasonable detail. Fuel rods, guide tubes, spacer grids, end nozzles, basket plates, and the canister shell are all modeled individually using coarsely discretized blocks as discussed below. The 3-D model is set up as shown in Figure 25 to Figure 27, and the entire length and volume of the canister are modeled. To reduce computation time a representative length equal to the spacing between two consecutive spacer grids can also be modeled if the spacer grids are not expected to deteriorate. Otherwise, modeling the entire length is required. Due to the level of detail (i.e., explicit representation of each fuel rod) this model is suitable to be used as a validation model for static analysis (run time up to 10 days on a typical desktop workstation), but the run times for seismic analyses are prohibitive (months). As described in later sections, a simplified model (justified by the detailed model) can be used for extensive static parametric studies and for dynamic analyses.

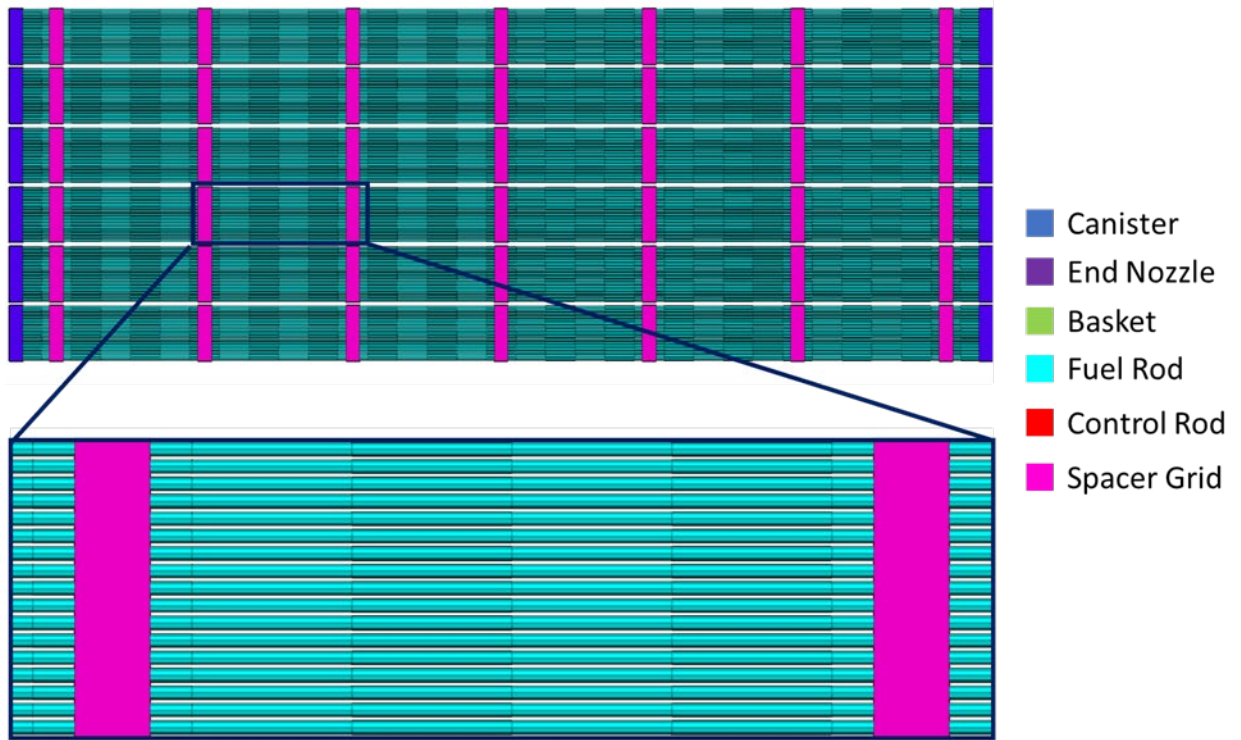


Figure 25. Model setup showing different components in longitudinal view.

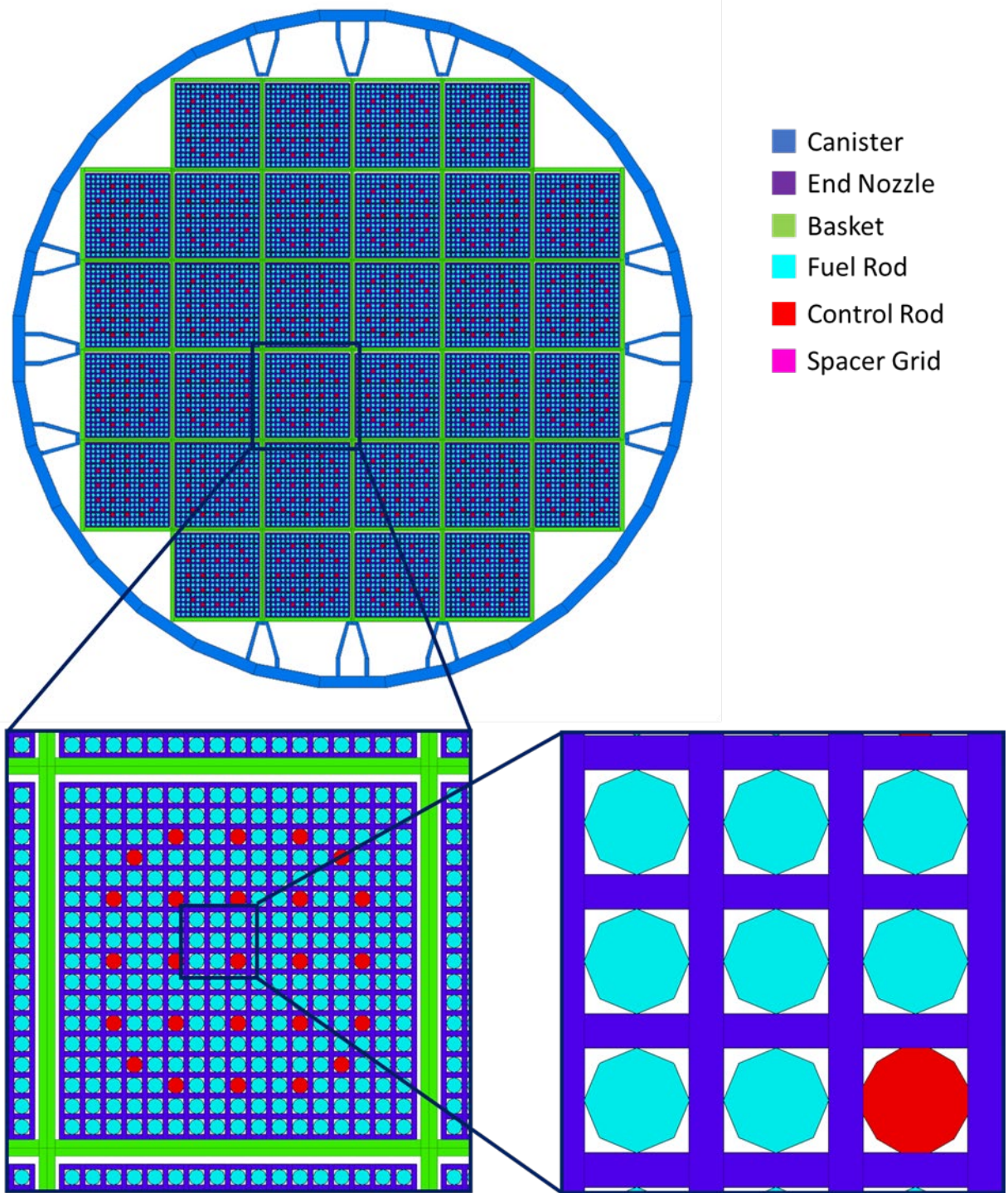


Figure 26. Model setup showing different components in transverse view.

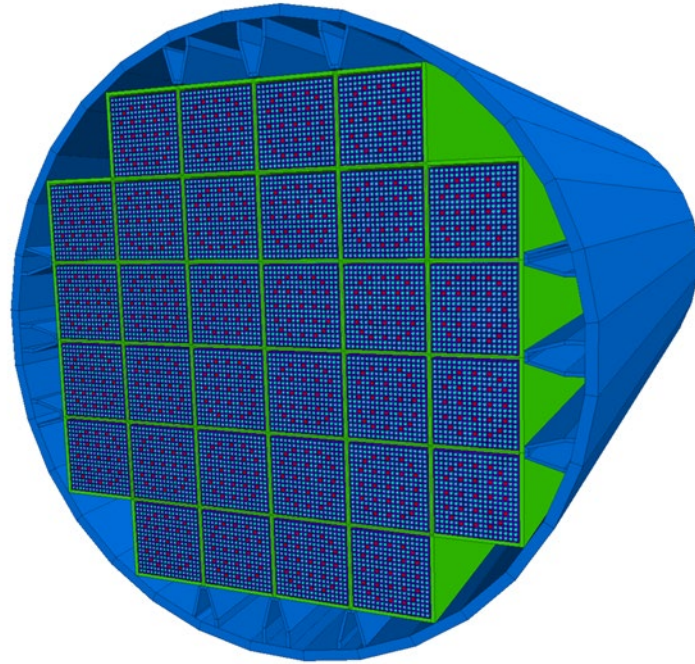


Figure 27. Model setup showing different components in perspective view.

The following subsections described the salient features and assumptions of the model.

### Fuel Assemblies

The fuel assemblies consist of fuel rods, control rod guide tubes, spacer grids, and end nozzles, all of which are simulated separately. A typical fuel assembly used for developing the template is shown in Figure 28. The mixing spacers are equivalent to the spacer grids discussed here.

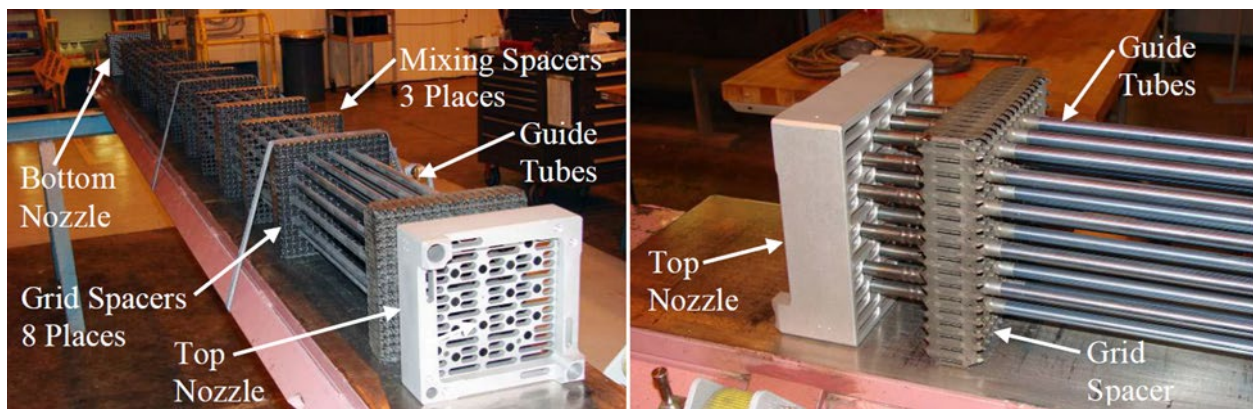


Figure 28. Components of a typical 17×17 PWR fuel assembly (Lindgren and Durbin 2013).

### ***Fuel Rods***

The fuel rods are modeled as long, thin cylindrical blocks. The circular cross-section is approximated as a regular polygon with a user-specified number of sides (Figure 26). A larger number of segments results in better approximation but more computational effort. Between eight and 12 sides to the polygon allow for sufficient detail while keeping run times reasonable. The deformability and flexural strength of rods are modeled by discretizing each rod into a certain number of segments along its length. Each segment is rigid, but the contacts between segments have stiffness and strength that are calibrated to match the analytical response or composite bending behavior observed in laboratory tests. Again, a higher number of segments provides higher resolution but at increased computational cost. Around 5 segments between adjacent spacer grids (about 50 cm) provides enough resolution to produce the simulations presented here.

### ***Guide Tubes and Instrumentation Tubes***

Some of the positions in the array of fuel rods are occupied by guide tubes, and the center position by the instrumentation tube. These tubes are modeled the same way as fuel rods except with different stiffness and strength properties to represent hollow tubes. The user can specify the locations for these tubes in terms of indices from the center, e.g., (0,0) means center tube and (3,6) means it is the third tube from center along one axis and the sixth from center along the other.

### ***Spacer Grids***

The actual structure of spacer grids is very detailed, including thin plates, dimples and springs to hold the fuel rods (Figure 29). Representation of complete details would be computationally prohibitive. Instead, the spacer grid is currently modeled as a rectilinear array of plates (Figure 26). The thickness of plates modeled is larger than the actual thickness such that the boundary condition that the rods have no free room available to move in direction normal to their axis is simulated correctly. However, the density of the plates is reduced accordingly to match the mass of the spacer grid.

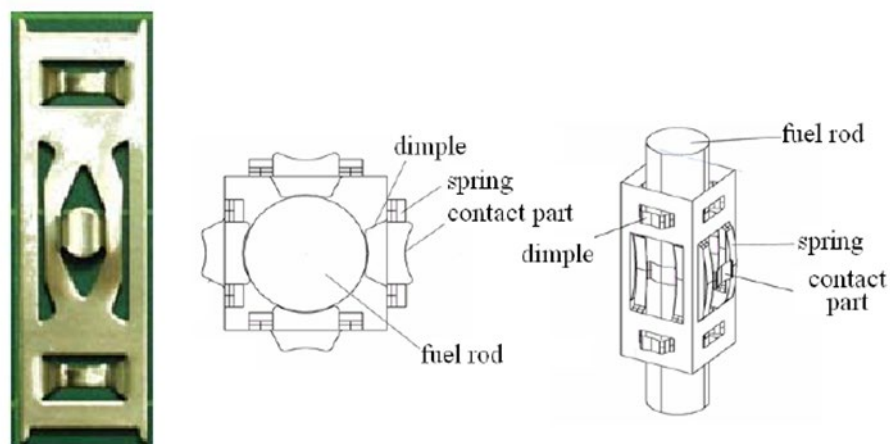


Figure 29. Details of a single cell of spacer grid (Lee et al. 2007).

### ***End Nozzles***

The end nozzles are massive blocks of stainless steel on both ends of the fuel assembly. They are also modeled as rectangular arrays of plates with thicknesses such that the rods cannot move normal to their axis.

### ***Basket Plates***

There are two main types of baskets: egg-crate and tube-and-plate. The egg-crate design is simpler. It consists of parallel, longitudinal plates that extend the full length of the basket. They are indexed together to form a rectilinear array. Each square cell in the array accommodates one fuel assembly. The egg-crate design was the focus of this study as discussed previously. Plates made from Metamic-HT® MMC are modeled using rigid blocks joined at the contacts where actual plates are welded together. If needed, the plates can be discretized along both the length and width to simulate deformability and strength. The plates can also be discretized by multiple blocks along the thickness, and some discrete blocks can be deleted progressively to model the reduction in strength and stiffness due to corrosion.

### ***Canister Shell***

The canister shell is currently modeled as a hollow cylinder with a certain thickness. The side supports inside the cylinder are also modeled. The location and details of the side supports are crucial because they have a significant influence on how the fuel assemblies stack up if the basket structure degrades and fails. However, not many details are available regarding the interior support elements in the canister. For the current model, the support elements are assumed to be continuous along the length of the canister.

### ***Single-Rod Model***

This model is used to calibrate the bending behavior of a single fuel rod or a single control rod cladding. Because the segments themselves are rigid and the deformability is concentrated at the contacts, the contact stiffness is proportional to the modulus of the rod and inversely proportional to the segment size. The user inputs the modulus and tensile strength of the material and the contact stiffness and strength are calculated within the model.

For control rod guide tubes, the rod is loaded as a cantilever and the displacement profile for a given small load is compared with the analytical solution. Then, the load is increased gradually until the rod breaks, and the failure load is compared to the analytical solution. Because the rod is hollow, both the modulus and tensile strength are scaled down in proportion to the moment of inertia of the cross-section, i.e., the reduction factor is calculated as  $F_r = 1 - (r_i^4/r_o^4)$ , where  $r_i$  is the internal radius and  $r_o$  is the external radius of the rod. Figure 30 shows a good match obtained between displacements from the analytical solution and those obtained from the model.

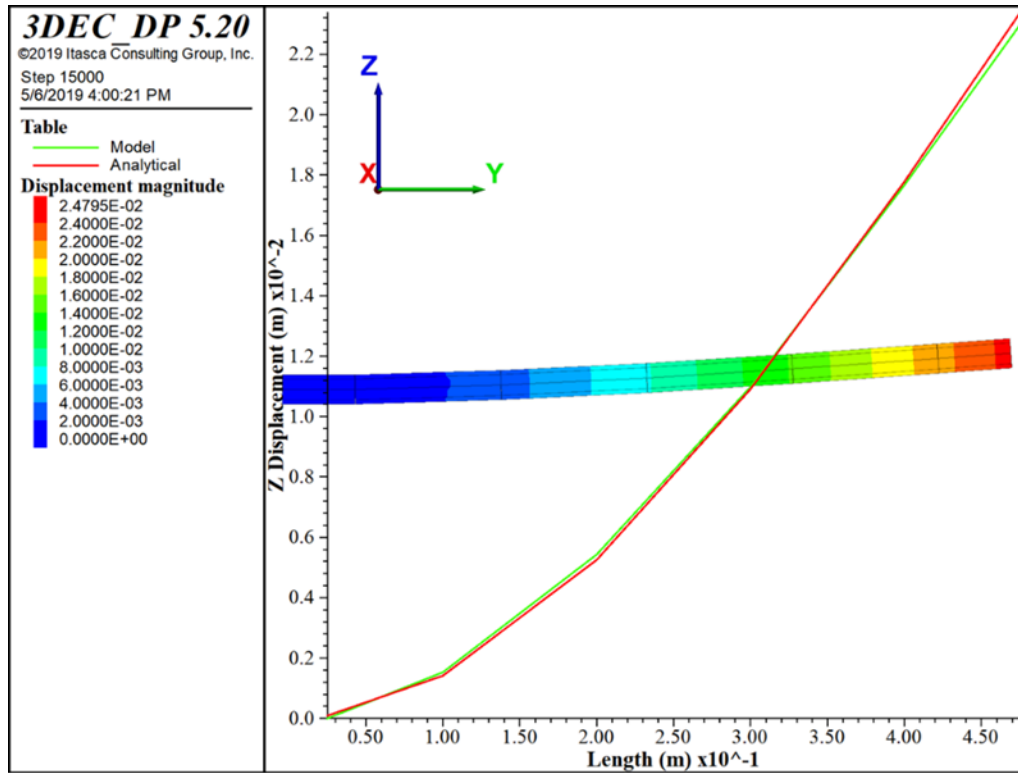


Figure 30. Single rod model of guide tubes showing comparison of displacement profiles (m) for cantilever bending obtained using analytical solution and 3DEC model.

The fuel rod is loaded in pure flexure by imposing rotation of both ends so that the resulting moment-curvature curve can be compared with laboratory data (Ahn et al., 2018) as shown in Figure 31. The rod behaves as a composite beam with spent fuel inside showing brittle behavior and the surrounding Zircaloy cladding being ductile. To model this composite system, the peak tensile strength is calibrated accounting for both the spent fuel and the cladding. A single contact between two segments is composed of multiple sub-contacts. Once a sub-contact fails, it is assumed that the tensile strength of the fuel portion falls to zero (brittle failure) and a residual strength equal to the contribution from the cladding remains (ductile failure). The composite behavior obtained using this technique compared with the data from laboratory tests, as shown in Figure 31, indicates good agreement between the two.

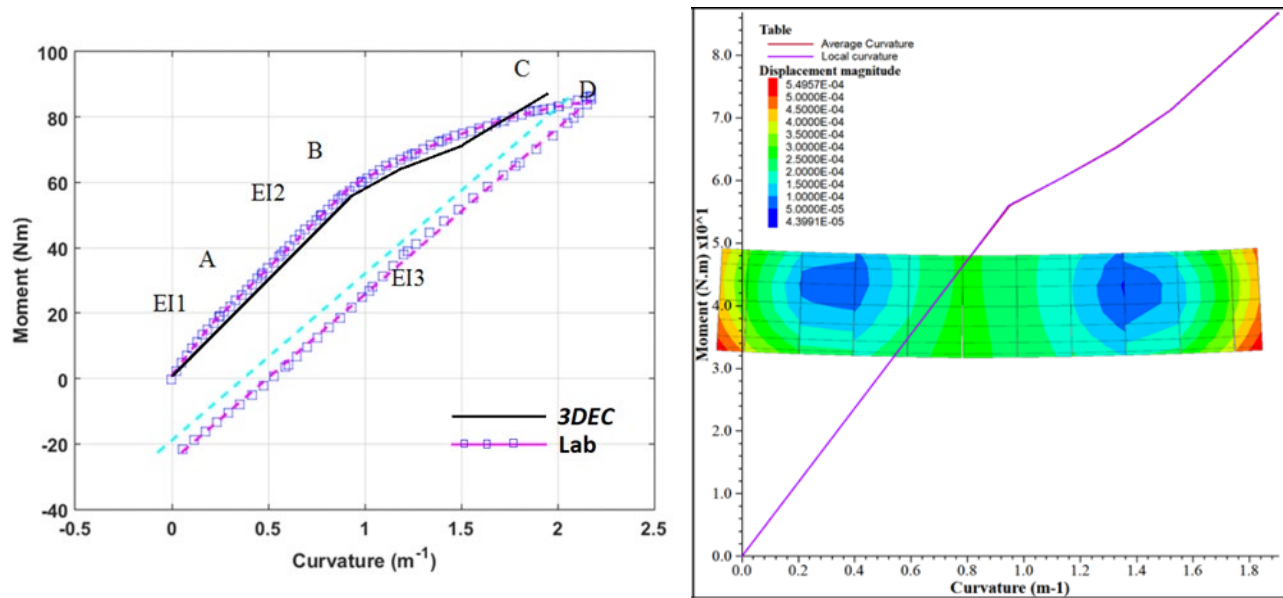


Figure 31. Moment-curvature responses for a single fuel rod obtained from laboratory tests (left) and from 3DEC model (right).

The ultimate capacity of the fuel rods in bending depends on the failure strain for the cladding material (Zircaloy), which is typically around 5 to 6% (Section 2). Using Euler's beam theory, the failure strain can be related to curvature as  $\epsilon_f = yu''$ , where  $u''$  is the curvature and  $y$  is the distance from the neutral axis. For a typical external radius of 4.5 mm for the cladding, this corresponds to an ultimate curvature of around 11 to 13 m<sup>-1</sup>, which is much higher than the curvature loading for the fuel rods in the laboratory tests (Ahn et al., 2018). In 3DEC, if the two block faces forming that contact move away by more than a certain distance (*ctol*) then the contact is deleted. To allow the fuel rods to remain intact until the ultimate curvature is reached, the *ctol* value needs to be increased to  $\epsilon_f l_e$ , where  $l_e$  is the discretization length for the rod. For typical values, this corresponds to a *ctol* value of around 0.005 m. However, increasing the *ctol* value also increases the number of contacts detected and hence the amount of memory and computation time. Because the fuel rods are not expected to reach such high curvature values in these simulations, a value of 0.0025 m is used. No breakage observed in fuel rods in subsequent simulations confirms that this parameter can be reduced further if needed.

Summaries of all the geometry-related parameters for the 3DEC models are provided in Table 4 and for material-related parameters in Table 5.

Table 4. Parameters related to model geometry.

Parameter	Typical Value	Comment
<b>Fuel Rod Parameters</b>		
Length of fuel rod	3.85 m	
Outer radius of rod	4.75 mm	
Thickness of fuel rod cladding	0.57 mm	
Number of segments for cross-section	8-12	Numerical parameter
Number of segments along length per spacer	5-8	Numerical parameter
<b>Fuel Assembly Parameters</b>		
Number of rods in an assembly in each direction	17	
Spacing between rods in an assembly (center to center)	12.6 mm	
Clearance between fuel assembly and basket	4 mm	
<b>Spacer Grid Parameters</b>		
Spacing between spacer grids (center to center)	0.58 m	
Number of spacer grids	7	
Length of spacer grid	54.4 mm	
Thickness of spacer grid plate	3.1 mm	Set to constrain rods
<b>Basket Parameters</b>		
Number of assemblies in the basket	32	
Thickness of basket plate	10 mm	
<b>Canister Parameters</b>		
Number of facets for canister	32	Numerical parameter
Thickness of canister	30 mm	Not important
Clearance between basket and canister	12.5 mm	No data available
Width of supports at bottom	75 mm	No data available
Width of supports at top	30 mm	No data available
Height of vertical part of supports	95 mm	No data available
Thickness of additional support in canister	10 mm	No data available
Clearance of basket from supports	2 mm	No data available

Table 5. Parameters related to material properties.

Parameter	Typical Value	Comment
Density of spent fuel (UO <sub>2</sub> )	10,970 kg/m <sup>3</sup>	
Density of Zircaloy (cladding material)	6560 kg/m <sup>3</sup>	
Density of stainless steel	8000 kg/m <sup>3</sup>	
Density of Metamic-HT	2690 kg/m <sup>3</sup>	
Young's modulus for Zircaloy	100 GPa	
Tensile strength for Zircaloy	600 MPa	
Equivalent modulus for spent fuel + cladding	100 GPa	Calibrated
Tensile Strength for spent fuel + cladding	450 MPa	Calibrated
Residual tensile strength for spent fuel + cladding	200 MPa	Calibrated

### Simplified Basket Model

In this model, each fuel assembly is represented as a single set of coarsely discretized blocks along the length with equivalent density, modulus, and strength. In other words, an equivalent continuum is used to represent the rods. All the values are calculated internally from the material parameters used for the detailed model. Reducing the detail in modeling the fuel assemblies (and fuel rods specifically) greatly speeds up the computation and allows seismic analyses to be run in one to two days. This is a good assumption if the individual rods in the assemblies do not break. In case the rods do break, a hybrid approach can be used to model the fuel assembly of interest in more detail while using the simplified approach for the rest of the assemblies. This allows for correct modeling of the interactions between assemblies, and for study of the response of a particular assembly without imposing significant computational overhead. Different models could then be run to study the behavior of assemblies at different locations. The model setup is shown in Figure 32.

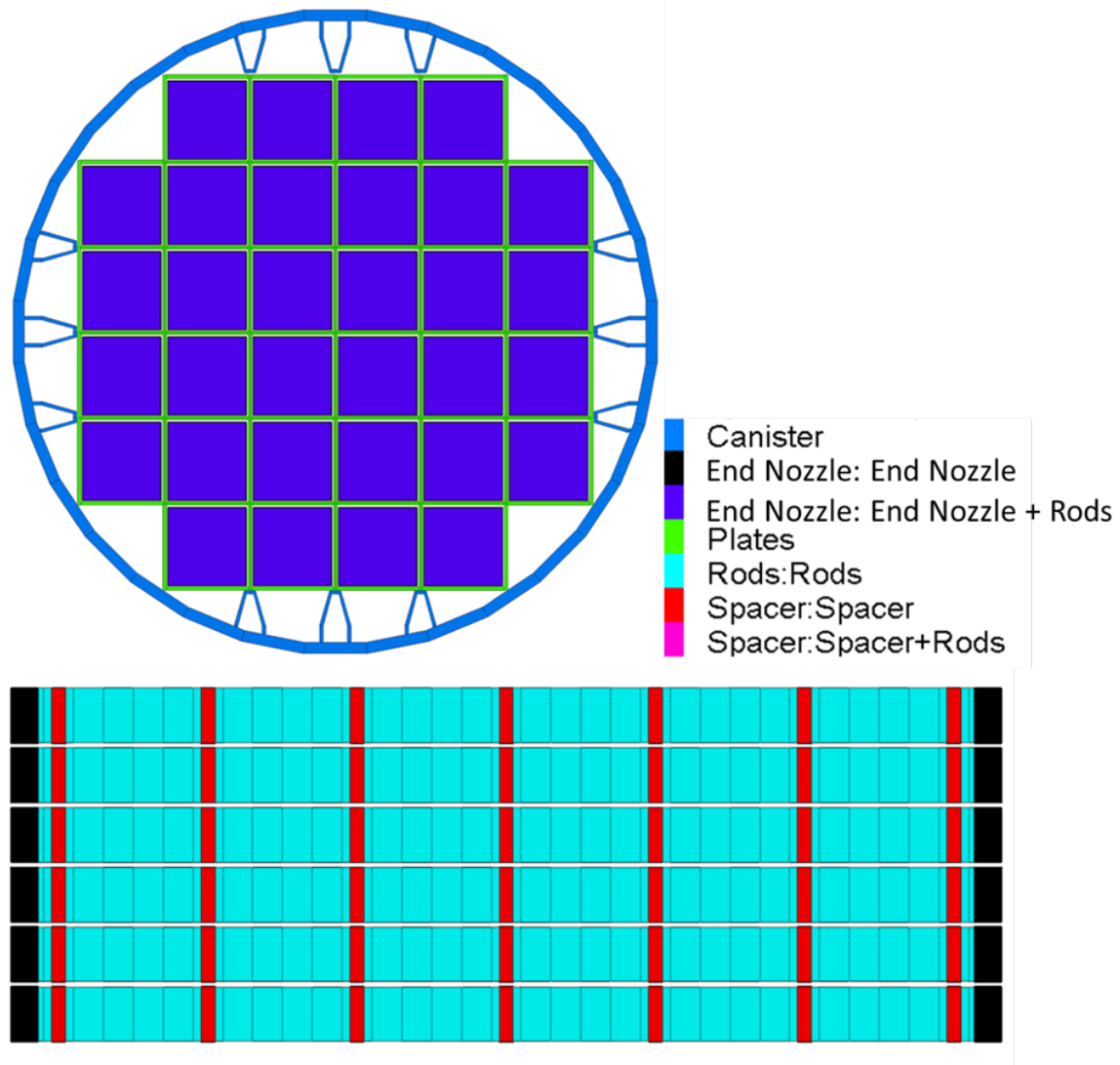


Figure 32. Model setup showing different components in the simplified model.

## Static Analyses

Both the detailed and the simplified models were run in three stages to model the effect of degradation of structural components caused by corrosion on the basket collapse.

- Stage 1: The first stage is to establish initial equilibrium under gravity with fuel assemblies resting on the basket plates and the basket structure supported by the canister internal supports and the canister itself.
- Stage 2: It is assumed that the basket plate structure has corroded away by deleting the basket plates, and the fuel assemblies stack up on top of each other. The final configuration is controlled by the configuration of internal supports in the canister. More details will be added to this stage in future work where the basket structure will be degraded progressively by breaking connections between basket plates based on the insights obtained from the *FLAC3D* model.
- Stage 3: The spacer grids corrode away next and the model is cycled to equilibrium again. The end nozzles and control rod guide tubes are still intact. Although the spacer grids are also made of Zircaloy, the same material used for fuel rod cladding, they have much greater surface area and are thus likely to corrode before the fuel rod cladding.

The final configuration in Stage 3 for the detailed model is shown in Figure 33 and for the simplified model in Figure 34. The detailed model is still not in complete equilibrium with the bottom leftmost and rightmost assemblies at the bottom still moving very slowly towards the center. However, the assemblies are no longer falling, and the subsequent minor adjustments are unlikely to damage fuel rods. The final configurations from both models are comparable.

However, the detailed model is capable of modeling rod failure mechanisms should they occur. For one of the simulations, the model of fuel rods does not include contribution from fuel pellets, and the bending of fuel rods due to gravity at the end of Stage 1 can be observed (Figure 35). Also, the internal supports in the canister are narrower, resulting in a larger height of fall for the fuel assemblies for Stage 2, which then results in rod failure and subsequent pulling out of rods from end nozzles at the end of Stage 3, as shown in Figure 36. The results shown in Figure 35 and Figure 36 are for illustration purposes to demonstrate capability of the detailed model to simulate both large deformation and failure of the fuel rods. If the degradation of the fuel rods is negligible, they behave elastically, and approximation by the simplified model of the final configuration after Stage 3 shown in Figure 34 is realistic.

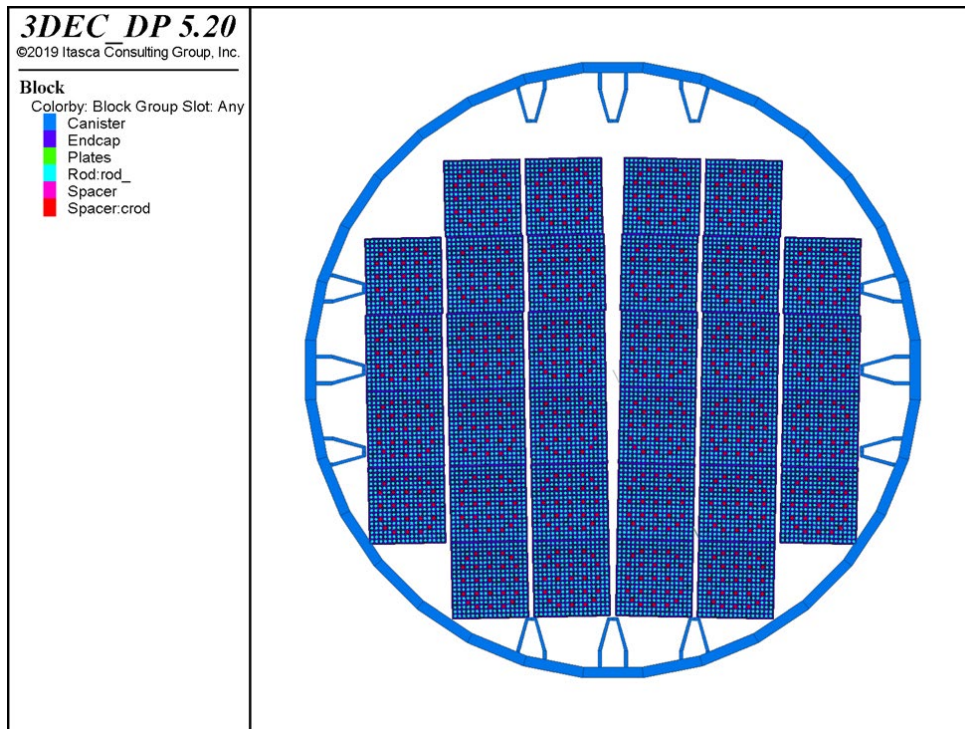


Figure 33. Final configuration at the end of Stage 3 for the detailed model.

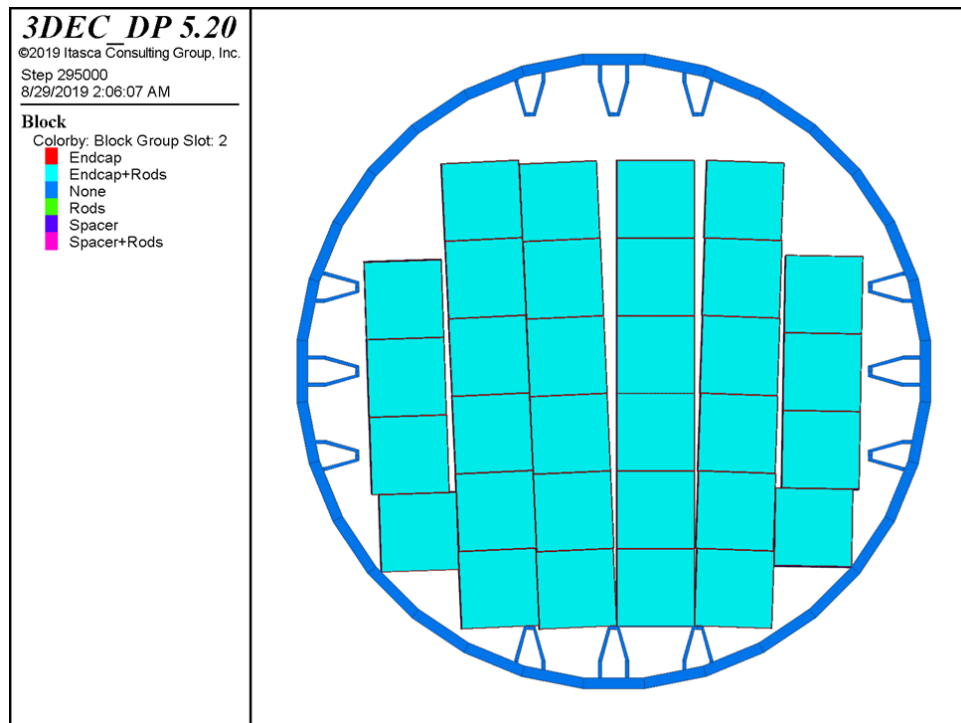


Figure 34. Final configuration at the end of Stage 3 for the simplified model.

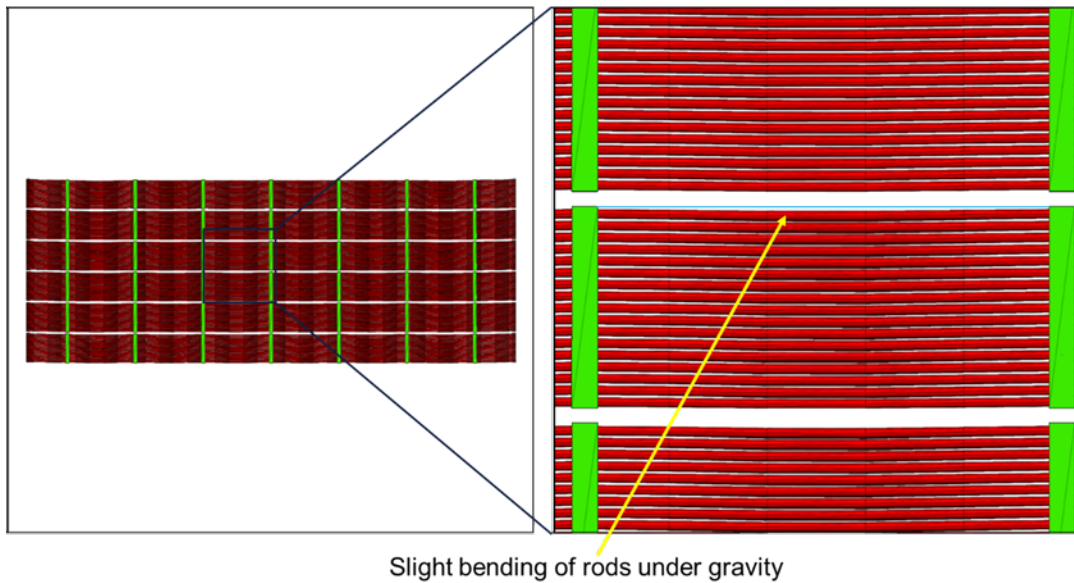


Figure 35. Bending of rods under gravity in the model that neglected contribution from fuel pellets.

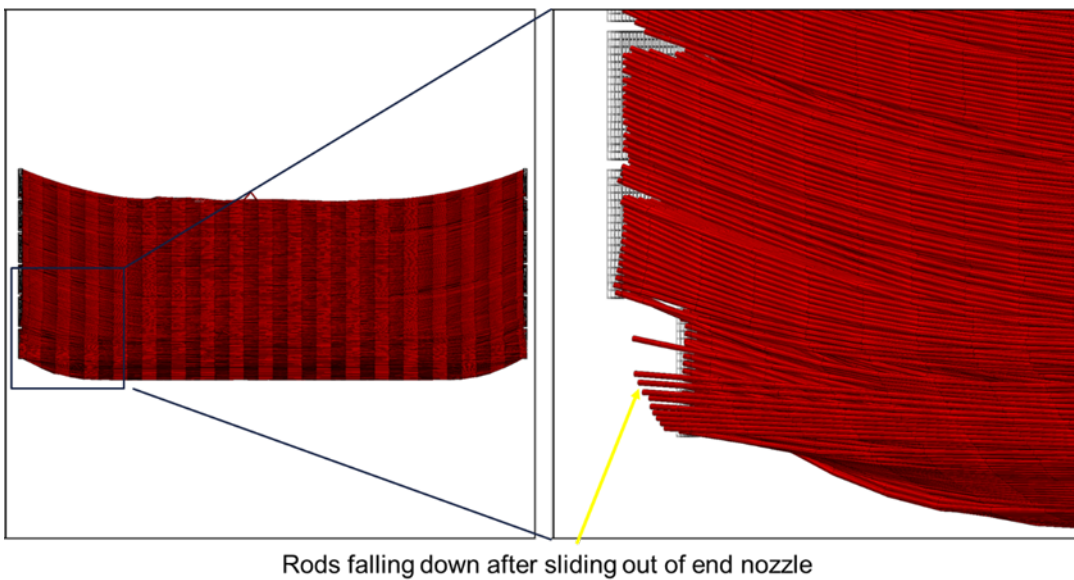


Figure 36. Rods breaking and sliding out of end nozzles at the end of Stage 3 for the model with greater height of fall due to narrower canister supports.

### Seismic Analyses

After Stage 3 of the static analysis, a seismic analysis is carried out using the simplified model. It is assumed that the canister is embedded in ground at least partially so that the ground motion is transferred directly to the canister. To model the seismic shaking, all three components of the

ground motion, as shown in Figure 37, are applied as velocities for the canister in three directions. For this demonstration, a ground motion from the set for the 5.35 m/sec PGV level used for the Yucca Mountain project was selected. The snapshots of configuration at four different instants of time are shown in Figure 38. As most of the energy in ground shaking is in the first five seconds, relatively smaller changes are observed after five seconds. The results indicate that there is some bending and possible twisting of the fuel assemblies during the shaking. The assemblies showing the most bending can be investigated in detail using a hybrid model as suggested before.

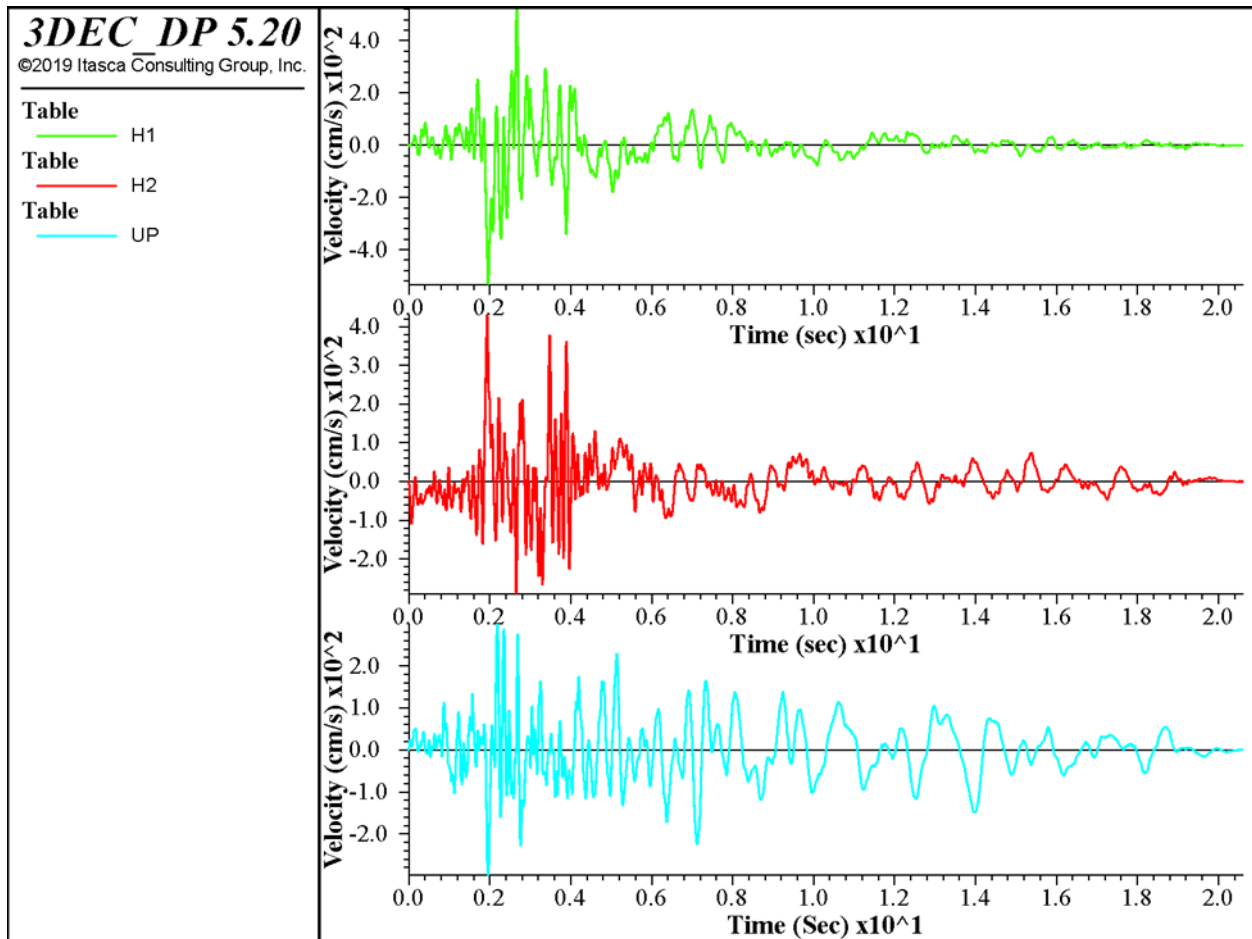


Figure 37. Velocity time histories of three components of ground motion used for shaking of the canister.

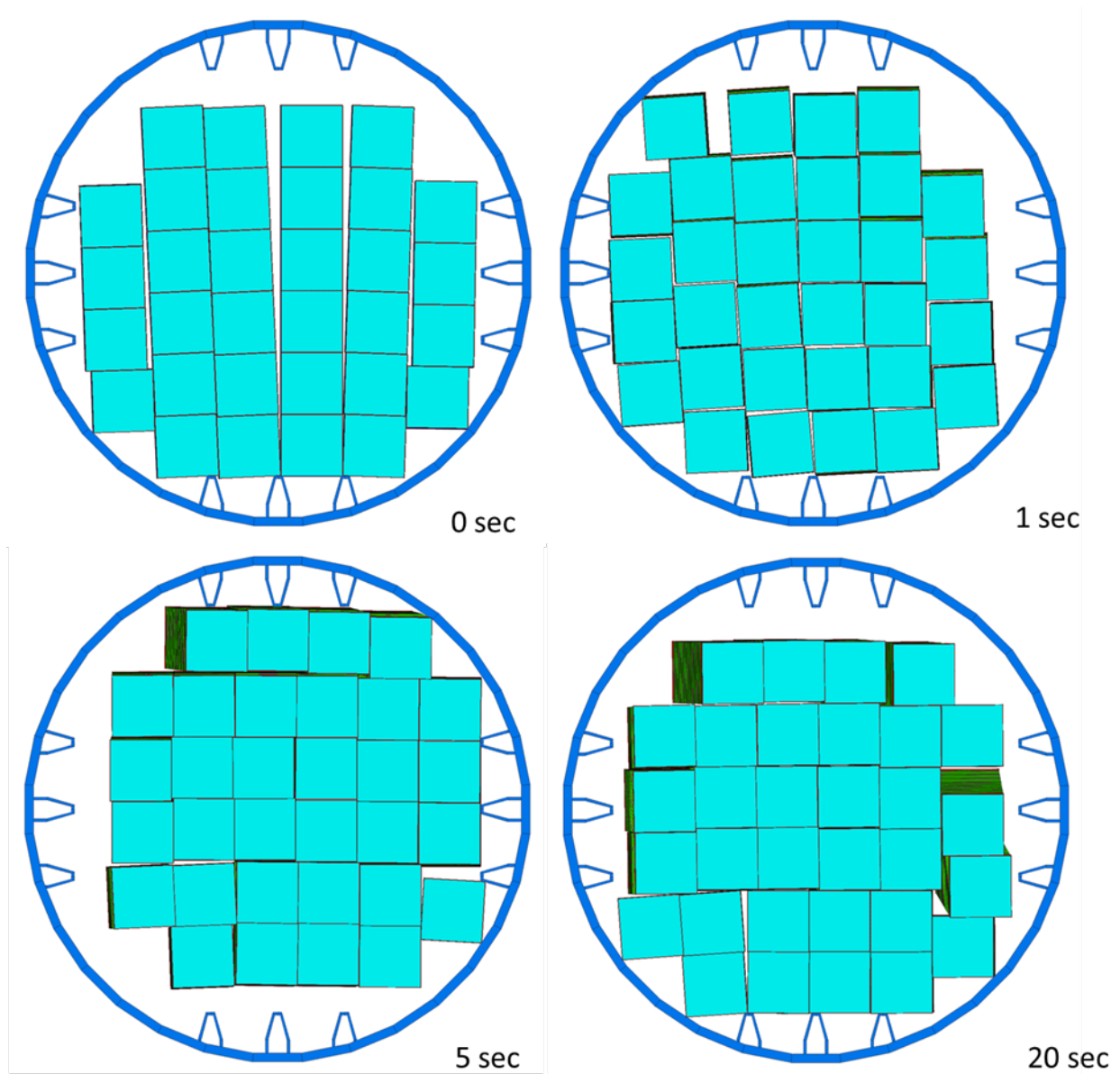


Figure 38. Model configuration at different times during the shaking.

### 5.3 Discussion

Models for simulation of basket collapse using *3DEC* software have been developed and used for simulation of the collapse of an MPC-32® fuel basket caused by corrosion of the structural components. In order to optimize the run times, two models were created:

**Detailed Model** – This version contains explicit representation of all important basket structural components, including the fuel rods. In this model, although the detail of the cross-section of the fuel rods (with fuel pellets inside Zircaloy cladding) is not explicitly represented, the fuel rod model matches the experimentally obtained moment-curvature response of the fuel rods.

**Simplified Model** – Simulation of the basket collapse (by removing corroded structural elements like plates and spacer grids) showed that none of the rods fail. Consequently, there was justification to create a simplified model in which the fuel assembly is represented as an equivalent continuum. This allowed faster run times for the simulation of complete basket collapse from total degradation of the plates and the spacer grids, as well as simulation of the effects from seismic shaking of the degraded structure.

As noted above the locations of the basket side supports is crucial to predicting gross deformations of the fuel and basket. Hence, the *rotational orientation* of the waste package in a repository could strongly affect the predicted deformations.

Future work should determine critical failure modes for basket plates using continuum mechanics (*FLAC3D*) and incorporate the results into the *3DEC* basket degradation model. Degraded components (fuel rods, basket plates, and other components) can be represented as disaggregated pieces rather than removing degraded components from the model. Disaggregation can include more realistic criteria for separation of fuel rods from the nozzle blocks at the ends. Also, randomness of degradation can be added so that components fail progressively rather than all at once.

A new application for the simplified basket degradation model would couple the fuel, basket, and canister shell to simulate external loading of DPCs by ground water pressure in a saturated repository, after breach of the overpack but prior to breach of the canister. Buckling of the shell, if it occurs, could rearrange the fuel and basket, and significantly reduce void space in the canister.

The detailed basket model can also be used to represent degraded configurations with postclosure disposal criticality control features added to the basket or to fuel assemblies. For example, the model could be used to study degradation of PWR fuel assemblies that have disposal control rods inserted into guide tubes. Extending the model to BWR fuel, it could represent the configuration of fuel channels designed specifically for criticality control (e.g., channels made from advanced neutron absorbing alloys).

## **6. Waste Package Breach Model**

Azadeh Riahi, Jason Furtney, Varun, and Branko Damjanac (Itasca Consulting Group)

### **6.1 Introduction**

This model is a first iteration that investigates the effect of internal pressure such as could result from a criticality event, on a pre-existing breach in the DPC shell and/or the disposal overpack. Over many thousands of years it is envisioned that the DPC and overpack will be breached by initial cracks (fractures) due to SCC. Breaches in both the canister and overpack could allow ground water to fill the canister. After partial or complete flooding by ground water, neutron-absorbing DPC components are likely to degrade, whereupon a criticality event could occur. Such an event would create transient temperature and pressure conditions, and the internal pressure could cause the initial fractures in the canister and overpack to widen, and possibly to grow. It is important to understand the potential for changes in hydraulic transmissivity between the canister and surroundings because: 1) it may control the potential for, and frequency of subsequent criticality events; and 2) it may control the release of radionuclides from the canister.

### **6.2 Methodology**

The modeling assumes that the canister has an initial breach (crack) in both the canister and overpack, and that the canister is filled with water. *FLAC3D* (Itasca 2017) is used to model deformation, yielding and fracturing of the canister and overpack. Figure 2 (Section 3) provides a schematic of the model.

Four model geometries are considered: two cases with a longitudinal fracture and two cases with a circumferential or “hoop” fracture. The fractures are perpendicular to the outer surface of the cylinder wall. For each fracture orientation, two fracture locations are considered: one in the middle of the canister and one near the base. Figure 39 shows the model geometries considered. For each geometry three different values of initial fracture length are considered. For each geometry and fracture length, two canister thicknesses are considered: 1.2 cm to represent the DPC shell, and 2.5 cm to represent the overpack. The model does not represent the canister and overpack simultaneously; each component is modeled separately.

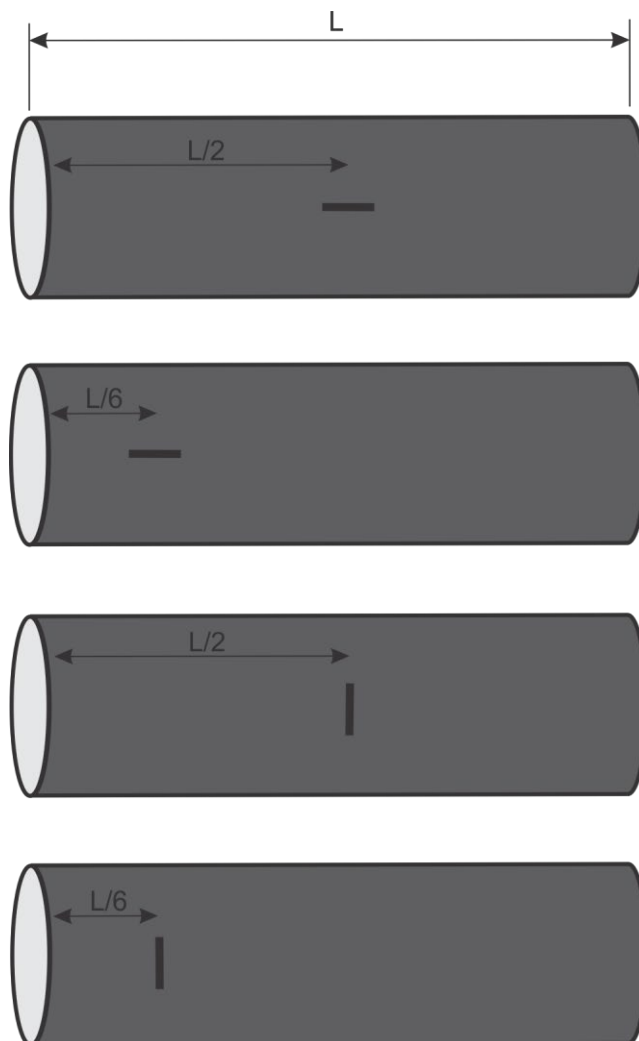


Figure 39. Analyzed locations and orientations of the initial fractures.

A spatially uniform and temporally constant pressure is applied to the inner surface of the canister, so the models are quasi-static (they neglect inertial effects from rapid loading, although this could be activated). The model is solved to equilibrium. The internal canister pressure during an actual criticality event may vary with time due to evolving internal energy and due to steam potentially escaping the package. To keep the initial modeling simple, the thermal hydraulics of the water in the canister are not considered. This analysis considers the limiting case where pressure is constant for long enough to cause fracture growth or other failure in the canister. Once mechanical equilibrium is reached at a given pressure, the pressure is increased, and mechanical equilibrium is reestablished. The model is stopped when the critical pressure (that causes vessel failure by fracture growth or yielding of the cylinder wall) is reached. The initial residual stresses, which are responsible for development of the initial crack, are not considered in the present modeling. The stresses causing unstable fracture growth or yielding of the canister wall are greater than the residual stresses. Also, the residual stresses are localized.

### 6.3 Canister and Disposal Overpack Properties

The geometric details of the canister are listed in Table 6.

Table 6. Geometric details of canister.

Component of HI-STAR 100 System	Inner Radius {m [in]}	Outer Radius {m [in]}	Height {m [in]}
Multipurpose Canister Base Plate	0.0 [0.0]	0.8683625 [34.1875]	0.0635 [2.5]
Multipurpose Canister Shell	0.8556625 [33.6875]	0.8683625 [34.1875]	4.5212 [178.0]
Multipurpose Canister Lid	0.0 [0.0]	0.8683625 [34.1875]	0.2413 [9.5]

For the present modeling both the canister and the overpack are assumed to be made of stainless steel with the same (typical for SS304L) properties. Holtec (2018) indicates that the canister is made of Alloy X, meaning one of several types of stainless steel (Type 316, Type 316LN, Type 304, Type 304LN, or duplex alloy S31803).

The lower values of Young’s modulus, yield and ultimate strengths for stainless steels are reported by Holtec (2018). The minimum values of Young’s modulus for different stainless-steel alloys are 194 GPa at 38°C and 182 GPa at 204°C. The Young’s modulus of 200 GPa, the density of 8,031 kg/m<sup>3</sup>, and Poisson’s ratio of 0.3 (at ambient temperature) are selected.

The yield strength of stainless steel at 200°C in a linearly elastic–perfectly plastic model is assumed to be 445 MPa. This value represents the ultimate strength of stainless steel and is selected based on the considerations discussed in Appendix C. Because of potential variations in temperature, use of different stainless steel grades, and reported yield and ultimate strengths, a reduction factor of 95% is applied to this value. Also, the mechanical response of stainless steel is not perfectly plastic, and because of the variation between yield and ultimate strengths, a second set of analyses with a more conservative yield strength value of 300 MPa representing the average of yield and ultimate strengths is also carried out. Nevertheless, the pressure requirement for total collapse of the canister is presented using the ultimate strength.

For these calculations the submerged density of steel is used. (The density of water at 200°C of 850 kg/m<sup>3</sup> is subtracted from the steel density.) The pressure required to keep the water in a liquid state at a temperature of 200°C is approximately 1.5 MPa, which is below the pressure requirement to initiate fracturing. Therefore, it is assumed that the water is in the liquid state. The elastoplastic response of steel is represented by the von Mises criterion.

In this study, it is assumed that propagation of the initial crack is in Mode I (i.e., opening) and governed by linear elastic fracture mechanics (LEFM). Mode I fracture toughness,  $K_{Ic}$ , for stainless steel can vary between 40 and 100 MPa-m<sup>1/2</sup>. The value of 50 MPa-m<sup>1/2</sup> is assumed for  $K_{Ic}$  of the stainless-steel material (Matthews 1973) of the canister and overpack. Fracture toughness was not provided in the available Holtec references.

Modeling fracture propagation numerically presents significant challenges and can be computationally intensive. In this study, it is assumed that fracture will propagate along the specified trajectory (i.e., pre-defined fracture surface). A *FLAC3D* interface along the assumed path of fracture growth is explicitly introduced into the model geometry and is bonded initially.

The orientations of the stress tensors indicate that the assumptions of the fracture propagation trajectories (i.e., straight along the canister and straight in the hoop direction) are correct for all analyzed initial crack configurations.

The condition of the fracture propagation was determined using the LEFM. The approximation by the LEFM is justified because the process zone for the assumed steel properties,

$$l = (K_{IC}/\sigma_y)^2/\pi \quad (3)$$

where  $\sigma_y$  is the yield strength, is estimated to be approximately 1 to 3 mm which is relatively small compared to the shell thickness, and the assumed initial crack lengths for which the canister failure is controlled by fracture propagation. The tensile strength of the interface is calculated such that the fracture toughness ( $K_{IC}$ ) is represented correctly using

$$K_{IC} = \alpha \sigma_t \sqrt{\delta} \quad (4)$$

where  $\alpha$  is a dimensionless quantity with value near one,  $\sigma_t$  is the tensile strength and  $\delta$  is the *FLAC3D* interface element length. From the above equation, the numerical value of fracture toughness depends on discretization, i.e., zone size. Therefore, to match the fracture toughness, tensile strength must be selected based on the zone size.

## 6.4 Results

### Critical Pressure for Steel Yielding

Before presenting the results of the numerical analysis it is worth considering the expected critical pressure for yielding in an infinitely long steel cylinder. Failure of the canister due to plastic yielding (without a pre-existing crack) occurs when internal pressure reaches the critical value given by the following relation:

$$P_c = \sigma_y t r \quad (5)$$

where  $P_c$  is the critical pressure,  $\sigma_y$  is the steel yield strength,  $t$  is the canister thickness and  $r$  is the canister radius. The DPC shell, with 1.2 cm thickness, yields at a critical pressure of 4 MPa, while an overpack, with 2.5 cm thickness, yields at a critical pressure of 8.4 MPa. This is relevant because fractures cannot grow if plastic yielding happens first. (If perfectly plastic behavior of steel is assumed, yielding of the canister is also failure of the canister.) The axial stress due to pressurization of the canister lids is less than the hoop stress. It is expected (see yielding pressures in Figures 41 and 42) that the actual internal pressure at canister failure due to plastic yielding will be higher because of the influence of the ends of the cylinder.

### Numerical Model Results

Two failure criteria are possible for both the canister and overpack: fracture propagation and plastic yielding. To accommodate both failure modes each model is run twice: 1) using an elastic constitutive behavior for the steel and a LEFM criterion for fracture propagation; and 2) an elastoplastic criterion for the steel, without an initial fracture.<sup>1</sup> These models must be run separately because the plasticity occurring in the coarse mesh is over a larger length than the expected fracture process zone of 1 to 3 mm. To represent fracturing in *FLAC3D*, the plasticity in

---

<sup>1</sup>Because the elastoplastic models do not include a pre-existing fracture, a total of two elastoplastic models, one representing canister and one representing overpack, were analyzed.

the process zone is implicitly represented in the Mode I fracture toughness value and local plastic dissipation is not explicitly represented in the model. Further, the LEFM solution is suitable in this case because the initial fracture lengths are an order of magnitude larger than the expected process zone size (1 to 3 mm). The model that fails at the lowest pressure is considered the critical mechanism for that configuration. Figure 40 shows a typical result for displacement in the longitudinal fracture cases. Figures 41 and 42 show calculated critical pressures for the longitudinal and hoop fractures, respectively. The orange curve shows the fracture propagation criterion and the blue curve shows the plastic yielding criterion. Whichever is lower becomes the actual failure mechanism. The results are presented as composite curves in which the solid line indicates the behavior. A dashed line is plotted when the critical fracture propagation pressures are above the yield strength.

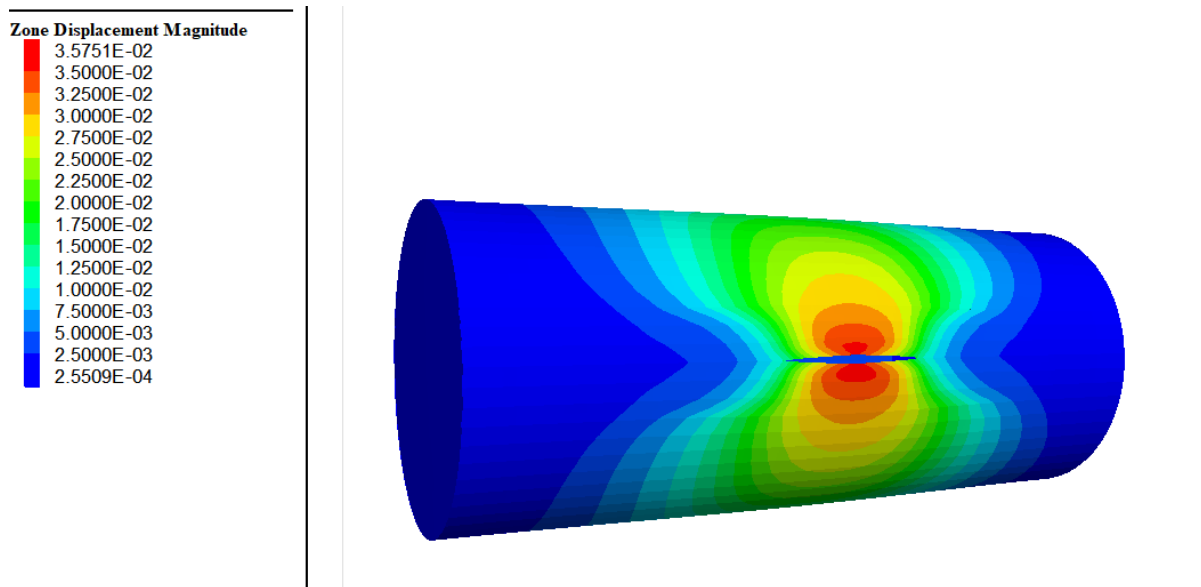


Figure 40. Typical results (displacement magnitude contours shown in meters) for a longitudinal fracture.

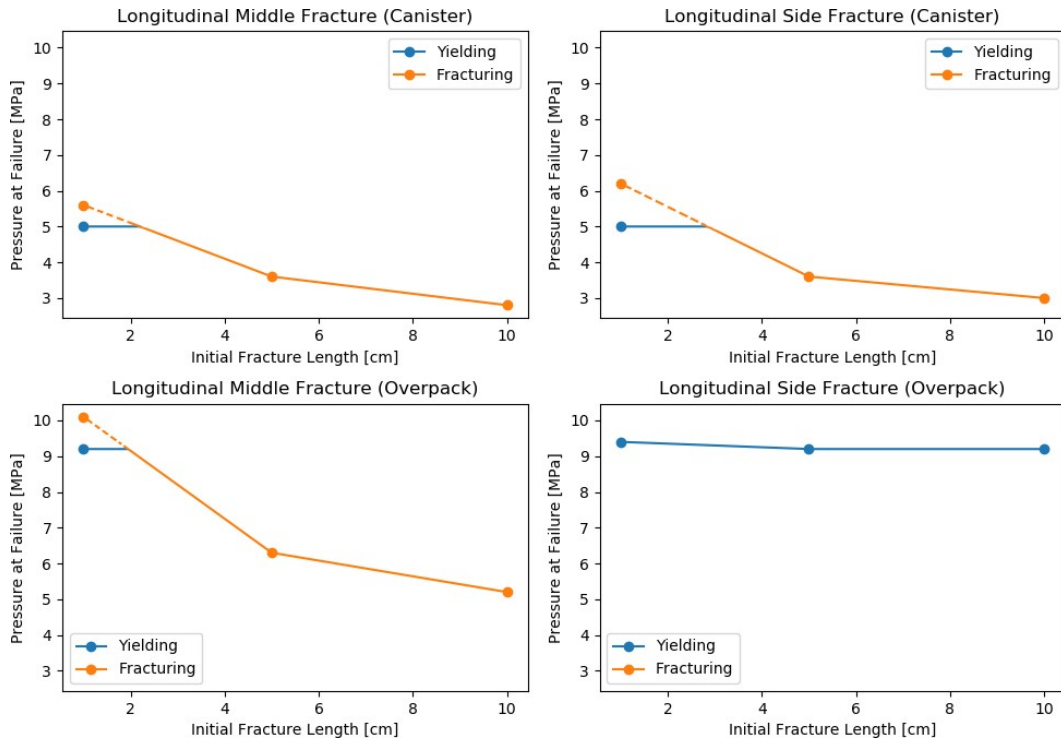


Figure 41. Critical pressure for longitudinal fractures of different lengths in both the canister and the overpack.

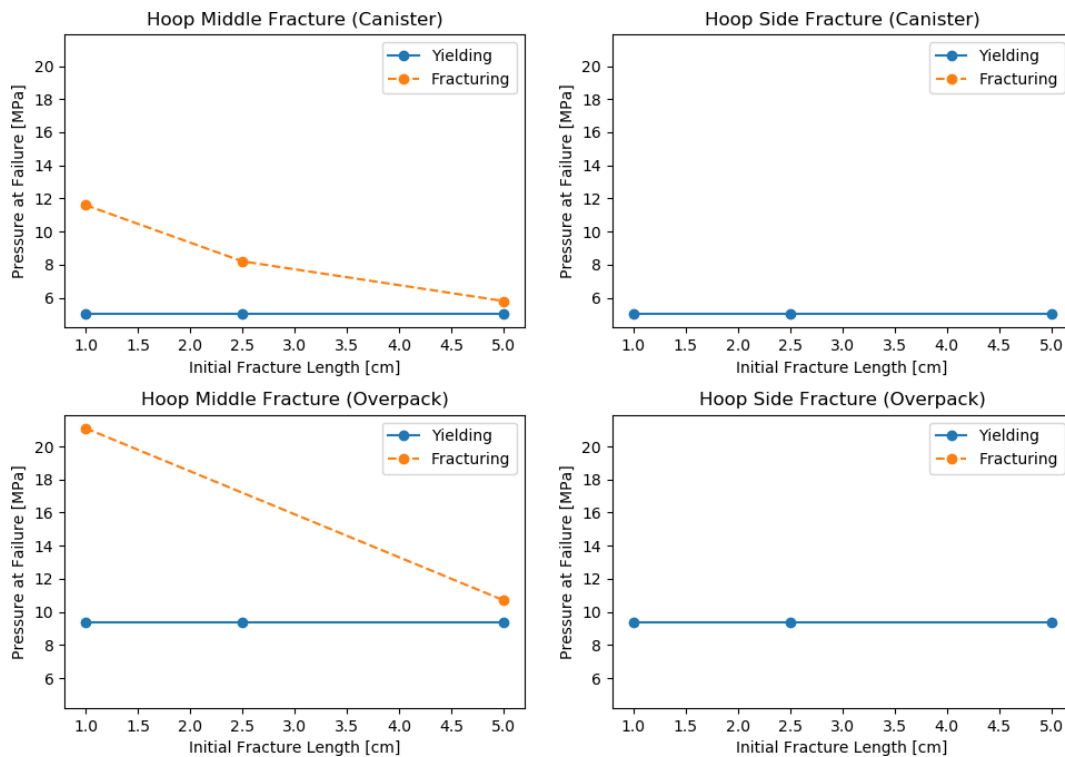


Figure 42. Critical pressure for hoop fractures of different lengths in both the canister and the overpack.

## 6.5 Discussion

The following observations are made:

- Fracture growth will not happen if the ultimate strength of stainless steel is reached before critical pressure for fracture growth.
- In all cases analyzed in this study, the failure processes (both fracturing and plastic yielding, if perfectly plastic model is assumed) are unstable. Once failure starts, it continues at a constant pressure. Note that these models are quasi-static, with constant pressure. This behavior could change in a dynamic model that includes inertial effects and rapid loading.
- For both the canister and overpack, longitudinal initial fractures around 1 cm and longer will grow due to internal pressurization.
- The critical pressures required to fail the overpack are greater than those for the thinner canister.
- For both the canister and overpack, hoop fractures for the assumed initial fracture lengths less than approximately 6 cm will not grow before plastic yielding occurs. For fracture length more than approximately 6 cm, failure is controlled by fracture propagation.

The next steps in modeling WP breach behavior should be to account for residual stresses and hydrostatic pressure conditions, then calculate a dynamic pressure-time history by adding a pulse of heat energy to a constrained volume of fluid representing a saturated WP. A scoping model can be built to include expansion of the fluid and heat conduction inside and outside the WP, and to couple internal pressure to transmissivity of the WP breach. Breaches in both the DPC shell and disposal overpack should be considered in a series combination. The venting rate for water mass from the package would be a function of breach morphology, energy input, and other factors found to be important. This approach would be scoping because it uses a low-order approximation for the behavior of the DPC internal volume (see Section 7).

## 7. Coupling of Mechanical and Porous-Medium Flow Models

Jason Furtney and Branko Damjanac (Itasca Consulting Group)

This section describes preliminary work to couple *FLAC3D* with *TOUGH3*, a porous-medium heat-mass transport simulator. The objective is to enable coupled mechanical-thermal-hydraulic analysis of a thermal event, representing an internal criticality event in a DPC after disposal in a repository. This is a progress report on development of the coupled model.

Over thousands of years it is possible that the waste package, consisting of a DPC enveloped in a disposal overpack, will be breached and fill with ground water. Ground water could then corrode the neutron absorbing components of the DPC basket, and with water as neutron moderator, a criticality event could occur. Such an event could produce enough energy to boil water in part or all of the DPC, and pressurize the canister. Internal pressurization could cause the breaches in the DPC shell and overpack, which are initially fractures, to deform and grow. For these conditions, the exchange of heat and water mass between the DPC and its surroundings would control the energy and frequency of subsequent criticality events. The history of criticality events and degradation of the waste form and WP, would control release of radionuclides from the package (source term). The motivation for this work is therefore to better understand the potential for transient or steady-state, periodic criticality events to cause canister damage and impact the release of radionuclides (source term).

### **FLAC3D Background**

*FLAC3D* stands for Fast Lagrangian Analysis of Continua in Three Dimensions. The software predicts stresses and displacements in a continuous medium using a robust explicit integration technique (Itasca 2018). It can use complex nonlinear material models, accounting for complex geometries, including structural elements, and accounting for the influences of fluid and heat on mechanical deformations. The software consists of a graphical user interface, a solution engine, and a *Python* scripting engine. The combination of the robust solution procedure and the flexibility of the *Python* scripting engine allows *FLAC3D* to easily integrate with other solvers to include additional physics in the solution. *FLAC3D* has a porous flow capability, but it cannot handle multi-component flows with phase changes.

*FLAC3D* uses a mesh of hexahedral (or degenerate hexahedral) elements for which stresses and strains are defined over the elements and velocities are defined on the gridpoints. The *FLAC3D* equation of motion is

$$\rho_r \frac{dv}{dt} = \nabla \sigma + \rho_r \mathbf{g} \quad (6)$$

where  $\sigma$  is the stress tensor,  $\rho_r$  is rock density,  $\mathbf{g}$  is acceleration due to gravity, and  $\mathbf{v}$  is velocity. The strain-rate tensor  $\dot{\epsilon}$  is calculated from gridpoint velocities,

$$\dot{\epsilon} = \frac{1}{2} (\nabla \mathbf{v} + (\nabla \mathbf{v})^T) \quad (7)$$

and strain is given by

$$\epsilon = \frac{1}{2} (\nabla \mathbf{u} + (\nabla \mathbf{u})^T) \quad (8)$$

where  $\mathbf{u}$  is the gridpoint displacement vector. The strain is composed of elastic, plastic, and thermal parts. The strain increment can be written as

$$\Delta\epsilon = \Delta\epsilon^e + \Delta\epsilon^p + \Delta\epsilon^T \quad (9)$$

where the superscripts refer to the elastic, plastic, and thermal parts. The change in mean stress due to temperature change is

$$\Delta\sigma^m = -3K\beta\Delta T \quad (10)$$

where  $\beta$  is the coefficient of thermal expansion,  $K$  is bulk modulus, and  $\Delta T$  is the temperature increment. An arbitrary constitutive law relates increments in strain to increments in stress. The constitutive laws can be an arbitrary function of stress, strain, and loading history. The constitutive models operate on effective stresses,  $\sigma'$ ,

$$\sigma' = \sigma - \alpha IP \quad (11)$$

where  $\alpha$  is the Biot coefficient,  $P$  is the fluid pore pressure, and  $I$  is the identity matrix. *FLAC3D* uses a finite difference approximation and solves these equations forward explicitly with (numerical) damping to reach a quasi-static equilibrium. The model can also be run in a dynamic mode with physically realistic damping.

### **TOUGH3 Background**

*TOUGH3* stands for Transport Of Unsaturated Groundwater and Heat version 3. The software was developed by Lawrence Berkeley National Laboratory (LBNL) to solve fluid and heat flows in multiphase, multi-component fluid mixtures in saturated or unsaturated porous and fractured media (Jung et al. 2018). *TOUGH3* includes equation of state (EoS) modules for common fluid mixtures, including water, air, oil, gas, and brine. The *TOUGH* family of software is widely used to study CO<sub>2</sub> sequestration, gas and oil flow, enhanced geothermal systems, underground gas storage, and nuclear waste isolation.

*TOUGH3* solves coupled nonlinear mass and energy conservation equations that are closed via an EoS. The conservation of mass for phase  $\kappa$  is written as

$$\frac{\partial}{\partial t} \mathbf{M}^\kappa - Q^\kappa = \nabla \cdot (\mathbf{q}_l^\kappa + \mathbf{q}_g^\kappa) \quad (12)$$

where  $\mathbf{M}$  is the mass per unit volume (accumulation term),  $Q$  is a mass source or sink term, and  $\mathbf{q}_l$  and  $\mathbf{q}_g$  are the liquid and gas flux terms. The definition of the phases depends on which EoS is used. In this work,  $\kappa=a$  for air and  $\kappa=w$  for water. The mass term of each phase is a sum of the liquid and gas components,

$$\mathbf{M}^\kappa = \phi S_l \rho_l X_l^\kappa + \phi S_g \rho_g X_g^\kappa \quad (13)$$

where  $\phi$  is porosity, and  $S$ ,  $\rho$ , and  $X$  are the saturation, density, and mass fraction of each phase. The flux of each component of each phase considers both advection and diffusion. The total flux of component  $\kappa$  of phase  $\psi$  is

$$\mathbf{q}_\psi^\kappa = -\rho_\psi X_\psi^\kappa \frac{k_{r\psi}}{\mu_\psi} (\nabla P_\psi - \rho_\psi \mathbf{g} \nabla z) - \rho_\psi D_v \nabla X_\psi^\kappa \quad (14)$$

where  $\mathbf{k}$  is the intrinsic permeability tensor,  $k_{r\psi}$  is the relative permeability,  $\mu_\psi$  is the dynamic viscosity, and  $D_v$  is the diffusion coefficient. Fluid momentum is neglected in porous Darcy flow, so there is no momentum equation. The energy conservation equation is,

$$\frac{\partial}{\partial t} (\phi S_l \rho_l e_l + \phi S_g \rho_g e_g + (1 - \phi) \rho_s C_s T) - Q^h = -\nabla \cdot (\mathbf{q}^h) \quad (15)$$

where  $e_l$  and  $e_g$  are the internal energies of the liquid and gas phases,  $\rho_s$  is the grain density,  $C_s$  is the heat capacity of the grains,  $Q^h$  is a heat source or sink term and  $\mathbf{q}^h$  is the heat flux of each component of each phase. The flux is the summation of the advective and diffusive heat fluxes of each component of each phase,

$$\mathbf{q}^h = \sum_\psi \sum_\kappa h_\psi^\kappa \mathbf{q}_\psi^\kappa - \lambda_m \mathbf{I} \nabla T \quad (16)$$

where  $h_\psi^\kappa$  is enthalpy of component  $k$  in phase  $\psi$  and  $\lambda_m$  is thermal conductivity. There is a single temperature describing both the pore fluid and the rock grains at a given location. *TOUGH3* uses an integral finite difference discretization, and time integration is first-order backward Euler and fully implicit. The unknowns are temperature, pressure, and saturation in multiphase systems. The discretization results in nonlinear algebraic equations that are solved via a Newton-Raphson scheme with numerical evaluation of the Jacobian.

## 7.1 Coupling Methodology

LBNL previously developed a *FLAC3D-TOUGH2* coupling scheme (Rutqvist et al. 2002). This was extended to large strain by Blanco-Martin et al. (2017) and to *TOUGH3* by Rinaldi et al. (2018). The existing coupling is for quasi-static mechanical conditions. The new coupling methodology discussed here will relax this restriction but may be less generally applicable. The coupling will be designed specifically to study the mechanical response of a submerged and water-filled DPC to a criticality event in the fuel.

The models are coupled sequentially. Fluid temperature, fluid phase, and saturation are predicted by *TOUGH3* and mechanical stresses are predicted by *FLAC3D*. The coupling consists of a loop in which temperature, pressure, and saturation are transferred to *FLAC3D* and an updated effective stress is transferred to *TOUGH3*. Nonlinear empirical expressions are used to update hydraulic properties as stress changes. The effect of changes in fluid pressure and rock temperature on deformation is considered, as is the effect of mechanical deformation on porosity and permeability. The *FLAC3D* and *TOUGH3* grids are maintained so they correspond. Figure 43 shows a schematic of the coupled calculation sequence.

Following the approach of Rutqvist et al. (2002) the porosity of the porous medium is adjusted as a function of mean effect stress,  $\sigma'_M$ ,

$$\phi = \phi_r + (\phi_0 - \phi_r) \exp(a \sigma'_M) \quad (17)$$

where  $\phi_r$  is the residual porosity,  $\phi_0$  is the porosity at zero stress, and the term  $a$  is experimentally determined. The parameter  $a$  can take the form  $a = \log(0.5) \sigma'_c$ , where  $\sigma'_c$  is a characteristic stress at which porosity is halfway between the zero stress and residual porosity. Once porosity is known, permeability can be calculated from a variety of different empirical formulas. One approach is

$$k = k_0 \exp \left[ c \left( \frac{\phi}{\phi_0} - 1 \right) \right] \quad (18)$$

Where  $k_0$  is the permeability at zero stress and  $c$  is experimentally determined. Zone-based temperatures are used by *FLAC3D* for the coupling.

Optionally, a source term can be added to the *TOUGH3* mass conservation equation to account for pore pressure generation due to porosity change. The equation becomes

$$\frac{\partial}{\partial t} \mathbf{M}^k + \mathbf{M}^k \alpha \frac{\partial \epsilon_v}{\partial t} - Q^k = \nabla \cdot (\mathbf{q}_l^k + \mathbf{q}_g^k) \quad (19)$$

where  $\epsilon_v$  is the volumetric strain.

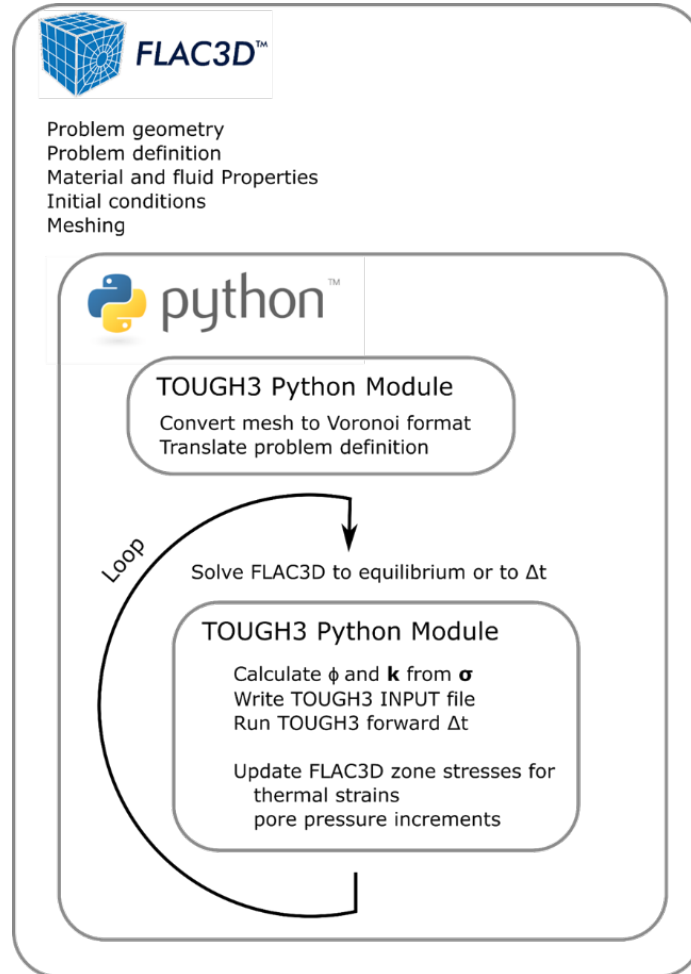


Figure 43. Schematic of *FLAC3D*–*TOUGH3* coupling.

## 7.2 Coupling Implementation

From a software engineering perspective, coupled problems are solved by using the *FLAC3D Python* scripting engine to run and communicate with *TOUGH3* and to calculate the appropriate coupling terms. A *Python* module (*flac3dtough3*) has been created to make transferring data to *TOUGH3* easier. *TOUGH3* uses files formatted with fixed-width *FORTTRAN* records. The

*flac3dtough3* module has a single class (*flac3dtough3.FLAC3D\_TOUGH3*) that does the following tasks:

- Converts the *FLAC3D* mesh into the *TOUGH3 MESH* file
- Provides easy-to-use functions to set *TOUGH3 INFILE* records
  - Utility functions are provided to map between *FLAC3D* zone id and *TOUGH3* grid block names and to write fixed width *FORTRAN* records.
- Transparently runs *TOUGH3* and checks for errors
- Parses the *TOUGH3* output for temperature and pore pressure
- Calculates porosity as effective stress changes
- Optionally applies a volumetric source term to account for pore-pressure generation
- Calculates permeability as porosity changes
- Applies the *TOUGH3* pore pressure to the *FLAC3D* zones
- Applies thermal strains to *FLAC3D* zones

The automatically generated *flac3dtough3.FLAC3D\_TOUGH3* is shown in Appendix D.

### **7.3 Example Coupling Problem**

The example shows pore pressure and thermal effects in a source-sink flow where colder water is injected into a hot reservoir. A horizontal 2-D slice of a reservoir compartment of 20 m × 20 m is represented. A Mohr-Coulomb material model is used with bulk modulus of 10 GPa, shear modulus of 3 GPa, friction angle of 25°, and cohesion of 100 MPa. The initial conditions are total stress of 50 MPa, pore pressure of 10 MPa, and formation temperature 300°C. Fluid at 100°C is injected at 0.5 kg/sec into a well in the lower left and the same flow is produced at a well in the upper right. Figures 44, 45, 46, and 47 show the *TOUGH3* predictions of pore pressure and rock temperature, and the *FLAC3D* predictions of total stress and effective stress.

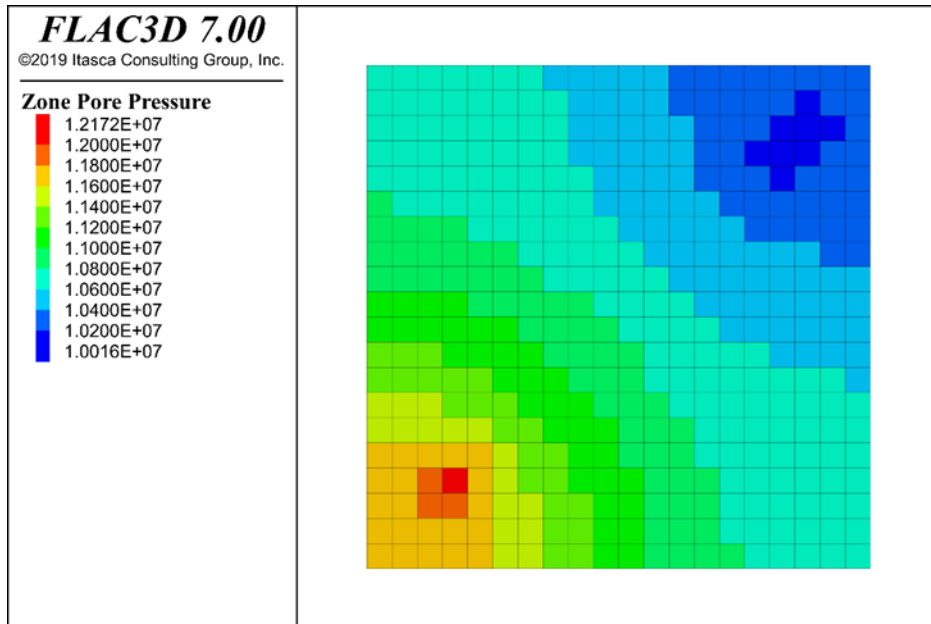


Figure 44. *TOUGH3* predictions of pore pressure (Pa) for cold water injection.

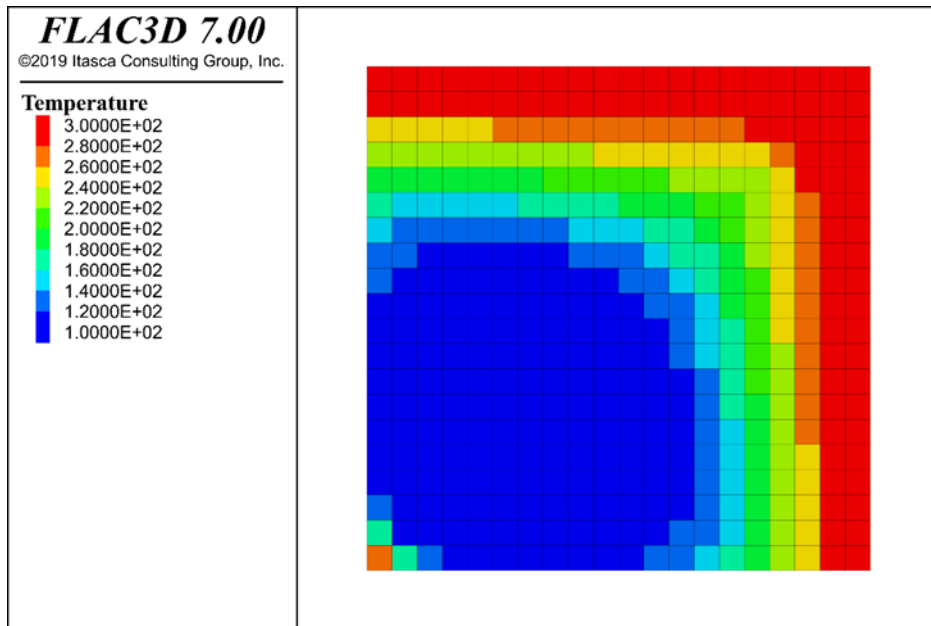


Figure 45. *TOUGH3* predictions of temperature (°C) for cold water injection.

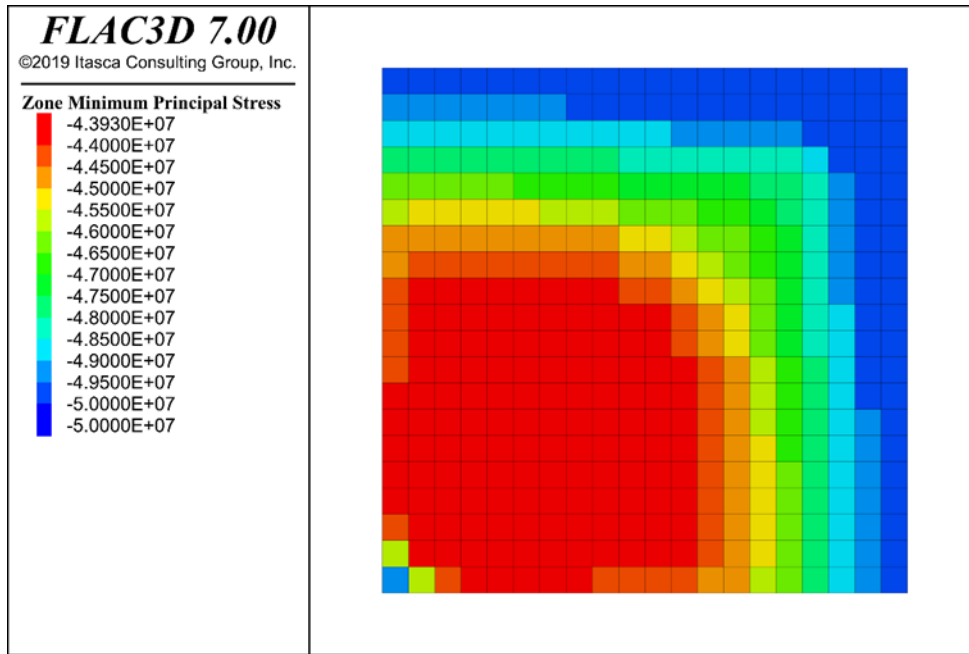


Figure 46. *FLAC3D* predictions of total stress (Pa) (including thermal strains).

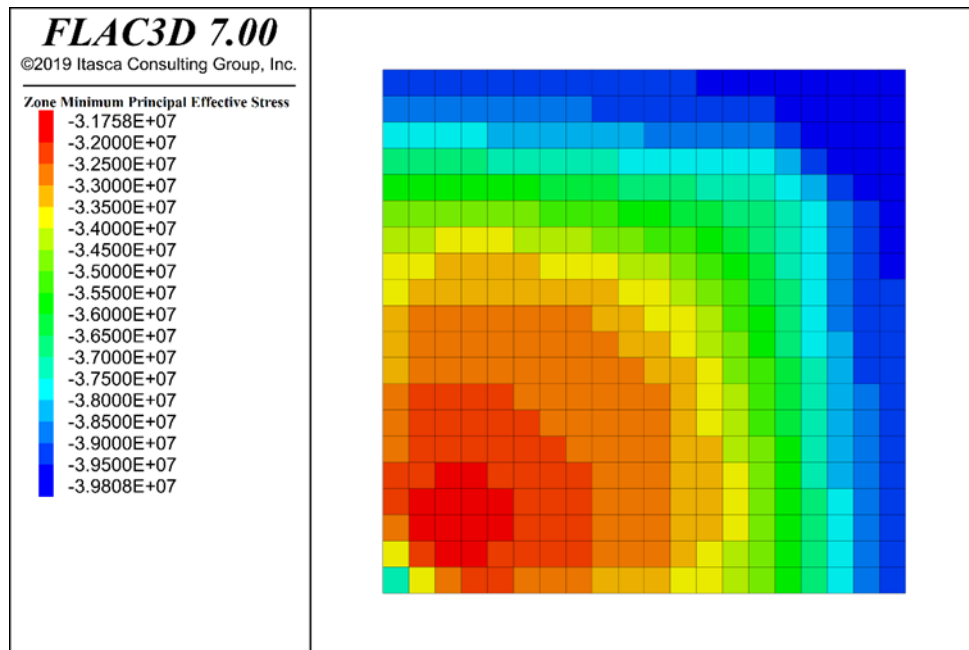


Figure 47. *FLAC3D* predictions of effective stress (Pa).

## 8. Summary and Recommendations

Conclusions and recommendations from the foregoing model descriptions are collected below for each model area. Note that in future studies these models may be renamed and/or re-purposed to reflect evolutionary development, as the capabilities and applications come into better focus.

### 8.1 Fuel Assembly Cell Model

The meshless, distinct element approach used in *PFC3D* software has been shown to be useful for studying redistribution of corrosion products, and particularly for controlling particle shape, and the conditions for particle formation and release. Results show that seismic ground motion might cause rapid thinning of partially degraded absorber plates, in baskets made entirely from aluminum-based materials, which is a condition that could lead to transient criticality events. Further parameter studies and constraint data are needed to increase confidence in model predictions of this type. The modeling approach should also be extended to BWR fuel, and stainless steel baskets with Boral® sandwich-type absorber plates.

An important uncertainty in modeling of plate degradation is the criterion for release of corrosion-product particles from the plates. In particular, the extent of release in the event of a seismic event could determine whether a transient criticality event occurs, and the nature of the event. To address these uncertainties, future work should represent the mechanics of detachment and unravelling of corrosion products. One approach is to model the plates as bonded assemblies of spheres or balls representing the intact MMC material. During corrosion the bonds could be allowed to break randomly near the face, releasing particles. This could more realistically represent the particle size and timing of disaggregation, e.g., particles in the roof may fall at a faster rate than those on the sides. The approach would also explicitly represent weakening and thinning of the neutron absorbing plates.

### 8.2 Basket Degradation Model

Preliminary results show that degradation of metal plates comprising an “egg-crate” basket structure will lead to redistribution of loads onto fuel assembly components (spacer grids, nozzles), deformation of fuel rods, and degradation of neutron absorbing components. It is recommended that future work examine critical failure modes for basket plates using continuum mechanics (*FLAC3D*) and incorporate the results into the *3DEC* model. Degraded components (fuel rods, basket plates, and other components) in these models should be represented as disaggregated pieces rather than removing degraded components from the model. Spatial heterogeneity of properties such as corrosion rates, should be added so that components fail progressively rather than all at once.

Mechanical modeling of the entire basket and DPC shell has shown that the relative locations of the basket side supports is crucial to predicting gross deformations of the fuel and basket. This means that the *rotational orientation* of waste packages at emplacement must be controlled to allow such predictions.

External loading of a DPC by ground water pressure, after breach of the disposal overpack but prior to breach of the canister, should be simulated using a variant of the basket degradation model that includes the canister shell, and allows large displacements and yielding of structural components.

Additional detail is needed for key features such as spacer grids and rod-end attachments, to understand the potential for fuel and basket deformations that increase void space and could make

fuel locally more reactive (i.e., that increase fuel rod pitch in a large enough region to support a criticality event).

The basket collapse model can also be used to represent degraded configurations with postclosure disposal criticality control features added to the basket or to fuel assemblies, such as disposal control rods in the guide tubes of PWR fuel assemblies. Extending the model to BWR fuel, it could represent the configuration of fuel channels designed specifically for criticality control (e.g., channels made from advanced neutron absorbing alloys).

### **8.3 Waste Package Breach Model**

For both the canister and overpack, longitudinal initial fractures around 1 cm and longer can grow due to internal pressurization, unless tensile stress exceeds the ultimate strength of the cylinder wall (in which case rupture occurs). For both the canister and overpack, initial circumferential “hoop” fractures less than approximately 6 cm long will not grow before plastic yielding occurs. In general, critical pressures required to fail the overpack are greater than for the canister shell because of greater thickness. Preliminary results show that fracture growth will not occur if the ultimate strength of stainless steel is reached before critical pressure for fracture growth. Note that these models are quasi-static, with constant pressure, and that behavior could change in a transient model if inertial effects are important in the vicinity of the cracks.

Preliminary results suggest that deformation of initial cracks in a DPC shell and disposal overpack could increase the transmissivity at relatively low differential pressures. In addition, critical differential pressures at which cracks start to grow are estimated to be just a few MPa. This could be significant from the standpoint of allowing voiding of critical regions in the fuel during a criticality event, and thereby limiting the energy of transient events. One potentially important complication is the series arrangement of breaches in the canister and overpack and its effect on composite transmissivity, which should be investigated.

The next steps in modeling WP breach behavior should be to account for residual stresses, then produce a dynamic pressure-time history by adding a pulse of heat energy to a constrained volume of fluid representing a saturated WP. A scoping model can be built to include thermal expansion of the fluid, and heat conduction inside and outside the WP, and to couple internal pressure to transmissivity of the WP breach. The venting rate for water mass from the package would be a function of breach morphology, energy input, and other important factors.

### **8.4 Coupling of Mechanical, Thermal, and Flow Processes**

Much work remains to develop coupling of *FLAC3D* with a heat-mass transport code such as *TOUGH3*. A similar transport code, *PFLOTRAN* (open-source freeware) is being used extensively for PA and should be considered for coupling with *FLAC3D*. These are fully implicit heat-mass transport codes, whereas *FLAC3D* is fully explicit, which presents numerical challenges to ensure accuracy and stability conditions. Note that *FLAC3D* has been selected by investigators for coupling schemes, in lieu of fully implicit finite element codes, because of the mechanical modeling features (e.g., interfacing with distinct element codes, and seismic boundary conditions) and constitutive models (e.g., creep) that are available.

The finite-displacement capability of *FLAC3D* should be incorporated in the coupling scheme and tested for conservation and flux balances, in multi-dimensional problems of increasing complexity. The problems should include adjustments to permeability based on finite volume strain, and they should include approximations for open spaces in the model (e.g., pseudo-permeability).

## 9. References

- Ahn T., H. Akhavannik, G.Bjorkman, F.C. Chang, W. Reed, A. Rigato, D. Tang, R.D. Torres, B.H. White and V. Wilson 2018. *Dry Storage and Transportation of High Burnup Spent Nuclear Fuel (Draft Report for Comment)*. NUREG-2224. U.S. Nuclear Regulatory Commission, Office of Nuclear Material Safety and Safeguards.
- Bale, M. 2000. *Clad Degradation – Local Corrosion of Zirconium and its Alloys Under Repository Conditions*. ANL-EBS-MD-000012 REV 00. Office of Civilian Radioactive Waste Management, U.S. Department of Energy.
- Balfour, M.G., G.R. Kilp, R.J. Comstock, K.R. McAtee and D.R. Thornburg 1992. *Corrosion of Zircaloy-Clad Fuel Rods In High-Temperature PWRs: Measurement of Waterside Corrosion In North Anna Unit 1*. Westinghouse Electric Corp., for the Electric Power Research Institute. EPRI-TR-100408.
- Berzins, A., J.V. Evans and R.T. Lowson 1977. “Aluminium Corrosion Studies. II. Corrosion Rates in Water.” *Australian Journal of Chemistry*. V. 30, pp. 721-731.
- Blanco-Martin, L, J. Rutqvist and J.T. Birkholzer 2017. “Extension of TOUGH-FLAC to the finite strain framework.” *Computers and Geosciences*. V.108, pp. 64-71 (10.1016/j.cageo.2016.10.015).
- Blue, P. 2009. *Material Qualification Program for Metamic-HT for use in HI-Star 180 Fuel Basket*. Holtec International.
- Buongiorno, J. 2010. “PWR Description.” Advance Center for Advance Nuclear Energy System, Massachusetts Institute of Technology. ([https://ocw.mit.edu/courses/nuclear-engineering/22-06-engineering-of-nuclear-systems-fall-2010/lectures-and-readings/MIT22\\_06F10\\_lec06a.pdf](https://ocw.mit.edu/courses/nuclear-engineering/22-06-engineering-of-nuclear-systems-fall-2010/lectures-and-readings/MIT22_06F10_lec06a.pdf) accessed 28 August 2019).
- BSC (Bechtel-SAIC Co.) 2005a. *Commercial Spent Nuclear Fuel Handling in Air Study*. 000-30R-MGR0-00700-000-000. Office of Civilian Radioactive Waste Management, U.S. Department of Energy.
- BSC (Bechtel-SAIC Co.) 2005b. *Cladding Degradation Summary for LA*. ANL-WIS-MD-000021 REV 03. Office of Civilian Radioactive Waste Management, U.S. Department of Energy.
- Crank, J. 1956. *The Mathematics of Diffusion*. Oxford University Press. 347 pp.
- Einzig, R.E. and R.V. Strain 1986. “Behavior of Breached Pressurized Water Reactor Spent-Fuel Rods in an Air Atmosphere Between 250 and 360°C.” *Nuclear Technology*. 75(1). pp. 82-95.
- Hillner, E., D.G. Franklin and J.D. Smee 1994. *The Corrosion of Zircaloy-Clad Fuel Assemblies in a Geologic Repository Environment*. WAPD-T-3173. West Mifflin, Pennsylvania: Bettis Atomic Power Laboratory.
- Holtec (Holtec International) 2018. *Safety Analysis Report on the HI-Star 100 MB Package*. Ver. 0. Revision 15 issued October 11, 2010.
- Itasca (Itasca Consulting Group, Inc.) 2016. *3DEC — Three-Dimensional Distinct Element Code, Ver. 5.2*. Minneapolis, MN.
- Itasca (Itasca Consulting Group, Inc.) 2017. *FLAC3D — Fast Lagrangian Analysis of Continua in Three-Dimensions, Ver. 6.0*. Minneapolis, MN.

Itasca (Itasca Consulting Group, Inc.) 2019. *FLAC3D — Fast Lagrangian Analysis of Continua in Three-Dimensions, Ver. 7.0*. Minneapolis, MN.

Itasca (Itasca Consulting Group, Inc.) 2018. *PFC3D — Particle Flow Code in Three-Dimensions, Ver. 6.0*. Minneapolis, MN.

Jerden, J., V.K. Gattu and W. Ebert 2018. Update on Validation and Incorporation of a New Steel Corrosion Module into Fuel Matrix Degradation Model. M4SF-18AN010301017/M4SF-18AN010302016. Office of Spent Fuel and Waste Science and Technology, U.S. Department of Energy.

Jerden, J., K. Frey and W. Ebert 2017. *Spent Fuel Matrix Degradation and Canister Corrosion: Quantifying the Effect of Hydrogen*. FWD-SFWST-2017-000039/SFWD-SFWST-2017-000042. Office of Spent Fuel and Waste Science and Technology, U.S. Department of Energy.

Jerden, J.L., K. Frey and W. Ebert 2015. “A multiphase interfacial model for the dissolution of spent nuclear fuel.” *Journal of Nuclear Materials*. V. 462, pp. 135-146.

Jung, Y, G.S.H Pau, S. Finsterle and C. Doughty 2018. *TOUGH3 User’s Guide Version 1.0*. Energy Geosciences Division, Lawrence Berkeley National Laboratory, University of California, Berkeley, California.

Lee, S.-H., J. Kim and K. Song 2007. “Design improvement of an OPT-H type nuclear fuel rod support grid by using an axiomatic design and an optimization.” *Journal of Mechanical Science and Technology*. V. 21, pp. 1191-1195. (10.1007/BF03179035)

Lindgren, E.R. and S.G. Durbin 2013. *Laminar Hydraulic Analysis of a Commercial Pressurized Water Reactor Fuel Assembly*. NUREG/CR-7144. U.S. Nuclear Regulatory Commission. (SAND 2008-3938).

Matthews W.T. 1973. *Plane Strain Fracture Toughness (K<sub>IC</sub>) Data Handbook for Metals*. Army Materials and Mechanics Research Center. Distributed by National Technical Information Service (NTIS), U.S. Department of Commerce.

Motta, A.T., A. Couet and R.J. Comstock 2015. “Corrosion of Zirconium Alloys Used for Nuclear Fuel Cladding.” *Annual Reviews of Materials Research*. V. 45, pp. 311–343.

NRC. 2006. “Potential Rod Splitting Due to Exposure to an Oxidizing Atmosphere During 33 Short-term Cask Loading Operations in LWR or Other Uranium Oxide Based Fuel,” Interim Staff 34 Guidance 22, Washington, DC. ADAMS Accession No. ML061170217.

Popov, S. G., et al. (2000) “Thermophysical properties of MOX and UO<sub>2</sub> fuels including the effects of irradiation,” ORNL/TM-2000/351. (<https://info.ornl.gov/sites/publications/Files/Pub57523.pdf>).

Rinaldi, A.P., J. Rutqvist and M. Hu 2018. “Coupling TOUGH3 with FLAC3D for Parallel Computing of Fluid Flow and Geomechanics.” Proceedings TOUGH Symposium 2018. Berkeley, CA. October, 2018.

Rutqvist, J., Y.-S. Wu, C.-F. Tsang and G. Bodvarsson 2002. “A Modeling Approach for Analysis of Coupled Multiphase Fluid Flow, Heat Transfer, and Deformation in Fractured Porous Rock.” *Int. J. Rock Mech. Min. Sci.* V. 39, pp. 429–442.

Siegmann, E. 2000a. *Clad Degradation – Summary and Abstraction*. ANL-WIS-MD-000007 REV 00 ICN 01. Office of Civilian Radioactive Waste Management, U.S. Department of Energy.

Siegmann, E. 2000b. *Clad Degradation – FEPs Screening Arguments*. ANL-WIS-MD-000008 R0 ICN1. Office of Civilian Radioactive Waste Management, U.S. Department of Energy.

Stout, R.B. and H.R. Leider 1998. *Waste Form Characteristics Report*. UCRL-ID-108314, Version 1.3. Lawrence Livermore National Laboratory, Livermore, CA.

Transnuclear Inc. (2004) *Standardized NUHOMS® Horizontal Modular Storage System for Irradiated Nuclear Fuel – Final Safety Analysis Report (Non-Proprietary), Appendix N, Rev. 8*. NUH-003.

Westinghouse 2009. *Westinghouse Technology Systems Manual, Section 3.1, Reactor Vessel and Internals*. U.S. Nuclear Regulatory Commission, Human Resources Training & Development. Rev. 09-09.

Wolfe, R. A., and S. F. Kaufman 1967. “Mechanical Properties of Oxide Fuels (LSBR/LWB Development Program).” Report for the U.S. Atomic Energy Commission by Bettis Atomic Power Laboratory, Contract AT-11-1-GEN-14. (<https://www.osti.gov/servlets/purl/4511674>).

### Appendix A. Fuel Assembly Characteristics

The characteristics of fuel assembly are selected from the following table using a 17×17 array.

Table A-1. PWR fuel assembly characteristics (adapted from Table 1.2.10, Holtec 2018).

Table 1.2.10 (continued)  
PWR FUEL ASSEMBLY CHARACTERISTICS (Note 1)

Fuel Assembly Array/Class	15x15G	15x15H	16x16A	17x17A	17x17B	17x17C
Clad Material (Note 2)	SS	ZR	ZR	ZR	ZR	ZR
Design Initial U (kg/assy.) (Note 3)	≤ 420	≤ 475	≤ 443	≤ 467	≤ 467	≤ 474
Initial Enrichment (MPC-24, 24E, and 24EF) (wt % <sup>235</sup> U)	≤ 4.0 (24) ≤ 4.5 (24E/24EF)	≤ 3.8 (24) ≤ 4.2 (24E/24EF)	≤ 4.6 (24) ≤ 5.0 (24E/24EF)	≤ 4.0 (24) ≤ 4.4 (24E/24EF)	≤ 4.0 (24) ≤ 4.4 (24E/24EF) (Note 7)	≤ 4.0 (24) ≤ 4.4 (24E/24EF)
Initial Enrichment (MPC-32) (wt % <sup>235</sup> U) (Note 5)	N/A	(Note5)	N/A	(Note5)	(Note5)	(Note5)
No. of Fuel Rod Locations	204	208	236	264	264	264
Fuel Clad O.D. (in.)	≥ 0.422	≥ 0.414	≥ 0.382	≥ 0.360	≥ 0.372	≥ 0.377
Fuel Clad I.D. (in.)	≤ 0.3890	≤ 0.3700	≤ 0.3320	≤ 0.3150	≤ 0.3310	≤ 0.3330
Fuel Pellet Dia. (in.)	≤ 0.3825	≤ 0.3622	≤ 0.3255	≤ 0.3088	≤ 0.3232	≤ 0.3252
Fuel Rod Pitch (in.)	≥ 0.563	≥ 0.568	≥ 0.506	≥ 0.496	≥ 0.496	≥ 0.502
Active Fuel Length (in.)	≤ 144	≤ 150	≤ 150	≤ 150	≤ 150	≤ 150
No. of Guide and/or Instrument Tubes	21	17	5 (Note 4)	25	25	25
Guide/Instrument Tube Thickness (in.)	≥ 0.0145	≥ 0.0140	≥ 0.0400	≥ 0.016	≥ 0.014	≥ 0.020

### Appendix B. Analytical Buckling Load

The critical buckling load of a beam is calculated using  $P_{cr} = \frac{\pi^2 EI}{(KL)^2}$ , where  $P_{cr}$  is Euler's critical load (longitudinal compression load on a column).  $E$  is the modulus of elasticity of column material,  $I$  is the minimum area moment of inertia of the cross-section of the column,  $L$  is the unsupported length of the column, and  $K$  is the column effective length factor (Figure B-1).

Buckled shape of column shown by dashed line						
Theoretical K value	0.5	0.7	1.0	1.0	2.0	2.0
Recommended design value K	0.65	0.80	1.2	1.0	2.10	2.0
End condition key		Rotation fixed and translation fixed Rotation free and translation fixed Rotation fixed and translation free Rotation free and translation free				

Figure B-1. Column effective length factors for Euler's critical load (image from Wikipedia, public domain.)

### Appendix C. Selection of Stainless steel Yield Strength

A typical stress-strain curve for stainless steel is schematically shown in Figure C-1. For 304L stainless steel, the yield and ultimate strength values at room temperature are reported to be 215 MPa and 505 MPa (<http://asm.matweb.com/search/SpecificMaterial.asp?bassnum=mq304a>), respectively. For stainless steel, onset of yielding is often difficult to detect. Therefore, the stress level at 0.2% strain is taken as the yield stress. The yield stress is different from the stress associated with the onset of nonlinearity. With further loading (beyond the yield strength), magnitude of stress increase required to induce permanent strain decreases, as indicated by flattening of the curve between points Y and T in Figure A1. In this region, until the ultimate strength is reached at point T (Rowlands), the deformation is uniform along the specimen. Subsequently, localization of strains and necking develop.

As temperature increases both the yield and tensile strengths decrease (Holtec 2018, Table A.1.2). The full stress-strain curve for 316 stainless steel is shown in Figure C-2, which suggests that the variation of strength from yield to ultimate strength can be represented by a straight line. The ultimate strength defines the critical pressure, or the pressure required to cause necking. For Alloy X at 200°C, Holtec (2018) suggests a yield strength of 145 MPa and an ultimate strength of 445 MPa.

Using an elastic-perfectly plastic constitutive law, the yield strength in the constitutive model is selected to be equal to the ultimate strength of the stainless steel. Also, a second analysis with a yield strength of 300 MPa representing the average value of yield and ultimate strengths at 200°C is carried out to define a region of potential uncertainty.

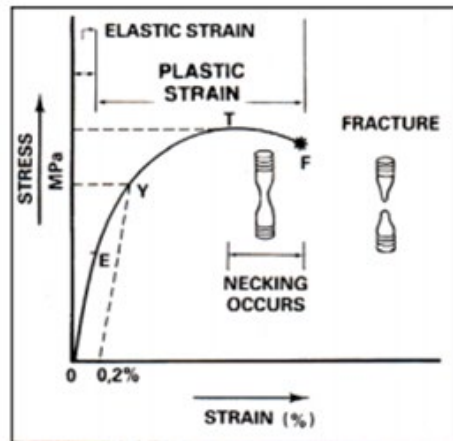


Figure C-1. Stress-strain curve for stainless steel at room temperature (Rowlands).

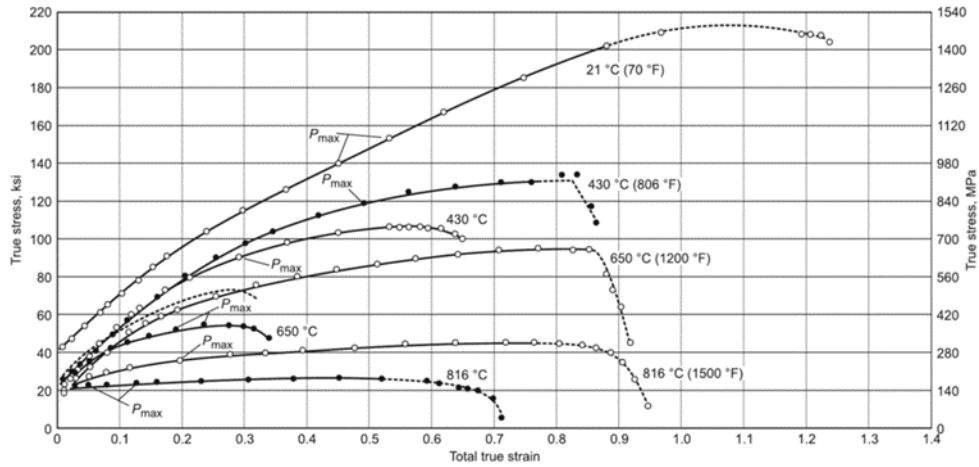


Figure C-2 Stress-strain curve for stainless steel at room temperature  
([https://icme.hpc.msstate.edu/mediawiki/index.php/316\\_Stainless\\_Steel](https://icme.hpc.msstate.edu/mediawiki/index.php/316_Stainless_Steel)).

## Appendix D. Generated *Python* Class That Performs Coupling Tasks (*flac3dtough3.FLAC3D\_TOUGH3*).

flac3dtough3 module Coupling between FLAC3D version 7.0 and TOUGH3

**class** flac3dtough3.FLAC3D\_TOUGH3

FLAC3D to TOUGH3 coupling.

**FOFT** (*EFOFT=None, IFOFT=None*) → None

Add a line to the FOFT INFILE record. This control which blocks have time series recorded by TOUGH3.  
(See TOUGH3 maunal p. 67)

**GENER** (*EL=None, SL=None, NSEQ=None, NADD=None, NADS=None, LTAB=None, TYPE=None, ITAB=None, GX=None, EX=None, HX=None*)

Add source/sink terms LTAB and ITAB can be sequences (See TOUGH3 maunal p. 75 for details)

**INCON** (*EL=None, NSEQ=None, NADD=None, PORX=None, USR1=None, USR2=None, USR3=None, USR4=None, USR5=None*) → None

Add a line to the INCON INFILE record. This sets the initial conditions for specific elements (See TOUGH3 maunal p. 64 for details.)

**PARAM\_1** (*NOITE: int = None, KDATA: int = None, MCYC: int = None, MSEC: int = None, MCYPR: int = None, MOP1: int = None, MOP2: int = None, MOP3: int = None, MOP4: int = None, MOP5: int = None, MOP6: int = None, MOP7: int = None, MOP8: int = None, MOP9: int = None, MOP10: int = None, MOP11: int = None, MOP12: int = None, MOP13: int = None, MOP14: int = None, MOP15: int = None, MOP16: int = None, MOP17: int = None, MOP18: int = None, MOP19: int = None, MOP20: int = None, MOP21: int = None, MOP22: int = None, MOP23: int = None, MOP24: int = None, TEXP: float = None, BE: float = None*) → None

Give values for the PARAM.1 record. This record gives computational parameters including timestep and convergence criteria. (See TOUGH3 maunal p. 55 for details.)

**PARAM\_2** (*TSTART=None, TIMAX=None, DELTEN=None, DELTMX=None, ELST=None, GF=None, REDLT=None, SCALE=None*) → None

Give values for the PARAM.2 INFILE record. The parameters are as described in the TOUGH3 manula except that DELTEN can be a sequence up to length 100. (See TOUGH3 maunal p. 61 for details.)

**PARAM\_3** (*RE1=None, RE2=None, U=None, WUP=None, WNR=None, DFAC=None, FOR=None, AMRES=None*) → None

Give values for the PARAM.3 INFILE record. (See TOUGH3 maunal p. 62 for details.)

**PARAM\_4** (*DEP1=None, DEP2=None, DEP3=None, DEP4=None*)

Give values for the PARAM.4 INFILE record. (See TOUGH3 maunal p. 63 for details.)

**ROCKS** (*MAT: str = None, NAD: int = None, DROK: float = None, POR: float = None, PER: float = None, PER1: float = None, PER2: float = None, PER3: float = None, CHWET: float = None, SPHT: float = None*) → None

Add a line to the ROCKS record to specify hydrogeologic parameters for a domain. Arguments are as given in the TOUGH manual but PER can be a vector or a scalar. If PER is a scalar it is copied to PER1, PER2, and PER3. (See TOUGH3 maunal p. 50 for details.)

**SOLVR** (*MATSLV=None, ZPROCS=None, OPROCS=None, RITMAX=None, CLOSUR=None*)

Give values for the SOLVR INFILE record. This controls the linear equation solver. (See TOUGH3 maunal p. 65 for details.)

**START** () → None

Add a START record to the INFILE file. (See TOUGH3 maunal p. 55 for details.)

**apply\_thermal\_strain** (*delta\_T: numpy.ndarray*) → None

Add thermal strains to FLAC3D zones due to the given temperature increment.

**calculate\_permeability** () → numpy.ndarray

Calculate a permeability from porosity.

**calculate\_porosity** () → numpy.ndarray  
Calculate porosity from the mean effective stress. Returns an array.

**clear** () → None  
Clear the TOUGH3 INFILE file values.

**convert\_FLAC3D\_mesh** () → None  
Convert the existing FLAC3D mesh into the format needed by TOUGH3. This function writes a MESH file.

**pore\_pressure** () → numpy.ndarray  
Return an array of the current TOUGH3 pore pressures.

**reset\_GENER** () → None  
Reset only the GENER (source terms) record in INFILE.

**run\_tough3** (*delete\_save: bool = True*)  
Run TOUGH3 and parse the OUTPUT file. Returns True or False for success or failure. If *delete\_save* is True (the default) the TOUGH3 SAVE file is deleted and the run starts with the initial conditions specified in the INFILE file. If False the SAVE file from a previous run remains and TOUGH3 will read the previous state as the starting state.

**set\_TOUGH\_permeability** (*permeability: numpy.ndarray*) → None  
Set the TOUGH (isotropic) permeability in each grid block.

**set\_TOUGH\_porosity** (*porosity: numpy.ndarray*) → None  
Set the TOUGH porosity in each grid block.

**set\_zone\_pp** (*offset: float*) → None  
Set the FLAC3D zone pore pressure from the values calculated by TOUGH3.

**temperature** () → numpy.ndarray  
Return an array of the current TOUGH3 temperatures.

**title** (*title: str*) → None  
Set the title line in the INFILE file. (See TOUGH3 manual p. 50 for details.)

**write\_INFILE** () → None  
Write INFILE with the values specified.